APRIL 1959 VOLUME 4 (1959) No. 3

GREGG M. SINCLAIR LIBRARY
UNIVERSITY OF HAWAII
8-7-63

NUCLEAR INSTRUMENTS & METHODS

A JOURNAL ON ACCELERATORS, INSTRUMENTATION AND TECHNIQUES IN NUCLEAR PHYSICS

EDITOR: K. SIEGBAHN - UPPSALA

CONTENTS

L. E. COLLINS and A. C. RIVIERE, A negative hydrogen ion injector for a tandem electrostatic accelerator 121
A. G. EKSPONG and B. E. RONNE, A microscope for the scanning of nuclear research emulsions 129
M. BONITZ und E. J. BERLOWITSCH, Bemerkungen zu einem schnellen 20-Kanal-Impulshöhenanalysator 133
M. MARSEGUERRA and G. PAULI, Neutron transmission probability through a curved revolving slit 140
F. D. BROOKS, A scintillation counter with neutron and gamma-ray discriminators 151
K. W. OGILVIE and D. PAIX, A pulse-height storage circuit of high stability 164
E. KASHY, R. R. PERRY and J. R. RISSER, A method for the preparation of very thin foils . . 167
J. KOCKUM and N. STARFELT, The response to high-energy gamma rays of a NaI(Tl) scintillation spectrometer 171
R. KELLER, Le mouvement anharmonique des ions dans un cyclotron et le diagramme de phase 181

NORTH-HOLLAND PUBLISHING COMPANY - AMSTERDAM

NUCLEAR INSTRUMENTS AND METHODS

A journal on accelerators, instrumentation and techniques in nuclear physics

EDITOR: K. SIEGBAHN, UPPSALA

EDITORIAL BOARD:

J. B. ADAMS (CERN)
F. A. ALSINA (Buenos Aires)
E. AMALDI (Rome)
H. L. ANDERSON (Chicago)
K. T. BAINBRIDGE (Cambridge, Mass.)
C. J. BAKKER (CERN)
P. R. BELL (Oak Ridge)
R. E. BELL (Montreal)
A. BERTHELOT (Saclay)
H. BRINKMAN (Groningen)
S. DE BENEDETTI (Pittsburgh)
M. DE HEMPTINNE (Louvain)
A. DE-SHALIT (Rehovoth)
M. DEUTSCH (Cambridge, Mass.)
S. DU TOIT (Pretoria)
B. S. DŽELEPOV (Leningrad)
W. GENTNER (CERN)
P. C. GUGELOT (Amsterdam)
H. HALBAN (Paris)
O. HAXEL (Heidelberg)
P. HUBER (Basel)
D. J. HUGHES (Brookhaven)
S. KIKUCHI (Tokyo)
J. KOCH (Copenhagen)
M. S. KOZODAEV (Moscow)
S. LIVINGSTON (Cambridge, Mass.)
E. M. MCMILLAN (Berkeley)
M. G. MEŠČERJAKOV (Moscow)
P. B. MOON (Birmingham)
M. L. OLIPHANT (Canberra)
W. PAUL (Bonn)
A. S. RAO (Bombay)
G. SALVINI (Rome)
P. SAVIĆ (Belgrade)
P. SCHERRER (Zürich)
CH. SCHMELZER (CERN)
H. W. B. SKINNER (Liverpool)
R. TANGEN (Oslo)
D. TAYLOR (Harwell)
V. I. VEKSLER (Moscow)
O. WERNHOLM (Stockholm)
G. VON DARDEL (CERN)
R. R. WILSON (Cornell)
S. D. WINTER (Saclay)

INSTRUCTIONS FOR CONTRIBUTORS

Contributions may be sent to the Editor, Professor K. Siegbahn, Institute of Physics, University of Uppsala, Sweden, either directly or through the intermediation of one of the members of the Editorial Board. Contributions may be written in English, French or German but should always, except for very short papers, be supplied with a brief abstract in English. Figures should be in inked original drawings or glossy prints and they should be sufficiently large. Contributors should make sure that important details in drawings and photographs will show up clearly in the diminished copy used by the publisher.

Books for review should be sent to Professor Siegbahn.

Objective and descriptive material on endeavours and product developments from the industry for the section "Spotlight on Industry" should be sent directly to the publishers, North-Holland Publishing Company, P.O. Box 103, Amsterdam.

Nuclear Instruments and Methods is published monthly. The subscription price of a volume of 360 pages is $ 17.00 (130 s), postage free.

Subscriptions should be sent to the publishers, North-Holland Publishing Company, P.O.Box 103, Amsterdam or to any subscription-agent.

No part of this issue may be reproduced in any form, by print, photoprint, microfilm or any other means without written permission from the publisher. Reprints, photoprints or microfilms are obtainable at cost from the publisher.

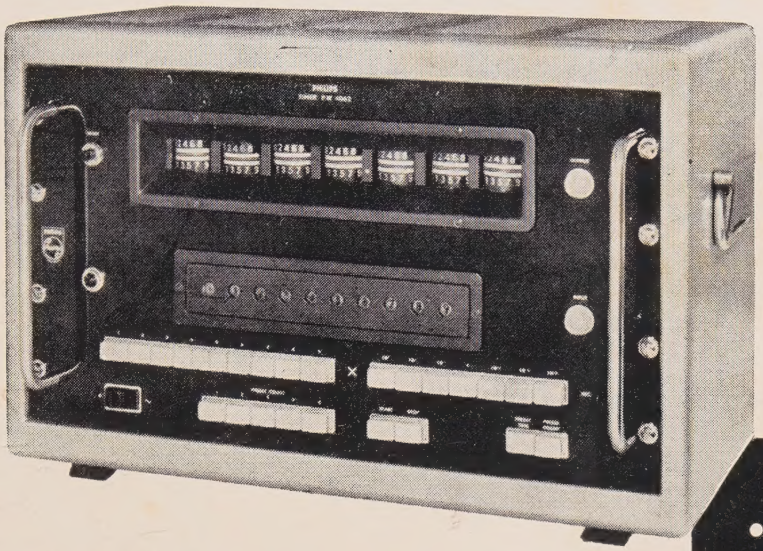

Electronic Timer PW 4062

PHILIPS

equipment for Nuclear Physics and Atomic Energy

The Philips Electronic Timer, type PW 4062

- has 60 preset time settings from 1 millisecond up to 9,000 seconds with an accuracy of 10^{-4} second,
- provides the possibility to accurately measure times from 1 millisecond up to 10,000 seconds in 10^{-3} second intervals,
- is crystal controlled,

and consequently is not only extremely suitable for special nucleonic laboratory work but for general industrial applications as well.

- Synchro-cyclotrons for various final energies.
- Cockcroft-Walton accelerators.
- Generators for very high d.c. voltages.
- Linear electron accelerators.
- Reactor control instrumentation.
- Radiation measuring and detection equipment.
- Civil defence instruments.
- Area monitoring instrumentation.
- Geiger counter tubes.
- Photomultipliers.
- Radio-active isotopes.
- Air & gas liquefiers.
- Vacuum measuring equipment.

PHILIPS

PHILIPS

Nuclear Equipment

For further information please apply to one of the following addresses:

N.V. PHILIPS' GLOEILAMPENFABRIEKEN, Scientific Equipment Department, Eindhoven-Holland
RESEARCH & CONTROL INSTRUMENTS LTD., Instrument House, 207/215, King's Cross Road, London WC1
PHILIPS ELECTRONICS INC., Instruments Division, 750, South Fulton Avenue, Mount Vernon N.Y. U.S.A.

Société d'Applications Industrielles de la Physique
S. A. I. P.
38, rue Gabriel Crié - MALAKOFF (Seine)

NUCLEAR PHYSICS

50-CHANNEL KICKSORTER "SA 50"

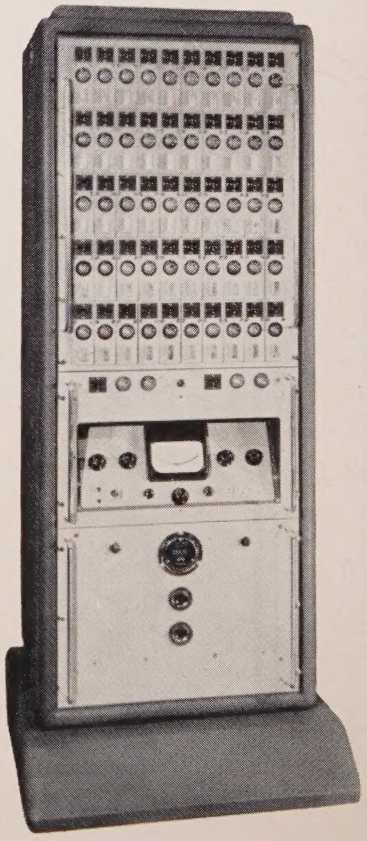

- Resolution: 1 millisecond.
- Maximum counting rate 10,000 c/sec. At high counting rates, the dead time correction is well defined throughout, and the spectrum will not undergo any deformation.
- Indication on a 1 : 10 scale, with interchangeable scales.
- For the integration, the graduation is in hundreds; for the last channel, graduation is in thousands.
- Release circuit for coincidence measurements of spectra.

OTHER PRODUCTS:

Single-channel kicksorters
Scalers
Scintillation spectrometers
Proportional counters
Circulation counters
Pressurised ionisation chambers
Linear amplifiers
Vibrating condensator type D.C. amplifiers
Automatic sampling dispensers.

AGENTS:

BELGIUM:	DRUA, 205 Avenue Van Volxem, BRUSSELS
DENMARK:	LANGEBAEK & SON, Trondhjemsgade 9, COPENHAGEN
NETHERLANDS:	ENRAF-EVERSHED, Van Leeuwenhoeksingel 69, DELFT
ITALY:	AMPERE, Via Felice Casati 8, MILAN
FINLAND:	ISOTEKNO, 13 A Mikontaku, HELSINKI
JAPAN:	RIKEI TRADING C°, Kosato Building, 12-4 Chome Shiba Tamura-Cho Minato-Ku, TOKYO
SWITZERLAND:	A. MAGAT, 28, rue de Vermont, GENEVA
U.S.A.:	LEVIANT, 239 Broadway, N.Y. 7., NEW YORK

FOR RELIABLE SCALING—

in *making* radioisotopes . . . or *monitoring* them

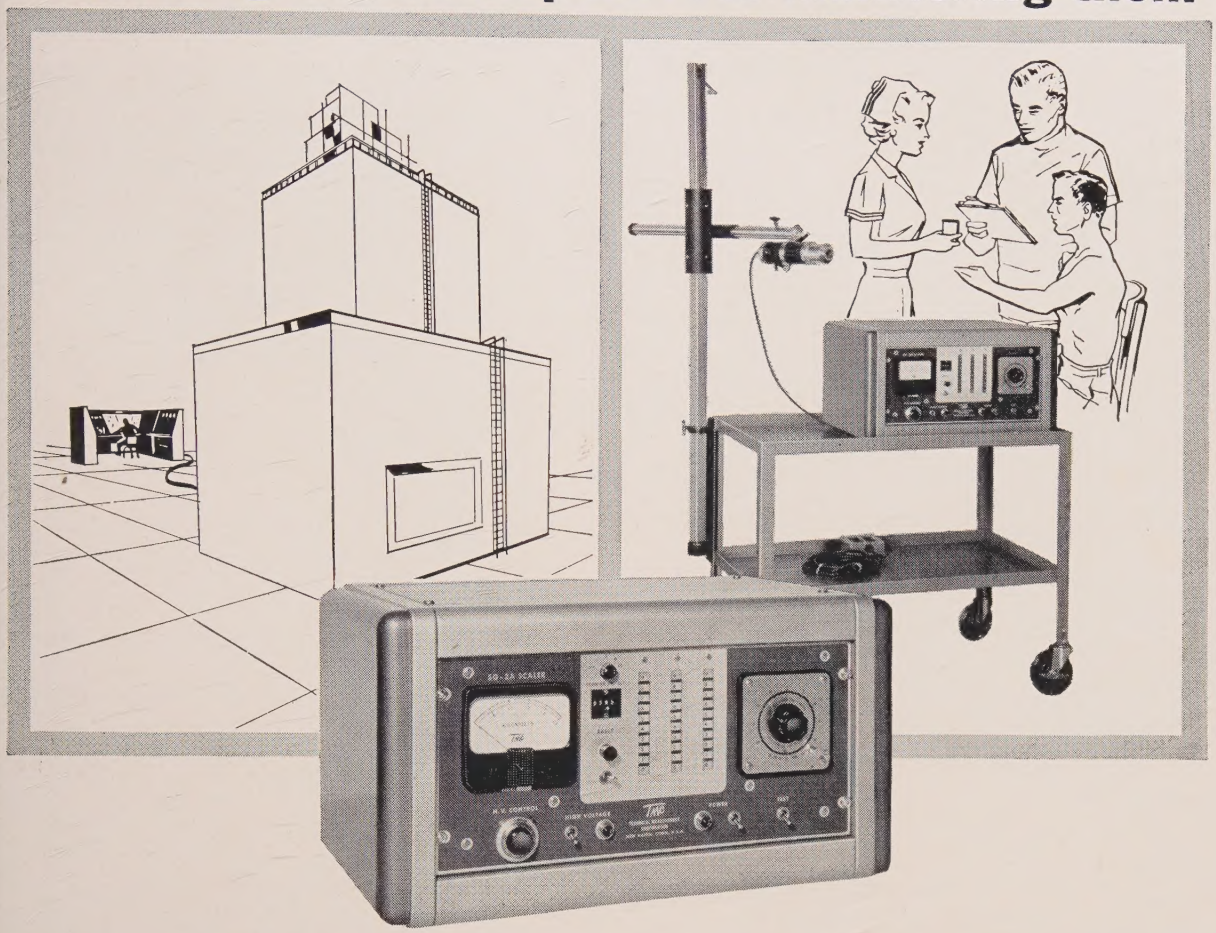

PERFORMANCE DATA

The SG-2A Scaler is a completely self-contained unit consisting of:

AMPLIFIER — Chase Higinbotham non-blocking type with selectable sensitivity — 1, 10 or 100 millivolts neg.

Rise time — 0.20 μs.

Dynamic range (at 1 mv. sens.) 10,000 to 1.

POWER SUPPLY

Dual Ranges 300 to 1000 volts, 300 to 2500 volts.

Stability — 2 volts low range, 4 volts high range (under normal operating conditions.)

(Available on special order with 5000 volt power supply for counters using high voltage gases. Dual ranges 1000 to 2500, 1000 to 5000 volts.)

SCALER — three etched wire decade strips followed by a precision four digit counter.

Counts — to 240,000 CPM with less than 1% coincidence loss.

Resolving time — 2.5 μs.

Auto-time — pre-set or elapsed time from 1 sec. to 60 min.

Accuracy $\pm$0.2 sec.

(Model SG-2A4 also available with all electronic pre-set count from 100 — 10,000 counts.)

TMC MODEL SG-2A SCALER PROVIDES ACCURACY YOU CAN DEPEND ON—AT THE REACTOR, LABORATORY OR HOSPITAL

When the SG-2A is used as part of *reactor instrumentation*, the one millivolt sensitivity and wide dynamic range of its Chase Higinbotham non-blocking amplifier permit accurate measurement of neutron levels at start-up long before the less sensitive operating instruments detect their presence. For *medical diagnostic procedures* using radioisotopes, many hospitals find that the SG-2A with the mobile cart and detector arm (above), provides the reliability and good reproduceability that are particularly necessary for thyroid function studies and blood and plasma volume measurements using Iodine (I^{131}) tracers, or in determining red cell mass with radiochromium (Cr^{51}). Countless other applications of the SG-2A range from radioactivity protective monitoring systems in industry to experimental work in college laboratories — wherever there is need for accurate radiation measurement.

If you use radioisotope tracers, write for complete information on the SG-2A Scaler, or related TMC detectors, pulse height analyzers, ratemeters and other instruments. By describing your work and the radioisotopes being used, you will enable TMC to recommend the most suitable instruments for your needs.

TMC **TECHNICAL MEASUREMENT CORPORATION**

441 WASHINGTON AVE., NORTH HAVEN, CONN.

INTERNATIONAL

advertise

YOUR NUCLEAR PRODUCTS IN

sell

YOUR NUCLEAR PRODUCTS

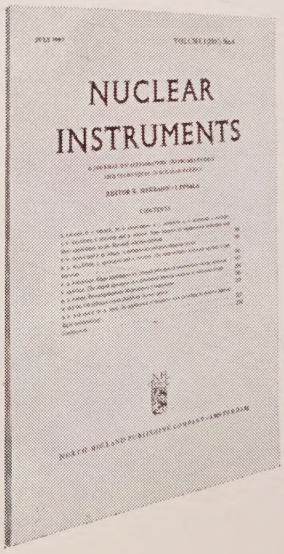

reap

YOUR NUCLEAR SALES
REWARDS

world wide

KEY NUCLEAR MANAGEMENT
NUCLEAR SCIENTISTS
NUCLEAR ENGINEERS
NUCLEAR PRODUCTION
PERSONNEL

SUBSCRIBE TO

you reach

THE WHOLE
NUCLEAR SALES WORLD IN

Entirely international in scope Nuclear Instruments and Methods is the one nuclear scientific journal that has an established subscription clientele throughout the whole world-where-ever nuclear men are at work—they want your nuclear products—they need your nuclear products—advertise in Nuclear Instruments and tell them WHAT – HOW – WHERE they can get your nuclear products

GO INTERNATIONAL WITH YOUR SALES PROGRAM TODAY WRITE

WILLIAM F. BAARS - ADVERTISING MANAGER NORTH-HOLLAND PUBLISHING COMPANY

P.O. BOX 103 – AMSTERDAM, HOLLAND

INTERNATIONAL

Announcing the Eldorado 4100

A Fast, Stable Pulse Height Analyzer

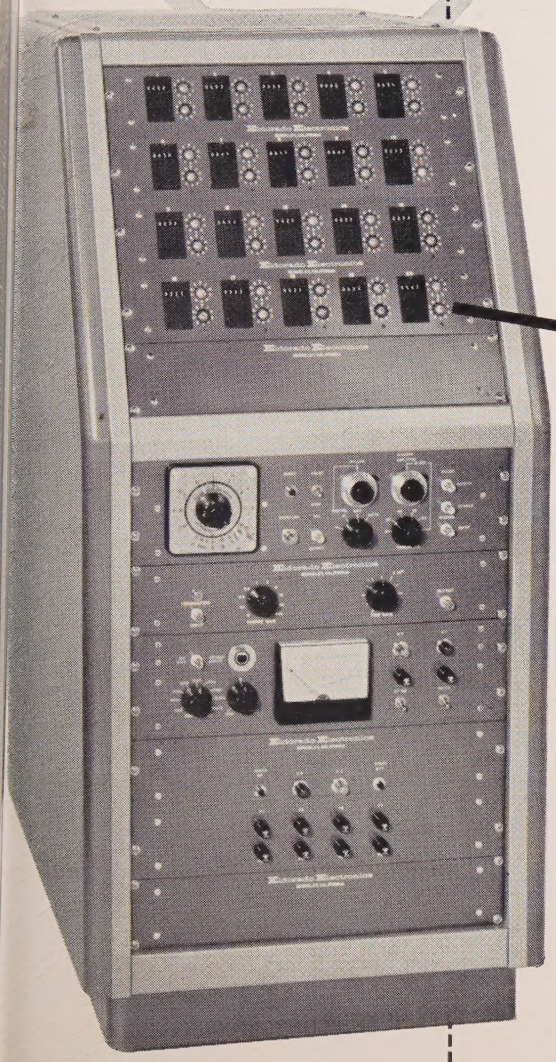

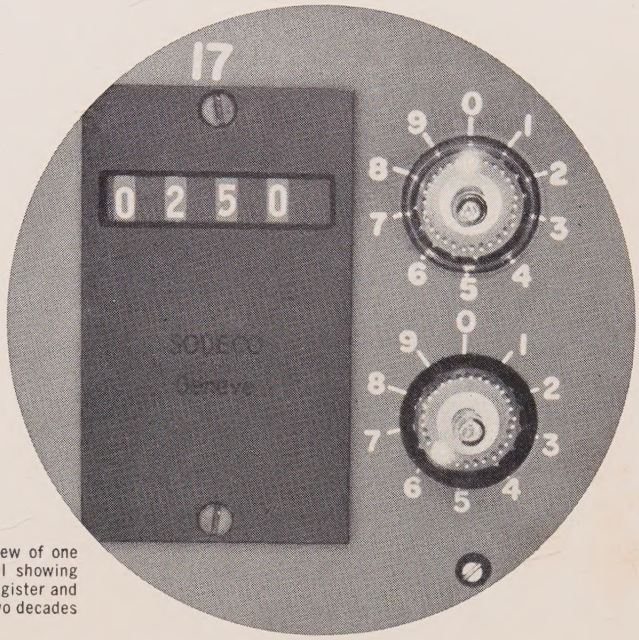

Full size view of one channel showing register and two decades

How Fast?

- ✻ Double pulse resolution better than 0.5 microseconds
- ✻ Dead time less than 0.1 microseconds
- ✻ Average counting rates greater than 10^5 counts per second without baseline distortion or use of temporary storage

How Stable?

- ✻ Channel width less than 1% drift per week
- ✻ Baseline less than 0.1% shift per week
- ✻ Channel triggering level unaffected by changes in input pulse width

Now in production, with 30 day delivery, the 4100 is priced at $8950 f.o.b. Berkeley, California. Shown with optional LA-600 Linear Amplifier and optional High Voltage Power Supply PS-530

BRIEF SPECIFICATIONS

NUMBER OF CHANNELS	20
CHANNEL WIDTH	1.0V NOMINAL
SCALER CAPACITY	10^6 COUNTS/CHANNEL
WINDOW AMPLIFIER INPUT	20V NOMINAL
WINDOW POSITION RANGE	5-105V

For complete details, call your nearby Eldorado Engineering representative or write Dept. H3

Eldorado Electronics

2821 TENTH STREET · BERKELEY 10, CALIFORNIA

Phone THornwall 1-4613

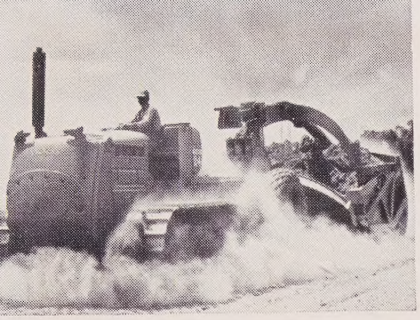

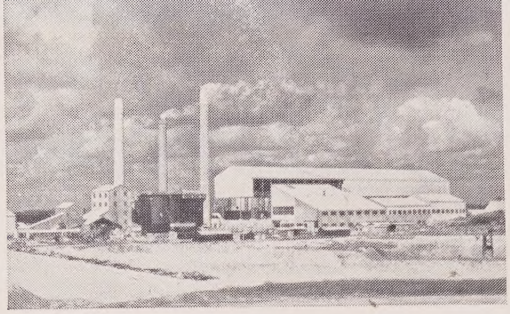

Against this background..
ELECTRON

Vickers are engineers, shipbuilders, aircraft constructors, steelmakers. They build aeroplanes, the Viscount and Vanguard, tankers, cement plants, earthmoving equipment, presses, printing machinery . . . produce steel . . . build capital equipment for Industry . . . help progress all over the world. Vickers spend on—and learn from—research. Vickers built 'Lido' swimming pool research reactor. In nuclear engineering they can provide equipment ranging from glove-boxes to reactors.

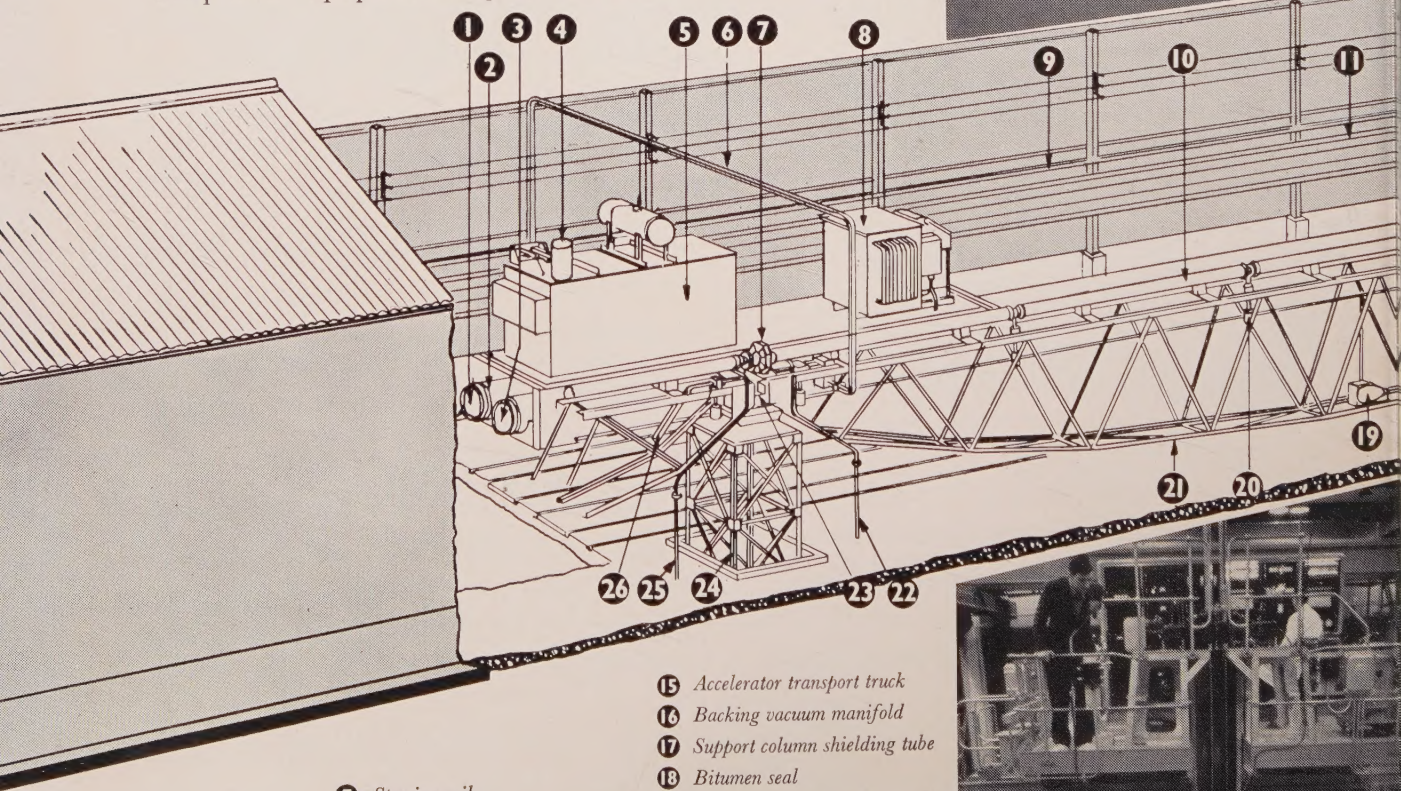

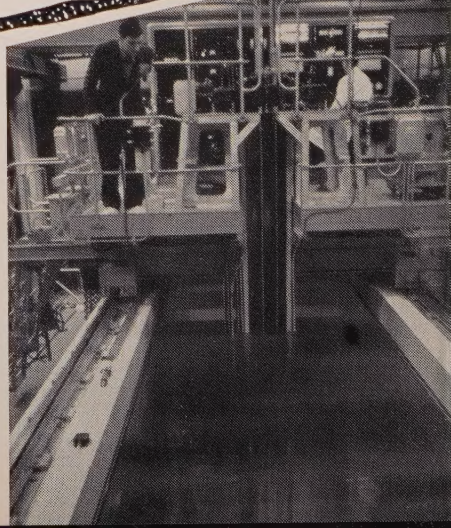

1. *Water main outlet*
2. *Lagging*
3. *Water main inlet*
4. *Klystron*
5. *Klystron Modulator Unit*
6. *Sub accelerator R.F. feed*
7. *Steering coil*
8. *Sub accelerator power supply*
9. *R.F. drive line*
10. *Accelerator tube*
11. *Supply and control cable rack*
12. *Travelling hydraulic hoist*
13. *Hoist power supply*
14. *Steel framed asbestos clad accelerator building*
15. *Accelerator transport truck*
16. *Backing vacuum manifold*
17. *Support column shielding tube*
18. *Bitumen seal*
19. *Rotary vacuum pump*
20. *Diffusion pump*
21. *20 metre sub accelerator*
22. *Water outlet*
23. *Support alignment jack*
24. *Support column*
25. *Water inlet*
26. *R.F. load*

VICKERS
are exhibiting at the
ATOMFAIR AND
NUCLEAR CONGRESS
CLEVELAND, OHIO, U.S.A.
ON STAND No. 104

Vickers designed
LINEAR ACCELERATORS

Nuclear Physics, Radiotherapy, Processing

kers Research Ltd. can supply Linear Electron Accelerators for various applications. se include custom-designed equipment for nuclear physics, accelerators for otherapy and for processing (10MeV. 5KW of electron power).

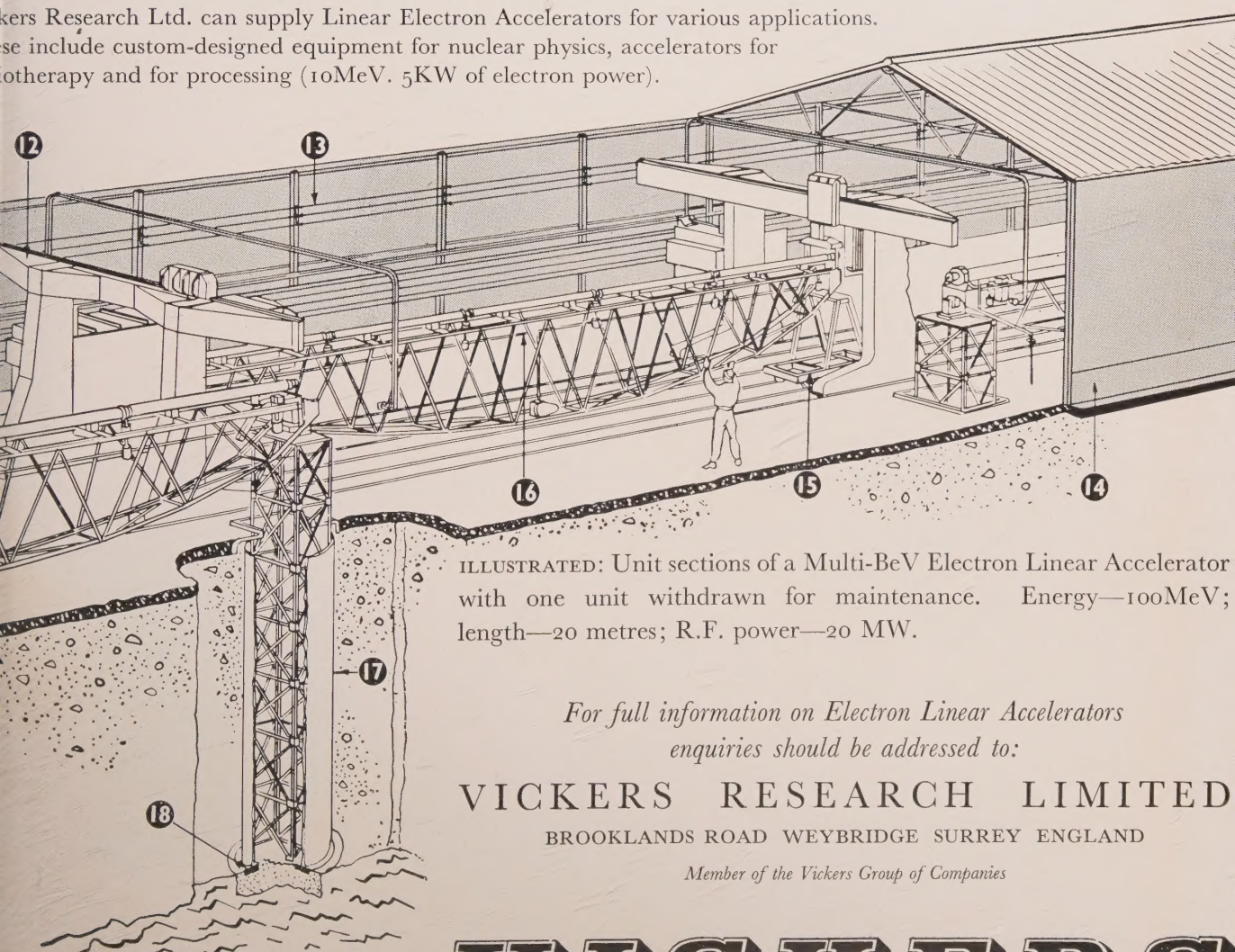

ILLUSTRATED: Unit sections of a Multi-BeV Electron Linear Accelerator with one unit withdrawn for maintenance. Energy—100MeV; length—20 metres; R.F. power—20 MW.

For full information on Electron Linear Accelerators enquiries should be addressed to:

VICKERS RESEARCH LIMITED
BROOKLANDS ROAD WEYBRIDGE SURREY ENGLAND
Member of the Vickers Group of Companies

VICKERS

AIRCRAFT CONSTRUCTORS ENGINEERS SHIPBUILDERS STEELMAKERS

The resources of the Vickers Group are available through their companies in Australia, Canada, Gt. Britain, India, Pakistan, Rhodesia, South Africa, USA

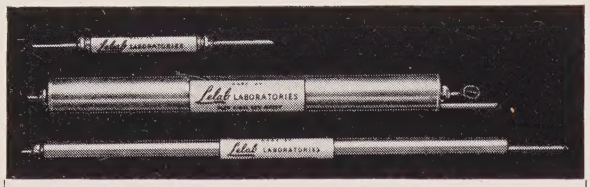

LELAB METAL-WALLED G-M TUBES

for anti-coincidence applications where uniformity counts !

Lelab Counter Tubes are individually constructed, filled, and tested. Each is fabricated almost entirely of metal. All components are confined within the diameter of the tube shell to permit close stacking.

Compare our low prices on these superior tubes!

(Makers of Lelab [Robinson-Selverstone Type] Probe Counters for neurosurgery and where a fine needle-like probe for highly localized measurements is useful.)

Write for complete information

H. W. Leighton Laboratories

York & Sunset Lane-Hatboro, Pa. U.S.A.

MODEL 412 MERCURY RELAY

PRECISION SLIDING PULSER

for Precise Calibration of Single & Multi-Channel Pulse Height Analyzers

Determines Window Widths Using Principle of *Constant Angular Velocity*

AUTOMATICALLY
10 × more accurately
40 × faster than conventional pulsers

Incorporates Both Manual Control and Precision Motor Drive

Simulates Pulses from Scintillation, Proportional or Geiger Counters

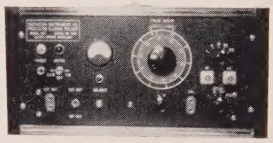

MERCURY PULSER, Model 401

Featuring Versatility and Precision

Specifically designed for the Nuclear Physics Laboratory

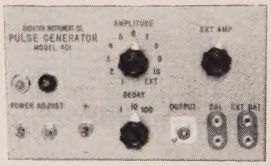

Fast rise and exponential decay simulates scintillation, proportional or geiger counter pulses for test and calibration of amplifiers, pulse height analyzers, scalers, etc.

MODEL 412 . . . $ 450.00 — MODEL 401 . . . $ 125.00

RADIATION INSTRUMENT CO.

P. O. BOX 733, SILVER SPRING, MARYLAND, U.S.A.

NORTH-HOLLAND BOOKS

Just out

Analytical and Canonical Formalism in Physics

by

ANDRÉ MERCIER

Head of the Department of Theoretical Physics, University of Berne

6 × 9″ VIII + 222 pages Guilders 20.00 (40 s.)

THE CONTENTS

i LAGRANGIAN FORMALISM
ii LAGRANGIAN DENSITY
iii CANONICAL FORMALISM
iv CANONICAL FORM OF ELECTRODYNAMICS
v HAMILTONIAN DENSITIES
vi TRANSFORMATIONS
vii CANONICAL FORMALISM WITH VANISHING JACOBIAN DETERMINANT

Sole Agency for U.S.A.: Interscience Publishers Inc. – New York

NORTH-HOLLAND PUBLISHING COMPANY — AMSTERDAM

a Complete Scintillation Service

phosphors and counters

PLASTIC LIQUID & PHOSPHORS

* PLASTIC PHOSPHOR NE 102, light output 65% anthracene, available in all sizes and shapes up to one ton, in thin sheet form, in fine tubes for the construction of scintillation flow counters, or as filaments for the construction of scintillation nuclear track chambers. (Bulletin 11).
* BORON POLYESTER PLASTIC PHOSPHOR NE 400 and NE 401(88% B^{10}) for neutron detection. Standard size from 0.5 to 5.0 inches diameter. (Bulletin 13).
* LOADED LIQUID SCINTILLATORS in bulk or encapsulated, containing Pb for extreme X-ray sensitivity, and Gd, B, Cd, and Sm for neutron detection. (Bulletins 9 and 9a).
* SCINTILLATING GELS for efficient internal counting of suspended materials. (Bulletin 9).
* SCINTILLATION CHEMICALS of highest purity P.B.D., POPOP, T.P.B., p-terphenyl, PPO, D.P.H., alpha-N.P.O., D.M.C., B.B.O., B.P.O., D.P.A., D.P.S., vinyltoluene, styrene, xylene, toluene, methyl borate, phenylcyclohexane, monoisopropylbiphenyl
* LIGHT PIPES of polyvinyltoluene and polystyrene.
* PLASTIC PHOSPHOR SPIRAL FLOW CELL NE 801 for beta and alpha emitters.

Nuclear Enterprises (G.B.) Ltd

NEW LINE OF PRECISION NUCLEAR INSTRUMENTS

* Non-overloading Linear Pulse Amplifier NE 5202 of the Fairstein type (Bulletin 14).
* Pre-Amplifier and Cathode Follower NE 5202A.
* Single Channel Pulse Height Selectors NE 5102 and NE 5103.
* Shielded Scintillation Head Units NE 5501-3.
* Highly Stabilised EHT Supplies NE 5302 (1.8 kV) and NE 5303 (5kV).
* Complete assembly for C14 and tritium counting NE 8301.
* Complete Human Body Counter Installations NE 8101–3.
* Ratemeter NE 5401 with eight ranges and six time constants.
* Scanning scintillation spectrometer NE 8601.

Bankhead Medway,
Sighthill, Edinburgh, 11, Scotland — Tel. CRA 4513

OF SPECIAL NOTE

* SCINTILLATION CRYSTALS by Harshaw. Exclusive concessionaire in Great Britain for NaI(Tl), CsI(Tl), LiI(Eu), and Li^6I(Eu). NaI(Tl) available in sizes up to 9″ diameter x 9″ thick, and down to 0.015″ thick with 0.005″ Be windows for X-ray counting and spectrometry. Resolution with standard sizes 7–8% on Cs^{137} line. CsI(Tl) down to 0.005″ thick for alpha and proton studies. Li^6I(Eu) in special low temperature mounts for fast neutron spectrometry.
* NEW! Photomultiplier-NaI(Tl) combinations with direct coupling of crystal to photomultiplier and giving improved resolution.
* C.D.C. 100-CHANNEL TRANSISTORISED KICK-SORTER at new *low* price for 1959 and with short delivery. Full range of accessories to provide automated assembly.
* MULTI-CHANNEL SCINTILLATION SPECTROMETER NE 8201 for industrial tracer investigations. (Bulletin 15).

Write now for Bulletins and Price List (ndh) 707

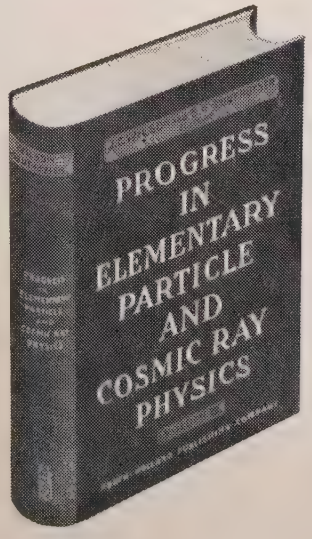

PROGRESS IN ELEMENTARY PARTICLE AND COSMIC RAY PHYSICS VOL. IV

Editors

J. G. WILSON, *Professor of Physics, University of Leeds*

and

S. A. WOUTHUYSEN, *Professor of Physics, University of Amsterdam*

6 × 9″ XII + 482 p. 110 illus. Guilders 45.00 (90 s)

CONTENTS

1. *Some Theoretical Aspects of the Strong Interactions of the New Particles* (B. D'Espagnat and J. Prentki). 2. *The Properties and Production of K-mesons* (W. D. Walker). 3. *The Interaction of μ-Mesons with Matter* (G. N. Fowler and A. W. Wolfendale). 4. *The Primary Cosmic Radiation and its Time Variations* (S. F. Singer). 5. *The Origin of Cosmic Radiation* (V. L. Ginzburg).

Sole Agency for U.S.A.: Interscience Publishers, Inc. — New York

NORTH-HOLLAND PUBLISHING COMPANY - AMSTERDAM

Send your order to your bookseller or directly to us

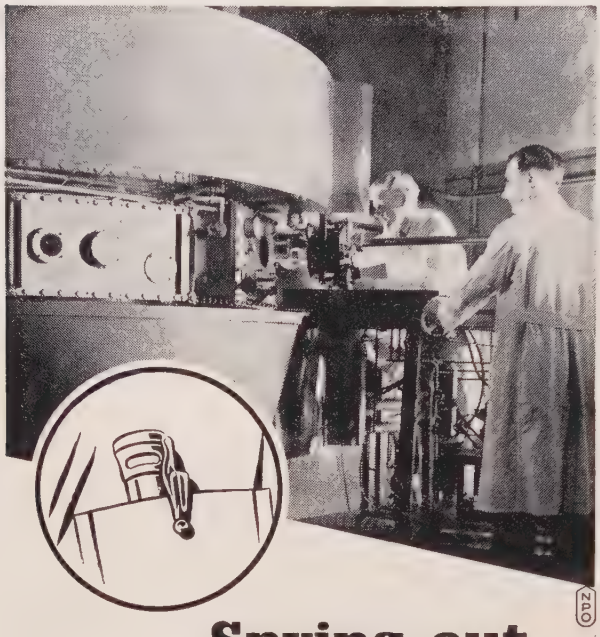

Spying out invisible danger

In nuclear research strong sources of ionising radiation impose strict demands on accurate monitoring.
Philips Pocket Dosimeters put the finger on danger spots.

Sturdily constructed to resist rough handling without loss of accuracy, these dosimeters require no separate charging device. Little larger than a fountain-pen they contain:

- a sensitive quartz-fibre electrometer
- an optical system that permits readings to be taken simply and directly
- a mercury-drop charging device

HERMETICALLY SEALED

Measuring ranges	Q 4423 C	Q 4424 C
	250 mr	20 r

PHILIPS

pocket dosimeter

The Oscilloscope with 220 Mc/s bandwidth

TYPE L362

DIMENSIONS:
only 14½ in x 8¾ in x 18 in (36·8 x 22·2 x 45·7 cm)
and weight 27lb. (12·2 kg)

- Rise time 2 milli-microseconds
- Sensitivity 150 mV/cm
- Can handle repetitive pulses of random separation
- Extremely compact and portable
- Inexpensive

Working on a novel sampling principle, the L362 provides nucleonic and electronic engineers with an inexpensive oscilloscope capable of recording rapid pulses at the higher frequencies.

The L362 oscilloscope has been developed from a design originated by the United Kingdom Atomic Energy Authority Research Establishment, Harwell.

A PRODUCT OF
MULLARD EQUIPMENT LIMITED
A COMPANY OF THE MULLARD GROUP

Write for full technical details :—

United Kingdom
RESEARCH & CONTROL INSTRUMENTS LIMITED
INSTRUMENT HOUSE
207 KING'S CROSS ROAD · LONDON W.C.1

Overseas
MULLARD EQUIPMENT LIMITED
MULLARD HOUSE
TORRINGTON PLACE · LONDON W.C.1

ME 639a

HIGH VOLTAGE ENGINEERING CORPORATION *in* EUROPE

OUR NEW FACILITY in Amersfoort, The Netherlands

will be European headquarters, in 1959, for sales, service, and manufacture of Van de Graaff® and electron linear accelerators for

- *Nuclear-physics research*
- *Electron-beam processing*
- *Supervoltage x-ray therapy*
- *Industrial radiography.*

Established to serve the European Common Market and the Euratom Nations, this new facility will enable our European distributors to offer local service and consultation.

HIGH VOLTAGE ENGINEERING CORPORATION
BURLINGTON, MASSACHUSETTS, U.S.A.

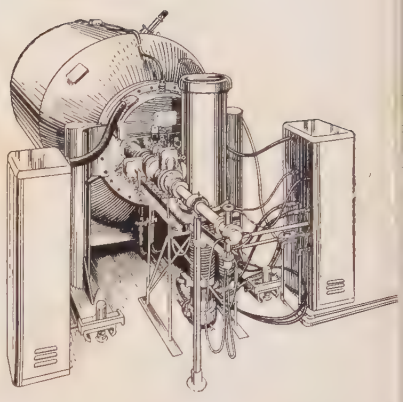

Represented by

Leybold-Hochvakuum, Cologne
for Germany,
Switzerland
Austria, Yugoslavia,
and Spain

Alpha Beta Gamma, s.r.l., Florenc
for Italy

LKB Produktor, Stockholm,
for Sweden
(for Denmark and Norway,
medical equipment)

Equipmentos Laboratorio, Lds., Lisbon
for Portugal

Saphymo, Paris
for France

and our affiliate

High Voltage Servicing Co., Ltd.
London, England
for Great Britain

NUCLEAR INSTRUMENTS AND METHODS 4 (1959) 121–128; NORTH-HOLLAND PUBLISHING CO.

A NEGATIVE HYDROGEN ION INJECTOR FOR A TANDEM ELECTROSTATIC ACCELERATOR

L. E. COLLINS and A. C. RIVIERE

Atomic Weapons Research Establishment, Aldermaston, Berkshire

Received 9 March 1959

A brief description is given of the source and accelerating system to be used for injection of negative ions into a tandem electrostatic accelerator. The ion source, which is of the radio frequency type, yields a current of 10 μA of negative hydrogen ions. The remainder of the system accelerates the ions under constant focusing conditions. The ion optical requirements for focusing of the first stage of the main accelerator are also discussed and compared with the performance of the injection system.

1. Introduction

A high voltage tandem electrostatic accelerator is being constructed in this Establishment for further studies in nuclear physics. The present report deals with the design, construction and performance of the negative ion injection system prior to its final installation.

In a tandem accelerator negative hydrogen ions are accelerated from ground potential to a positive high voltage terminal[1]). These ions are then stripped of their electrons, and the resulting high energy protons are further accelerated back to ground potential by the same field. The final proton energy is twice that corresponding to the potential of the high voltage terminal. Present techniques limit the attainable voltage to approximately 6 MV, but by using the tandem principle an effective energy of 12 MeV can be achieved for hydrogen ions.

2. The Injector Requirements for a Tandem Accelerator

A schematic drawing of the tandem accelerator is shown in fig. 1. Negative ions are injected at the point A, accelerated to the centre terminal and stripped of their electrons at B. The high energy proton beam, after further acceleration, finally leaves the machine at C. The accelerator sections and high voltage terminal are contained within a large steel tank, which is filled with a mixture of nitrogen

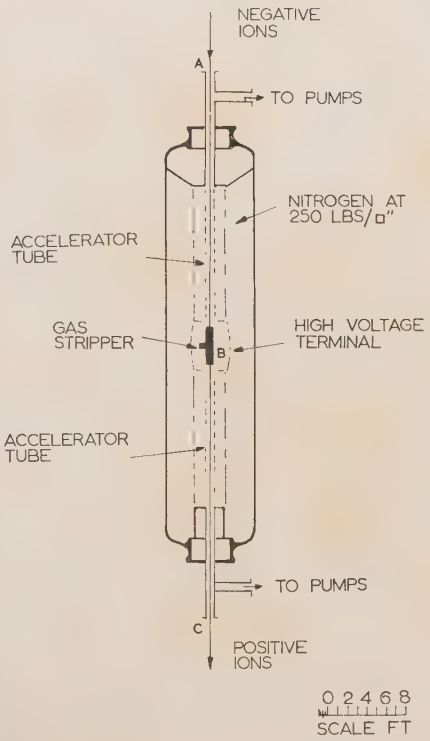

Fig. 1. General arrangement of the tandem electrostatic accelerator.

and carbon dioxide to a total pressure of 250 lbs/sq.in. The source of negative ions is outside the tank, and this is an advantage over the

[1]) J. L. Danforth, Can. Elect. Eng. 2 (1958) 18.

normal electrostatic accelerator where the source must be in the high voltage terminal inside the pressure tank.

The negative ions are stripped of their electrons in the centre terminal by undergoing atomic collisions in a region of relatively high gas pressure. The region of high gas pressure is contained by a long narrow bore tube so that a minimum quantity of gas flows into the accelerator. The tube forms a constriction through which the beam must pass, and the negative ions must be injected in such a way that minimum loss of beam occurs at this constriction. The requirements for correct injection are critical but can be calculated by means of the analysis made by Elkind[2]) of the ion-optical behaviour of long, high voltage accelerator tubes. The focusing properties of the 6 MV accelerator in this laboratory were compared with those calculated by Elkind's analysis, and it was found that the required focusing voltage differed from the calculated value by only 4 per cent. To help in the following discussion an outline of Elkind's analysis is presented here:

3. Focal Properties of a Three Element Tube

With reference to fig. 2, a long, high voltage accelerator tube can be roughly characterised by three regions, which are:

(i) a region of zero field preceding the tube,

(ii) a region of constant field throughout the length of the tube; and

(iii) a second region of zero field called the tube extension.

Optically, these regions contribute the following elements: a single aperture lens (converging) at the entrance to the tube, a constant field region throughout the length of the tube, and a second single-aperture lens (diverging) at the exit of the tube. As sketched in fig. 2, an ion appearing to have originated at a distance P_1 from the tube entrance is converged by the first aperture lens, then follows a parabolic path for the length of the tube, and is diverged at the second aperture lens so that it crosses an extension of the tube axis at a distance L_2.

For the present purposes, a relation is required between the object distance P_1 and image distance L_2. The magnification of the system must also be known. This information can be obtained by using thin lens formulae and an expression for the parabolic path in the tube.

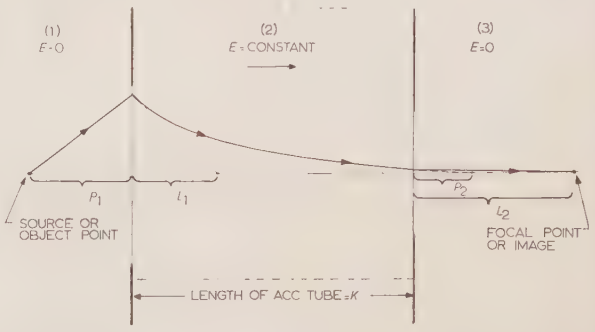

Fig. 2. Ion path in a long, high voltage accelerator tube.

An approximate expression for the focal lengths of the single aperture lenses is given by

$$f = \frac{4 \times \text{Ion Energy} \times K}{\text{Tube Voltage}}, \qquad \text{(i)}$$

where K is the length of the accelerating tube[3]).

A more precise value of f than that given by (i) has been computed by Zworykin *et al.*[3]), and the true focal lengths of the present lenses can be expressed by the relation

$$f = \zeta \times \frac{4 \times \text{Ion Energy} \times K}{\text{Tube Voltage}} \qquad \text{(ii)}$$

where ζ is a correction factor obtained from the data given in [3]).

For the entrance aperture lens $\zeta_1 = \zeta$, and for the exit aperture lens $\zeta_2 = 1$. By using equation (ii) the relation between $P = P_1$ and $L = L_2$ can be expressed as

$$\frac{K}{P} = \left[\frac{N-1}{4\zeta}\right] \cdot \frac{4\,(N^{\frac{1}{2}} - 1 - 2\zeta) + (3N^{\frac{1}{2}} - 1 - 2\zeta)\left[\frac{N-1}{N}\right]\frac{L}{K}}{4\,(N^{\frac{1}{2}} - 1) + (3N^{\frac{1}{2}} - 1)\left[\frac{N-1}{N}\right]\frac{L}{K}} \qquad \text{(iii)}$$

[2]) M. M. Elkind, Rev. Sci. Instr. **24** (1953) 129.

[3]) V. K. Zworykin, G. A. Morton, E. G. Ramberg, J. Hillier and A. W. Vance, Electron Optics and the Electron Microscope (John Wiley and Sons, Inc., New York, 1945) p. 446.

or alternatively,

$$\frac{L}{K} = 4N \cdot \frac{(N^{\frac{1}{2}} - 1 - 2\zeta) - \frac{4\zeta}{(N^{\frac{1}{2}}+1)} \cdot \frac{K}{P}}{4 \cdot \zeta \cdot \frac{K}{P}(3N^{\frac{1}{2}} - 1) - (N-1) \cdot (3N^{\frac{1}{2}} - 1 - 2\zeta)}, \quad \text{(iv)}$$

where

$$N = \frac{\text{Final Energy}}{\text{Initial Energy}} = \frac{\text{Injector Voltage} + \text{Centre Terminal Voltage}}{\text{Injector Voltage}}.$$

The overall magnification of the tube is given by

$$M = -\frac{K}{P}\left[\frac{2}{N^{\frac{1}{2}}+1}\left(1 + \frac{N-1}{4N} \cdot \frac{L}{K}\right) + \frac{1}{N^{\frac{1}{2}}} \cdot \frac{L}{K}\right]. \quad \text{(v)}$$

4. Focusing Condition for the First Stage of the Accelerator

The beam must be focused to a point at the centre of the stripper tube for optimum transmission. This fixes the value of L in the present design to 33 inches. The length of each of the accelerating tubes is 167.4 inches. From equation (iii) it can be seen that, with L and K fixed, the value of P depends only on the ratio N (ζ is only a function of N once the diameter of the lens has been specified). For a constant injection energy the value of P changes by several feet as the terminal voltage changes from 2.0 to 6.0 MV. The design of the injector becomes rather awkward if such changes in the position of a focused spot are required. However, if the injection energy is increased so that N is kept constant, then P will also be constant, that is, the position of the object point for the accelerator will be fixed for all energies. This is the focusing principle of most existing electrostatic accelerators, and it has been adopted in the present case.

The actual values of N and P are determined by practical limitations on the injection energy and mechanical access to the required object point. In the present design a figure of 50 has been chosen for N, and this requires that the injection energy must change from 40 to 120 keV as the terminal voltage is changed from 2.0 to 6.0 MV. The corresponding value of P, as calculated by equation (iii) is 28 inches. Both N and P must be held to within one per cent of their correct values in order to keep the beam focused to within 6 inches of the centre of the stripper tube.

The image size and beam divergence required at the object point for the accelerator are limited by the dimensions of the stripper tube. It can be shown that maximum transmission will occur when the size of the image at the centre of the stripper tube is equal to half the diameter of the bore, and the beam divergence is such as to fill the end aperture of the tube. With a length of 24 inches and bore diameter of $\frac{3}{16}$ inch, the above condition requires an image diameter of $\frac{3}{32}$ inch, or 0.24 cm, and a beam divergence of 0.004 radians. The magnification of the accelerator tube in the present case is 1.7 times, so that the beam diameter at the object point for the tube must be 0.14 cm and the beam divergence 0.048 radians.

It is of interest to consider the Lagrange product of image size, beam divergence and refractive index; in the present case this is 0.0013 cm·radians $(\text{MeV})^{\frac{1}{2}}$ for a terminal voltage of 2 MV, and this rises to 0.0023 cm·radians $(\text{MeV})^{\frac{1}{2}}$ at 6 MV. The refractive index in this sense is taken as the square root of the particle energy in MeV. The corresponding product at the source must be less than or equal to this value if all the beam is to pass through the stripper tube. Lens aberrations are neglected but in practice these will increase the Lagrange product of the beam and hence increase beam loss at the stripper aperture.

All the necessary properties of the injected ion beam have now been defined.

5. The Injector System

The four main requirements for the injector system are

(i) a source of negative ions,

(ii) a means of accelerating the ions to the required injection energy,

(iii) a system of lenses which transmit the ions to the object point for the accelerator with the correct image size and beam divergence,

(iv) a means for stabilising the position of the object point over the whole range of energies.

There are no doubt many ways in which these requirements could be combined into a given injector system. However, the present design

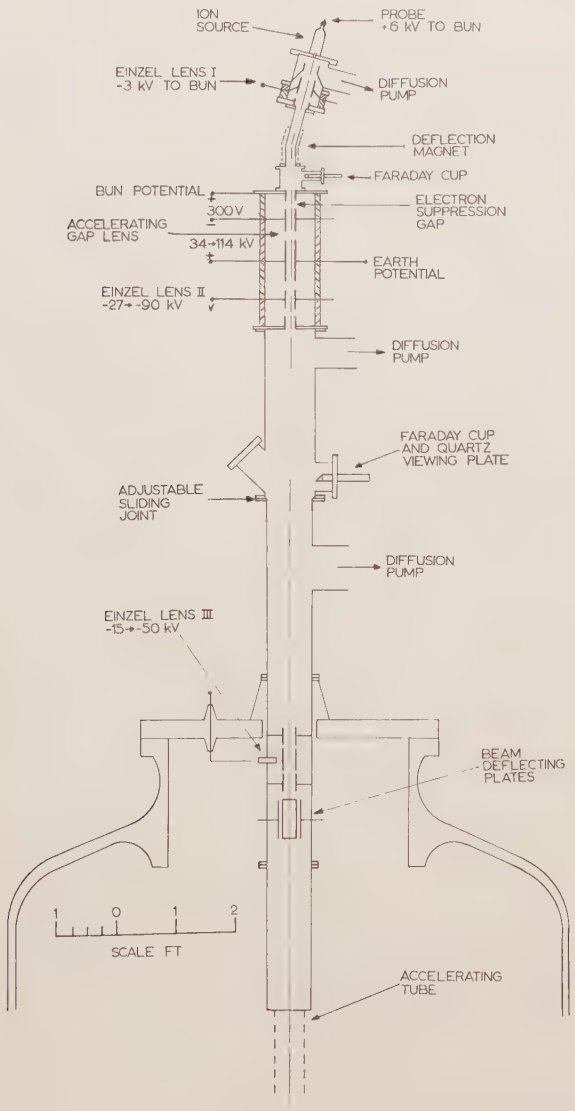

Fig. 3. General arrangement of the negative ion injector.

of the injector was influenced by the mechanical design of the accelerator, and the availability of some of the components. A schematic drawing of the injector is shown in fig. 3.

Negative ions are obtained from a radio frequency positive ion source in which use is made of the charge changing collisions occurring in the canal. A yield of 2.2 μA of negative hydrogen ions was reported by Phillips and Tuck[4]) from a source of this kind. The details of the source will be given in the following section. The particle beam leaving the canal has an energy of approximately 6.0 keV, and consists of protons, neutral atoms, and negative ions. There are also some slow electrons present. The negative ion beam is selected by a 15 degree analysing magnet. The deflection of the negative ion beam also serves to prevent neutral particles from travelling down the system and producing unwanted secondary electrons.

The negative ions are accelerated to the required energy for injection immediately after magnetic deflection. The fourth requirement is achieved by the use of an accelerating gap lens with a short focal length. The first electrostatic einzel lens (I) gathers the divergent beam from the canal and focuses it through the deflecting magnet to a point 4 inches beyond the median plane of the accelerating gap. A real image is formed between the median and focal planes of the gap lens and the variation in the position of this image is less than any variation in focal length. The gap lens consists of two cylindrical elements each 2 inches in diameter and spaced 1 inch apart. The properties of a lens of these proportions have been reported by Spangenberg[5]), and it is found that the focal length varies only slightly for the range of accelerator voltages of interest. In fact, the image formed in the gap moves only 0.5 inches towards the median plane as the gap voltage is increased from 34 to 114 kilovolts (accelerator voltage = injection voltage—extractor voltage on source). This method for stabilising the position of an image was suggested by Johnson *et al.*[6]) in their paper on The Focusing Procedures for Electrostatic Accelerators.

The stabilised image is transferred to the final object point by means of two further einzel

[4]) J. A. Phillips and J. L. Tuck, Rev. Sci. Instr. **27** (1956) 97.

[5]) K. R. Spangenberg, Vacuum Tubes (McGraw-Hill Book Company, Inc., New York, 1948) p. 371.

[6]) C. H. Johnson, J. P. Judish and C. W. Snyder, Rev. Sci. Instr. **28** (1957) 942.

lenses (II and III). The beam diameter and divergence at the final object point can be altered by changing the relative strengths of the two lenses. The potentials for the centre electrodes in each case are derived from a resistance chain across which a potential difference is applied equal to the total ion energy. For all accelerator gap voltages the focal lengths of these lenses remain constant, and with this arrangement the position of the image at the final object point should move by only 0.25 inch as the injection energy changes from 40 to 120 keV. This error in P_1 for the accelerator can be corrected for by a further small increase in injection energy.

Once the correct lens potentials have been determined on the accelerator there remains only the injection energy for the machine operator to adjust for optimum focus at the stripper.

Provision is made for observing and measuring the beam in two places. The first is just prior to the accelerator section and the second is approximately at the beam crossover between einzel lenses II and III. Each consists of a faraday cup with a secondary electron suppression electrode. A "flap" valve is also provided just prior to the accelerator section so that ion source components can be changed without letting the remainder of the system down to atmospheric pressure.

Electron loading of the accelerator gap and the associated X-radiation were originally quite troublesome. There were two sources of electrons; firstly, those which arose in the deflection magnet and drifted down to the accelerating section, and secondly, those which were formed by stray ion bombardment of the gap electrodes. This trouble was cured by placing a collimating aperture, 2 cm in diameter, just after the deflection magnet, and by applying a potential of — 300 volts across the subsidiary gap through which the beam passes before entering the accelerating gap.

6. The Negative Ion Source

Negative hydrogen ions are obtained from a radio frequency source which has been modified to give an optimum yield of negative rather than positive ions. In a conventional radio frequency source the positive ions are extracted from the discharge through an aluminium canal which restricts the flow of gas from the source but allows sufficient current to be drawn from the plasma. Protons, extracted from the discharge,

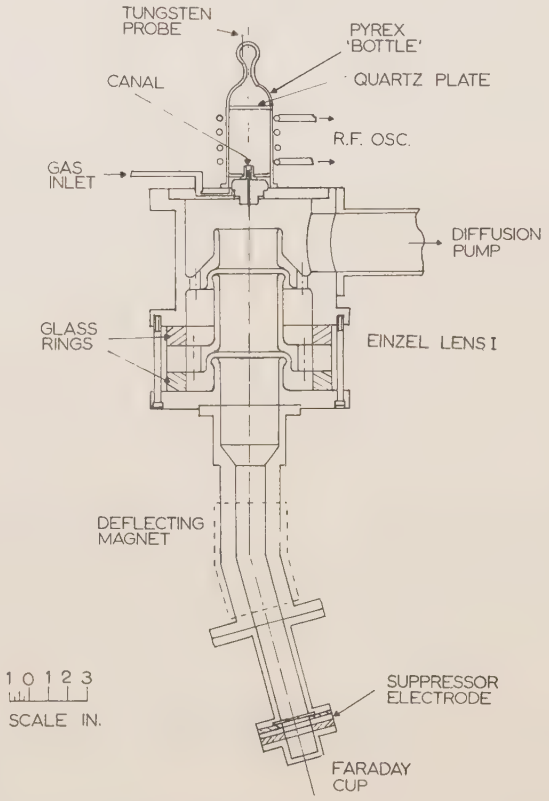

Fig. 4. The negative hydrogen ion source and test arrangement.

undergo charge changing collisions with the neutral gas atoms in the canal. When the product of canal length and mean gas pressure in the canal is high enough a large number of the protons become neutral atoms and a smaller number pick up further electrons to become negative ions. This process must be reduced to a minimum in a positive ion source to avoid the loss of ions but must be enhanced in the present case by making the canal as long as possible and working at the highest possible gas pressure.

A schematic drawing of the ion source is shown in fig. 4. The design is very similar to that

described by Goodwin[7]) for positive ions, and to that by Khirnyi[8]) for negative ions. A discharge is induced in the pyrex "bottle" by the radio frequency field of the surrounding coil. Power is obtained at a frequency of about 20 Mc/s from a single valve self-excited oscillator. The power input to the oscillator is normally about 500 watts but can be as high as 1000 watts. Hydrogen gas is fed in through a side tube in the base plate. The gas pressure is normally about 45 microns Hg; this pressure was measured by a MacLeod gauge with no r.f. power or probe volts applied. Protons are extracted from the plasma and directed into the canal by applying a positive potential to the tungsten probe. It was found necessary to catch back streaming electrons from the canal on a quartz disc supported at the top of the bottle, since without this disc the envelope was frequently punctured by the formation of a "hot spot" on the glass.

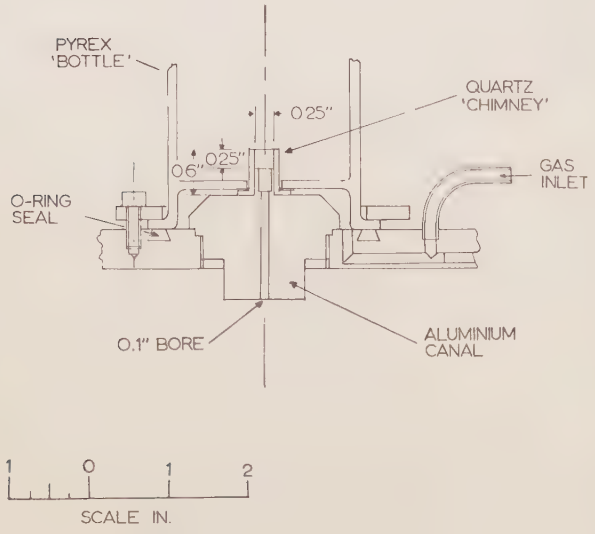

Fig. 5. Ion source canal details.

Details of the canal design are shown in fig. 5. The length of the canal is 4.5 cm, hence the total gas target thickness for protons entering the canal is approximately 100 micron·cm. The cross sections for the charge exchange processes of interest have been measured by several authors[9–12]) and the measured values indicate a maximum yield of 2 percent of the total beam as negative ions in the energy region of 7.5 to 15 keV. The present source is operated with a probe potential near 7.5 keV and the cross sections at this energy are given in table 1. The fractions of an initially pure proton beam which are in each of the charge states + 1, 0, and — 1 can be calculated as a function of the thickness of gas traversed, and these are shown in fig. 6. It can be seen that a gas target thickness of at least 100 micron·cm is required to obtain the full yield of H^- ions.

Table 1

Cross section	Reported values (cm^2/atom)	Reference	Values adopted in the present calculations (cm^2/atom)
Electron Capture σ_{10}	$4.64 \pm 0.46 \times 10^{-16}$	[9])	$4.32 \pm 0.11 \times 10^{-16}$
	$4.20 \pm 0.52 \times 10^{-16}$	[11])	
	$4.10 \pm 0.41 \times 10^{-16}$	[12])	
	$4.40 \pm 0.66 \times 10^{-16}$	[10])	
Electron loss σ_{01}	$0.440 \pm 0.044 \times 10^{-16}$	[12])	$0.440 \pm 0.044 \times 10^{-16}$
Electron attachment σ_{0-1}	$0.120 \pm 0.012 \times 10^{-16}$	[12])	$0.120 \pm 0.012 \times 10^{-16}$
Electron detachment σ_{-10}	$5.10 \pm 0.51 \times 10^{-16}$	[12])	$5.75 \pm 0.41 \times 10^{-16}$
	$6.40 \pm 0.64 \times 10^{-16}$	[10])	

[7]) L. K. Goodwin, Rev. Sci. Instr. **24** (1953) 635.
[8]) Y. M. Khirnyi, Pribory I Tekh. Eksp., No. 2 (1958) 51.
[9]) J. P. Keene, Phil. Mag. **40** (1949) 369.
[10]) A. C. Whittier, Can. Journ. Phys. **32** (1954) 275.
[11]) J. B. H. Stedeford and J. B. Hasted, Proc. Roy. Soc. A **227** (1955) 466.
[12]) P. M. Stier and C. F. Barnett, Phys. Rev. **103** (1956) 896.

The performance of the source was determined by the test arrangement shown in fig. 4, which included both einzel lens I and deflection magnet. The negative ion beam was measured in a faraday cup, which had a secondary electron einzel lens introduced a magnification of 3 times, so that the Lagrange product for the source was 0.0015 $MeV^{\frac{1}{2}} \times$ cm $\times$ radians. A negative hydrogen ion current of 10 μA was normally obtained.

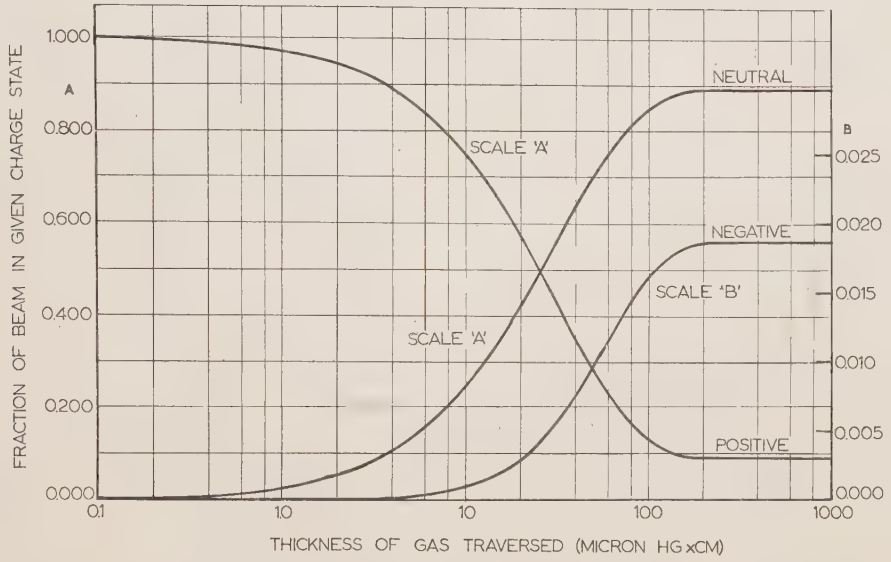

Fig. 6. Fractions of a 7.5 keV hydrogen ion beam in each of the given charge states as a function of the thickness of hydrogen gas traversed. The initial beam consists of protons only.

suppression electrode held at a potential of — 300 volts. The beam was focused on to the quartz disc at the back of the cup so that an estimate could be made of the beam parameters. The surface of the quartz was discharged by a copper gauze screen. At a probe potential of 6 kilovolts the spot diameter was seen to be less than 1 cm. The divergence of the beam was restricted by the canal to 0.06 radians, and the

7. Performance of the Complete Injector

The negative ion injection system was completed and assembled separately from the remainder of the accelerator, and measurements made to determine the beam parameters. The beam diameter was measured at the position corresponding to the object point for the first accelerating tube by observing the luminous glow on a quartz screen. This screen was

Table 2

Injection energy	Beam diameter	Beam divergence	Lagrange product cm·rad·$(MeV)^{\frac{1}{2}}$	Transmission through stripper tube	Final proton energy
40 keV	5.0 mm	0.007 radians	0.0007	0.3	4.0 MeV
110 keV	2.4 mm	0.010 radians	0.0008	1.0	11.0 MeV
		Calculated requirements			
40 keV	1.4 mm	0.048 radians	0.0013	1.0	4.0 MeV

covered with a fine copper mesh in order to avoid spurious affects due to the charging of the quartz surface. The divergence of the beam was measured by replacing the quartz screen with an aperture 2 mm in diameter, and then viewing the illumination of a further quartz screen placed in line with the beam 30 cm away. The results obtained are shown in table 2. The observational errors are estimated at $\pm$ 30 per cent.

The ideal conditions have not been achieved and this is principally due to the finite aperture of einzel lens III. The observed beam diameter would decrease if the beam crossover point between lens II and lens III were moved closer to lens II. This would result in a loss of beam current on the aperture of lens III, and the extra voltage required on lens II would exceed the safe limit of the installed insulation of this lens. For these reasons the final adjustments have been left until the injector is working on the accelerator.

The beam remained focused on the quartz screen at the object point for all injection energies from 40 to 120 keV. However, on moving the screen axially it was found that the "focused spot" existed over a region of $\pm$ 1.0 inch on either side of the required position and this result indicated that some spherical aberration was present in the einzel lenses.

The overall performance of the injector was considered to be satisfactory for initial use on the accelerator.

The authors would like to acknowledge the valuable assistance given by Mr. C. E. Goble in the assembly of the injector, and also that given by Mr. D. P. Hammond in the early development stages and that of Mr. N. Coles in mechanical design.

NUCLEAR INSTRUMENTS AND METHODS 4 (1959) 129–132; NORTH-HOLLAND PUBLISHING CO.

A MICROSCOPE FOR THE SCANNING OF NUCLEAR RESEARCH EMULSIONS

A. G. EKSPONG and B. E. RONNE

Institute of Physics, Uppsala, Sweden

Received 23 February 1959

A microscope which can handle rather large plates is described. The area which can be reached without moving the plate is 25 × 15 centimeters. The largest plate which can be examined on the microscope must have one side less than 49 centimeters.

The use of the microscope is made comfortable by suitably constructed manual controls. The stage can be moved rapidly and precisely.

1. Introduction

The development within high energy physics has led to the use of ever larger nuclear research plates. Extremely large plates may have to be cut before examination in microscopes starts. However, one usually wants to be able to examine as large plates as is possible without having to cut them.

The objects under investigation in high energy physics are small only in two dimensions. As the commercial microscopes used for scanning are built mainly for an examination of objects small in all three dimensions, they are usually equipped with inconveniently small stages. In many laboratories this difficulty has been to some extent overcome by rebuilding the stages or enlarging the existing stages.

At our Institute, we decided about two years ago to build completely new stages for six scanning microscopes. The desired stages should be big enough to handle plates of such sizes as were used then and also larger plates for future needs. As any prophecy about the future is bound to be somewhat uncertain, we considered only that 36 centimeters is a natural length, because this corresponds to a mean free path for highly interacting particles, like pions, in present day emulsions. The size of the microscope should also be convenient for use in daily work. Our final decision was to build a stage of dimensions 36 × 30 centimeters. The stage is horizontal. This means that plates larger than the stage dimensions can be examined but with much reduced convenience.

A further point which was considered important was that the manual controls and the eyepieces should be comfortably located. Finally, we wanted to have a construction that is accurate enough for precise measurements of ranges, angles, grain densities, and coordinates.

2. Description of the Microscope

The instrument is shown in fig. 1. The optical equipment is commercial and consists of body, tube, condenser, mirror, and lamp. The body has a revolving nose piece, which has objectives of 10 ×, 25 ×, 53 × (oil immersion), and 100 × (oil immersion) magnification, and the tube has a binocular equipment and 10 × oculars. The eyepiece goniometer seen in the picture was built at the Institute†.

The base plate, microscope arm, stage, substage, lampholder, and the controls were designed and built at our Institute. Most of these parts were cast in an aluminumalloy (silumin) and then finished in our workshop.

The stage consists of two frames. The lower one is movable in the y-direction (away from

† We wish to thank the Gustaf Werner Institute for Nuclear Chemistry, Uppsala, for the drawings of the goniometer.

the observer) and the upper one in the x-direction. The nuclear plate rests on the upper frame in a special plate holder to be seen in fig. 1. Each frame was cast as a unit but can be regarded as consisting of four bars 30 mm wide. The upper frame was finished to a thickness of 16 ± 0.005 mm and the lower one to a thickness of 21 ± 0.005 mm. Both frames slide on steel balls. On one side of each frame, there are 12 balls between two carefully ground steel bars with V-shaped groves. On the opposite side there is one steel ball between two plane steel bars. The steelballs were obtained with an extremely small tolerance; the diameter is 12.697 mm $\pm$ 0.1 μm. The tolerance is both between balls and between various diameters of the same ball†.

The lower stage frame, which carries the upper one, rests on two straight supports fastened to the large base plate, which is in turn supported at three points by the table. The lower frame measures 60 cm in the x-direction and 30 cm in the y-direction, and the upper frame is 36×30 cm.

The movements of the stages are controlled by ordinary precise micrometer screws. As the screws cannot cover the entire range, we have constructed a type of coarse adjustment, which is shown in fig. 2. The x-stage can move 25 cm and the y-stage 15 cm. The coarse adjustments of the stages are obtained by means of a steelbar, which slides in bearings fastened in the stage below and support below, respectively. The steel bars are furnished with jags at every centimeter. The distance between every two jags is 1 ± 0.003 cm, where the error comes from imperfections. A spring loaded pin in a carefully grounded case couples each stage to the bar belonging to it. The pin is fitted into the desired jag. This type of coarse adjustment is very convenient for rapid relocation of known events

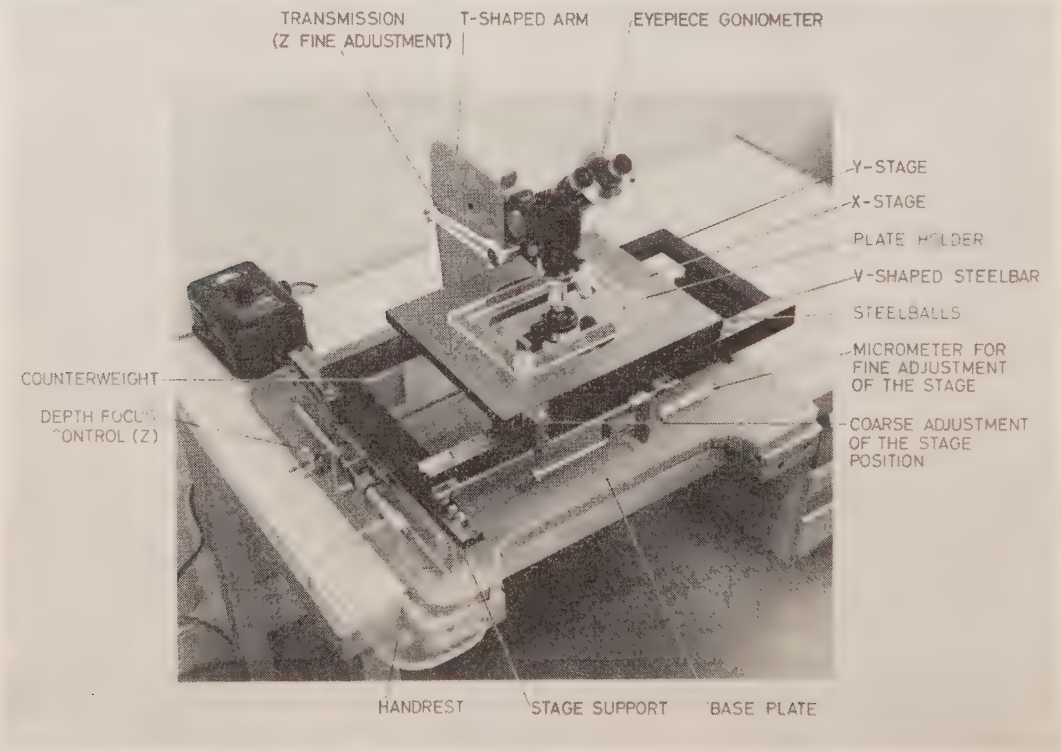

Fig. 1. The microscope for nuclear plate scanning.

† We wish to thank Aktiebolaget Svenska Kullager (SKF), Göteborg, Sweden, for their generosity in supplying us with the accurate steel balls.

in the neighbourhood of the optical axis. The fine adjustment is coupled to the steel bar, as in fig. 2, and consists of a micrometer screw and a spring loaded bar, which counteracts the screw.

A track can be followed about 40 mm with the aid of the micrometer screws. After moving the coarse adjustment one or several steps, one can then easily find the same point of the track and go on along the track.

The coarse and the fine adjustments in the

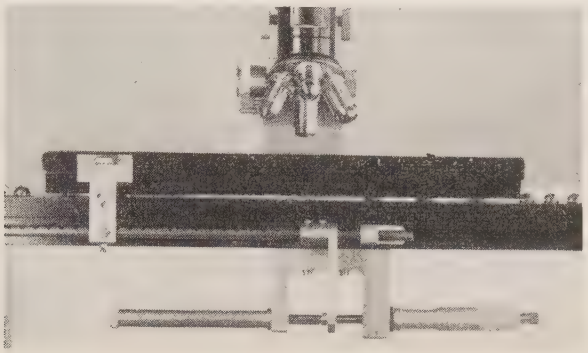

Fig. 2. The coarse and fine adjustments of the stage.

z-direction (perpendicular to the stage plane) are located in the body of the commercial part of the microscope. As this position of the fine adjustment is extremely uncomfortable for steady use, we have transferred the rotation of a horizontal axis, conveniently placed above the base plate, to the body by means of a transmission band. The axis is provided with control wheels at each end. It is then possible to manage the z-screw with either hand.

The arm of the microscope is T-shaped in order to obtain strength and small weight. It is fastened to an accurately ground part of the base plate by bolts. The two stage supports are also fastened to the base plate in the same manner.

It has proved necessary to attach felt-covered dampers on the right side of the lower stage to moderate its vibrations. Without these dampers there occur disturbing vibrations, which make observations in high magnification difficult. With dampers in place, mechanical disturbances originating in the surroundings (the building, the street, and etc.) do not cause any excessive vibrations in our microscopes.

3. Properties of the Microscope

The microscopes were designed and built for use in scanning work and for simple measurements. Ranges of tracks several centimeters long can be measured to an accuracy of about 5 μm. Small distances are measured much more accurately by the use of eyepiece scales. Angles can be measured with the goniometer to about 0.5°. The area, which can be reached without moving the plate, is 25 $\times$ 15 centimeters. At present our largest plates measure 22.5 $\times$ 15 centimeters. The distance between the optical axis and the microscope arm sets a limit to the absolute maximum size of plates to about twice this distance or 49 cm.

The stage cannot be used in multiple scattering measurements in its present condition. The stage noise (in the second differences in y) is 0.18 μm for a cellsize of 50 μm and grows to 0.40 μm for a cellsize of 500 μm. Good multiple scattering microscopes should have a stage noise $\leq$ 0.10 μm. We believe that the main contribution to the stage noise in our microscope originates in the unevenness of the V-shaped steel bars. If the bars had been lapped, the noise should probably have been reduced. The fact that the stage is not of a kinematical design contributes also (it has to many constraints). For scanning work and simple measurements the present noise is, of course, of no importance.

The first microscopes which were built have now been in steady use for about two years. Scanners find them comfortable to use. The position of the manual controls are within easy

reach, and the stage moves smoother than in most other scanning microscopes, partly because of the micrometer screw control of the stage.

Acknowledgements

Without the vigorous support of Prof. Kai Siegbahn the completion of these microscopes could not have been accomplished at the right time when our emulsion group was expanding. We would like to express our deep gratitude to him for all help with various aspects of the project.

Our thanks are extended to Mr. Gösta Larsson for his skilful craftsmanship and also for his solutions to some of the mechanical problems in the design. We would also like to thank Dr. S. Nilsson and Mr. S. Johansson for help in design work, and Mr. L. Eriksson for complete drawings.

The work was supported in part by a contract with the Air Research and Development Command, U.S.A.F., through its European Office.

NUCLEAR INSTRUMENTS AND METHODS 4 (1959) 133–139; NORTH-HOLLAND PUBLISHING CO.

BEMERKUNGEN ZU EINEM SCHNELLEN 20-KANAL-IMPULSHÖHENANALYSATOR

M. BONITZ† und E. J. BERLOWITSCH

Physikotechnisches Institut der Akademie der Wissenschaften der UdSSR, Leningrad

Eingegangen am 15. Februar 1959

A high-speed twenty-channel pulse analyzer of the Gatti type with a resolution better than 1 μsec is described. Improved discriminators allow the introduction of a new method for increasing the practical number of channels to a multiple of twenty.

1. Einführung

Impulshöhenanalysatoren der verschiedensten Typen sind heute in der Kernphysik gebräuchlich. Erwähnt seien davon hier nur Geräte, welche mit vorgespannten Diskriminatoren und Antikoinzidenzschaltungen arbeiten[1]), weiter solche, die das Wilkinson-Sanin-Prinzip der Amplituden-Zeit-Umwandlung benutzen[2,3]), und schliesslich ein Analysator, bei dem die Einsortierung der Impulse nach dem Chronotronprinzip erfolgt[4]). Alle diese Geräte haben trotz ihrer Verschiedenartigkeit ein Merkmal gemeinsam: ein Impuls, welcher in der Zeit der Aufnahmebereitschaft am Analysator erscheint, wird auch registriert. Fällt er durch unvermeidliche Instabilitäten nicht in "seinen" Kanal, so erfolgt die Registrierung im benachbarten Kanal. Verschiebt sich eine Kanalgrenze, so ändern sich entsprechend die Kanalbreiten der benachbarten Kanäle. Die unerwünschte Folge solcher Verschiebungen ist eine Verzerrung der aufgenommenen Spektren. Der Verringerung und Kleinhaltung der Kanalgrenzenschwankungen wird daher überall viel Aufmerksamkeit gewidmet.

Ein neues Analysatorprinzip, welches den Einfluss der Kanalgrenzen auf die Kanalbreite beseitigt, wurde von Gatti und Piva[5]) vorgeschlagen und von Gatti[6]) bzw. Colombo, Cottini und Gatti[7]) verwirklicht. Ihr Gerät arbeitet mit vorgespannten Diskriminatoren. Die Vorspannungen legen dabei lediglich die Kanalpositionen fest, während die Kanalbreite durch ein für alle Impulse gleiches Informationselement bestimmt wird. Dieses "Gatti-Prinzip" liegt auch unserem Gerät zugrunde.

Analysatoren mit vorgespannten Diskriminatoren haben den Vorteil schnell zu sein, d.h. eine Totzeit von nur wenigen μsec aufzuweisen. Allerdings wäre es wegen der grossen Röhrenzahl unwirtschaftlich, mit der Kanalzahl höher als etwa 30 zu gehen. Um mit solchen Wenigkanalanalysatoren grössere Spektren mit hinreichender Auflösung messen zu können, schaltet man ihnen gewöhnlich einen Fenster- (oder Expander-) Verstärker vor, welcher den jeweils zu untersuchenden Bereich des Spektrums in den Messbereich des Analysators rückt. Die Zeit der Messung vergrössert sich dabei auf das k-fache, wenn man k Teile des Spektrums nacheinander aufnimmt, angesichts der Schnelligkeit, mit der viele Wenigkanalanalysatoren zu arbeiten vermögen, ist das zu verantworten. Auch das hier beschriebene Gerät enthält einen Fensterverstärker.

Aus dem Gattiprinzip folgt nun eine Möglich-

† Vom Lehrstuhl für Kernspektroskopie an der Technischen Hochschule Dresden, DDR.

[1]) W. C. Elmore and M. Sands, Electronics Experimental Techniques (McGraw Hill, 1949) 241.

[2]) D. H. Wilkinson, Proc. Camb. Phil. Soc. **46** (1950) 508.

[3]) A. A. Sanin, Uspechi fis. nauk **4** (1954) 619.

[4]) G. R. Kartaschov, Pribori i technika experimenta, No. 1 (1958) 73.

[5]) E. Gatti and F. Piva, Nuovo Cimento **10** (1953) 984.

[6]) E. Gatti, Nuovo Cimento **11** (1954) 153.

[7]) S. Colombo, C. Cottini and E. Gatti, Nuovo Cimento **5**, No. 3 (1957) 748.

keit, auch ohne die Anwendung eines Fensterverstärkers die Zahl der Messpunkte auf das Doppelte, Dreifache usw. zu erhöhen und damit die Messgenauigkeit des Analysators zu verbessern. Dies wird verständlich, wenn man sich daran erinnert, dass in Analysatoren vom Gatti-Typ die Kanalbreite d nicht gleich dem Kanalabstand D zu sein braucht. Wir besprechen anschliessend das Gattiprinzip und die sich daraus ergebende Methode zur Erhöhung der praktischen Kanalzahl. Dann folgt eine kurze Beschreibung unseres Analysators.

Höhe d versehene Impuls werde A genannt. "A" geht nun auf die ansteigend vorgespannten Diskriminatoren D_i ($i = 1, 2 \ldots 20$). Zur gleichen Zeit mit dem Zusatzimpuls wird im Impulsumformer ein Synchronimpuls "B" erzeugt. Die Ausgangsimpulse der Diskriminatoren müssen Koinzidenzstufen K_i passieren, welche vom Synchronimpuls B aufgesteuert werden. Aus der Gleichzeitigkeit von Zusatzimpuls und Synchronimpuls B folgt, dass der Ausgangsimpuls eines Diskriminators seine Koinzidenzstufe nur dann passieren und zur Registrierung

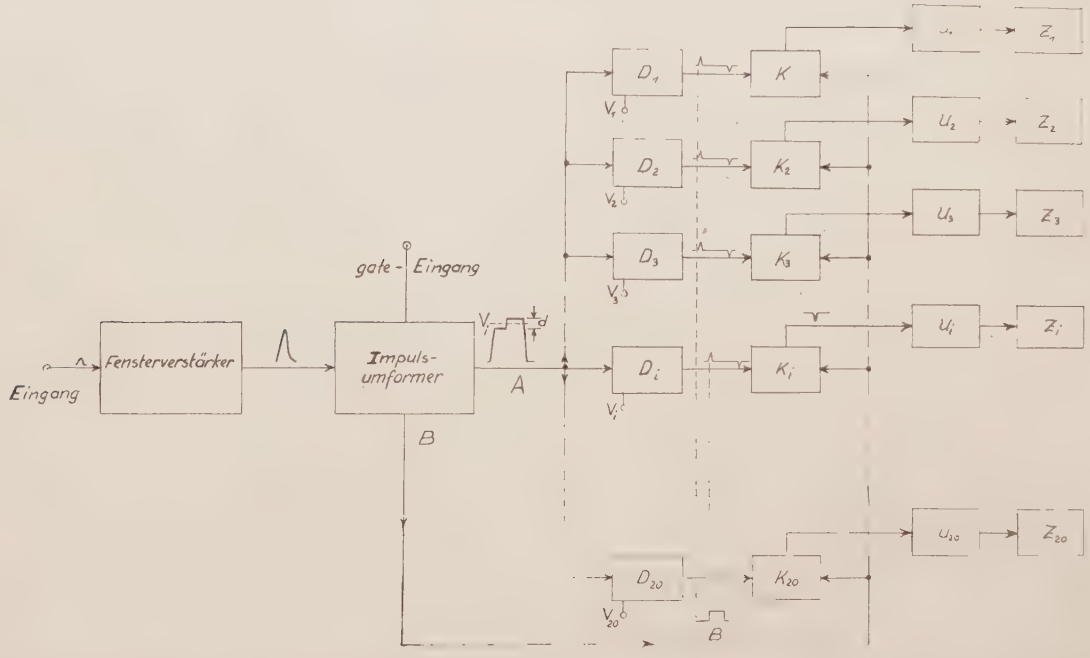

Fig. 1. Blockschaltbild des Analysators. D_i = Diskriminatoren, K_i = Koinzidensztufen, U_i = Untersetzer, Z_i = Zähler, $i = 1, 2, 3 \ldots 20$. Die Impulsregistrierung erfolgt im i-ten Kanal.

2. Wirkungsweise des Gerätes

2.1. DAS ANALYSATORPRINZIP VON GATTI

Der positive Eingangsimpuls geht nach der Verstärkung im Fensterverstärker in einen Impulsumformer (Fig. 1). Dort wird er unter Beibehaltung seiner Amplitude gestreckt. Nach ein bis zwei μsec wird diesem verlängerten Impuls ein Rechteckimpuls der Amplitude d aufaddiert. d ist für alle Impulse gleich und stellt das Informationselement "Kanalbreite" dar. Der verlängerte und mit dem Zusatzimpuls der

in seinen Zähler Z_i gelangen kann, wenn der Diskriminator vom Zusatzimpuls getriggert wurde. Alle niedriger vorgespannten Diskriminatoren, die von kleineren Impulsen A, und zwar von deren Vorderfront, getriggert wurden, geben ihre Ausgangsimpulse zu früh, sodass in diesen Kanälen keine Registrierung erfolgen kann. Anders ausgedrückt: hat ein Kanal die Vorspannung V_i, so werden in ihm alle Impulse registriert, deren Amplitude zwischen $(V_i - d)$ und V_i liegt.

Wir haben d Kanalbreite genannt, aber dieser Ausdruck darf nicht im herkömmlichen Sinn als Differenz zweier Kanalpositionen verstanden werden. Wir bemerken, dass d unabhängig ist von der Position der übrigen Kanäle—die Registrierung würde genauso erfolgen, wenn es gar keine anderen Kanäle gäbe (Fall des Einkanalanalysators[5])). Daraus ergibt sich eine interessante Konsequenz, die kurz beschrieben werden soll.

2.2. ERHÖHUNG DER ZAHL DER MESSPUNKTE

Nach Fig. 2 ergibt sich folgendes Bild der Impulsregistrierung: aus einem Impulsspektrum werden nur solche Impulse registriert,

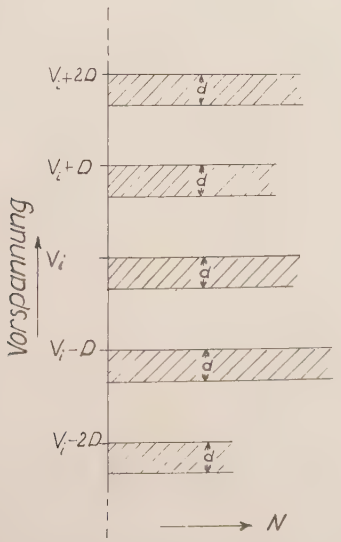

Fig. 2. Zur Methode der Erhöhung der Zahl der Messpunkte. V_i = Vorspannung des i-ten Diskriminators, D = Abstand benachbarter Kanäle, d = Kanalbreite.

welche in die schraffiert gezeichneten Streifen der Breite d fallen. Die unschraffierten Streifen der Breite $(D - d)$ bleiben dagegen leer, alle Impulse mit den entsprechenden Amplituden werden nicht gezählt. Es liegt nahe, diese Gebiete zur Erhöhung der Zahl der Messpunkte bei der Messung eines Impulsspektrums auszunutzen. Das kann geschehen, wenn man bei jeder folgenden Messung die schraffierten Streifen um eine Breite d weiterrückt, sooft, bis nach n Messungen das ganze unschraffierte Gebiet überdeckt ist. Der Einfachheit halber haben wir hier $n \cdot d = D$ mit $n = 1, 2, \ldots$ angenommen, d kann aber auch kleiner als D/n sein.

Indem man entweder die Lage des Spektrums oder das System der Vorspannungen oder die Kanalbreite verändert, ergeben sich folgende Möglichkeiten zu einer Verschiebung der schraffierten Streifen:

a. Lage des Spektrums und Vorspannungssystem fest. Kanalbreite vergrössern auf $2d$, $3d$ usw. Von der Zahl der in diesen Kanälen der Breite $2d$, $3d$ usw. registrierten Impulse jeweils die Zahl der vorher in den Kanälen der Breite d, $2d$ usw. registrierten Impulse subtrahieren. Wenn man die gleiche Messdauer bei jeder erneuten Messung voraussetzen kann, erhält man so jeweils die Zahl der Impulse in den um d weitergerückten Kanälen. Wir haben diese Methode angewandt, aber sie ist zeitraubender als die unter c. zu beschreibende.

b. Kanalbreite und Lage des Spektrums fest. Alle Vorspannungen V_i um d, $2d$ usw. verschieben. Diese Methode ist unhandlich.

c. Kanalbreite und Vorspannungssytem fest. Das Spektrum als Ganzes um d, $2d$ usw. verschieben. Diese Verschiebung wird etwa dadurch erreicht, dass man alle Ausgangsimpulse A mit Hilfe einer vorgespannten Diode im Ausgang des Impulsumformers um den Betrag der gewünschten Verschiebung verringert. Entsprechend rücken die Kanäle im Spektrum nach rechts um den Betrag d, $2d$ usw.

Fig. 3 zeigt zwei nach dieser Methode aufgenommene Spektren (Hg^{203}, Cs^{137}). Der Abstand D der Kanäle betrug 3 V. Die Breite eines Kanals war etwas kleiner als 1 V. Die Spektren wurden zweimal um 1 V verschoben, sodass sich 60 Messpunkte ergaben. An Hand von Fig. 3 überzeugt man sich, dass der Analysator linear arbeitet.

3. Beschreibung des Gerätes

3.1. IMPULSUMFORMER

Fig. 4 zeigt das Blockschaltbild des Impulsumformers, in dem die verstärkten Eingangsimpulse die Gestalt A erhalten. Das Herz des Impulsumformers ist der Impulsverlängerungskreis,

dessen Idee von Chase[8]) stammt und zu dessen Bau wir schaltungstechnische Anregungen von Patzelt[9]) verwendet haben.

In der Addierstufe erhält der verlängerte Impuls den Zusatzimpuls der Höhe d und geht dann über eine niederohmige Stufe (White-Kathodenfolger) auf die 20 Diskriminatoren.

Im untersten Teil des Blockschaltbildes findet man drei Signalgeber, die in zeitlich richtiger Einsatzzeitpunkt der Impulsblockierung bestimmt das Auflösungsvermögen des Analysators, wenn man unter Auflösungsvermögen den kleinsten zeitlichen Abstand versteht, den zwei Impulse haben dürfen, ohne dass der zweite Impuls die Registrierung des ersten fehlerhaft macht. Das Auflösungsvermögen beträgt in unserem Gerät weniger als 1 μsec. Der dritte Signalgeber liefert gleichzeitig zwei Im-

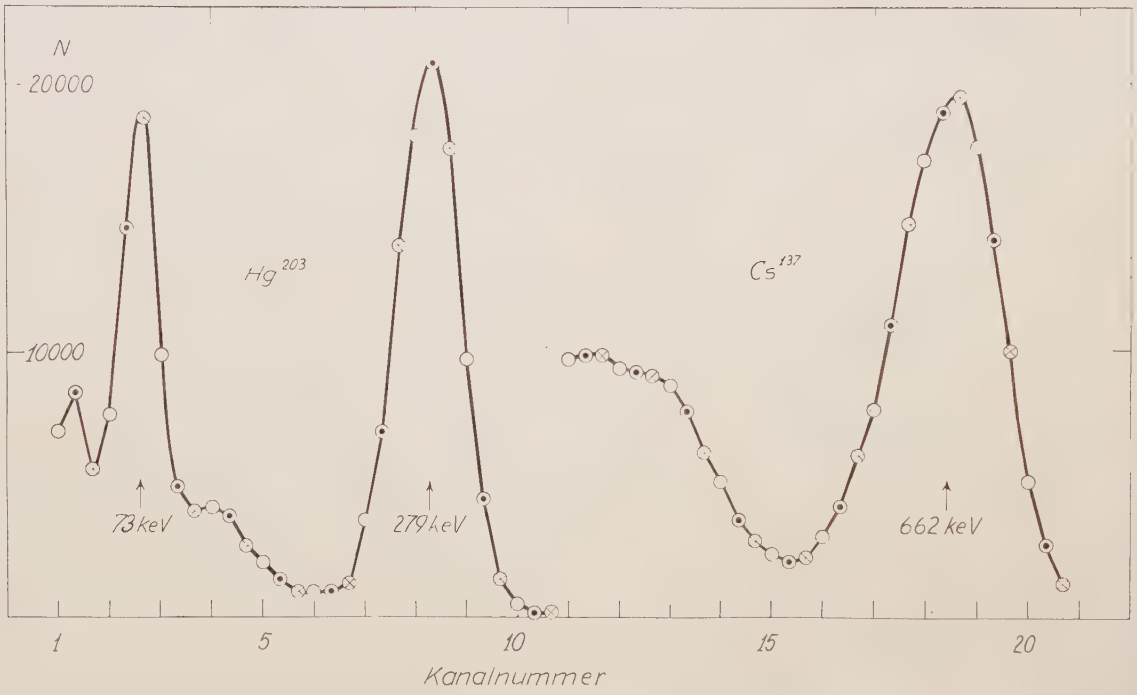

Fig. 3. Spektren von Hg^{203} und Cs^{137}. Die mit ○, ⊙ und ⊗ bezeichneten Messpunkte gehören jeweils zu einer Messung mit der entsprechenden Verschiebung des Spektrums von 0, 1 und 2 V.

Reihenfolge Steuerimpulse abgeben. Der erste Signalgeber legt die Dauer des verlängerten Impulses fest. Diese Dauer ist zugleich die Totzeit des Analysators, d.h. die Zeit, in der Impulse nicht registriert werden. Sie ist regelbar von 4–25 μsec. Der zweite Signalgeber dient der Impulsblockierung, d.h. nachdem der Eingangsimpuls sein Plateau erreicht hat, wird der Impulsverlängerungskreis solange gesperrt, bis der Zusatzimpuls der Höhe d vorüber ist. Der

[8]) R. L. Chase, Brookhaven Nat. Lab. Rep. 263 (T-42 1954)
[9]) R. Patzelt, Sitz. ber. d. Wr. Akad. d. Wiss. **165** (1956) 229.

pulse: den Synchronimpuls B, der auf die 20 Koinzidenzstufen geht, und einen Steuerimpuls, der die Addierung des Zusatzimpulses (Höhe d und Länge etwa 2 μsec) auslöst. Die Ausführung der von den drei Signalgebern gesteuerten Operationen wird von drei Übertragungsstufen besorgt, deren Funktion im Blockschaltbild angegeben ist. Weiter ist ein Impulstor vorgesehen (gate). Der Analysator ist nur aufnahmebereit, solange ein negativer Impuls am Eingang des Impulstores liegt.

Der Impulsumformer arbeitet linear für Eingangsimpulse der Amplitude 1–75 V, die

maximalen Impulse müssen eine Mindestlänge von 0.75 μsec haben. Die Linearität wurde für Impulsfolgefrequenzen bis zu 10 kHz geprüft. In Fig. 4 ist jeweils die Röhrenzahl der einzelnen Stufen angegeben.

3.2. DISKRIMINATOREN UND KOINZIDENZSTUFEN

Zur Durchführung der in 2.2 beschriebenen Messmethode benötigt man Diskriminatoren, die alle die gleiche Empfindlichkeit besitzen. Diese Empfindlichkeit muss regelbar sein, damit Unterschiede in den Röhrenkennwerten ausgeglichen werden können. In Fig. 5 sieht man, dass wir in unseren Diskriminatoren Spannungsdiskriminierung und Triggerung voneinander getrennt haben, ähnlich wie dies in einer Arbeit von Park[10]) beschrieben ist. Dadurch ist es möglich, die Eingangsröhre des aus den Röhren R_1 und R_2 (beide 6Ж5П) bestehenden Triggers in leitendem Zustand zu halten. Die Diskriminierung wird von einer vorgespannten Germaniumdiode D2Ж besorgt. Die Potentiale E und F sind in allen Kanälen die gleichen, dabei ist $(F - E) = 4$ V. Die Vorspannungen werden unabhängig davon eingestellt, wobei stets $V_i \leqq E$ ist. Zwecks Einstellung gleicher Empfindlichkeit aller Trigger wird in allen Kanälen $V_i = E$ gesetzt und ein im Analysator erzeugter Eichimpuls anstelle des Impulses A auf jeden Kanal gegeben. Durch Regulierung des Potentiometers 1 MΩ in jedem Kanal kann man erreichen, dass die Empfindlichkeitsschwelle jedes Triggers gleich der Grösse des Eichimpulses (etwa 0.30 ± 0.01 V) wird. Durch Verringerung von $(F - E)$ könnte man die absolute Empfindlichkeit leicht auf 10 mV bringen. Aber wegen der Eigenkapazität der Sperrdiode von etwa 1 pF würden dann vor allem die höheren Kanäle vorzeitig, nämlich auf die Vorderflanke der Eingangsimpulse A ansprechen.

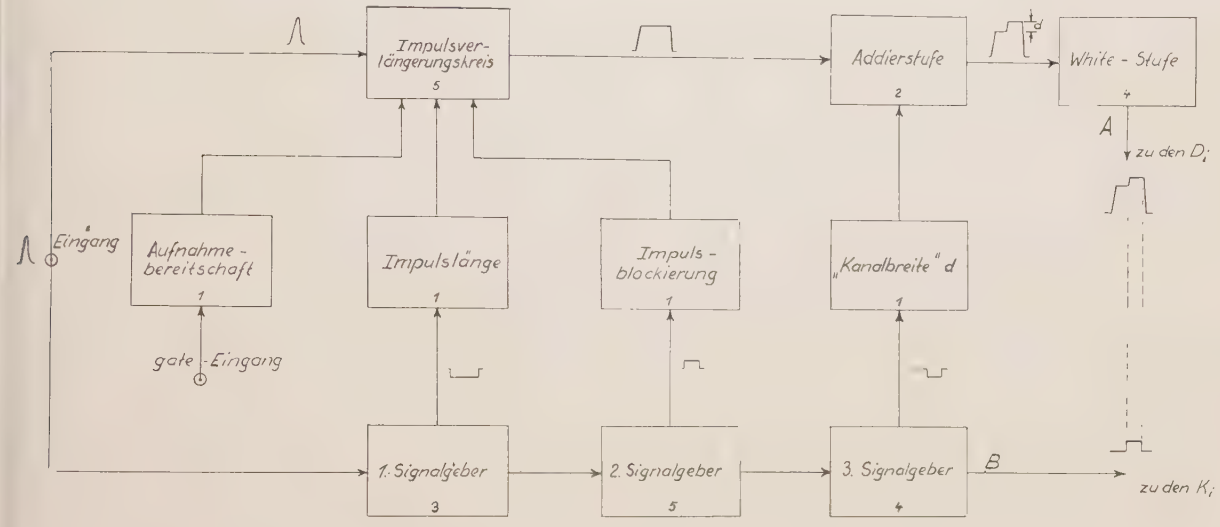

Fig. 4. Blockschaltbild des Impulsumformers.

Der rechteckige Triggerausgangsimpuls von etwa 4 μsec Dauer wird differenziert und geht auf die Röhre R_3 (6Ж2П), die als Koinzidenzstufe arbeitet. In R_3 ist sowohl das Steuergitter, als auch das Bremsgitter negativ vorgespannt. Das Bremsgitter wird durch den Synchroimpuls aufgesteuert. R_3 liefert daher seinen Ausgangsimpuls an den Untersetzer U_i dann und nur dann, wenn die Amplitude des Eingangsimpulses zwischen $(V_i - d)$ und V_i liegt.

In seiner zweiten Arbeit[7]) lässt Gatti dem Zusatzimpuls der Höhe d, der die Kanalbreiteninformation enthält, noch einen weiteren Zusatzimpuls vorausgehen, der bewirken soll, dass für alle Trigger gleiche Ansprechbedingungen

[10]) E. C. Park, Journ. Sci. Instr. 33 (1956) 257.

hinsichtlich der Form der Eingangsimpulse vorliegen. Infolge der Trennung von Diskriminierung und Triggerung hat sich bei uns eine solche Massnahme nicht nötig gemacht.

3.3. UNTERSETZER UND MECHANISCHE ZÄHLER

Die Untersetzer sind auf 2-fach bzw. 16-fach-Untersetzung einstellbar und bestehen jeweils aus Viererkaskaden der stromsparenden Doppeltrioden 6H2П. Infolge der ausgleichenden Wirkung der Untersetzer auf die Intervallstatistik registriert der Analysator 5 000–7 000 Imp/sec ohne Verzerrung des Spektrums.

Das Gerät enthält noch einen Diskriminator, der zur integralen Zählung aller Impulse A, die den Impulsumformer verlassen, eingesetzt wird.

3.4. MONTAGE

Der Analysator ist in drei Blöcken übereinander angeordnet, die nacheinander enthalten: Fensterverstärker und Spannungsteiler für die Erzeugung der Vorspannungen, Impulsumformer sowie Diskriminatoren und Koinzidenzstufen, Untersetzer und mechanische Zähler. Alle Chassis befinden sich wegen der erwünschten Kaminwirkung in vertikaler Lage. Die Kanäle sind untereinander austauschbar. Alle wichtigen Potentiale, insbesondere das Gitterpotential der Sekundäremissionspentode ЛП34 im Impulsverlängerungskreis, sind der schnellen Anzeige zugänglich.

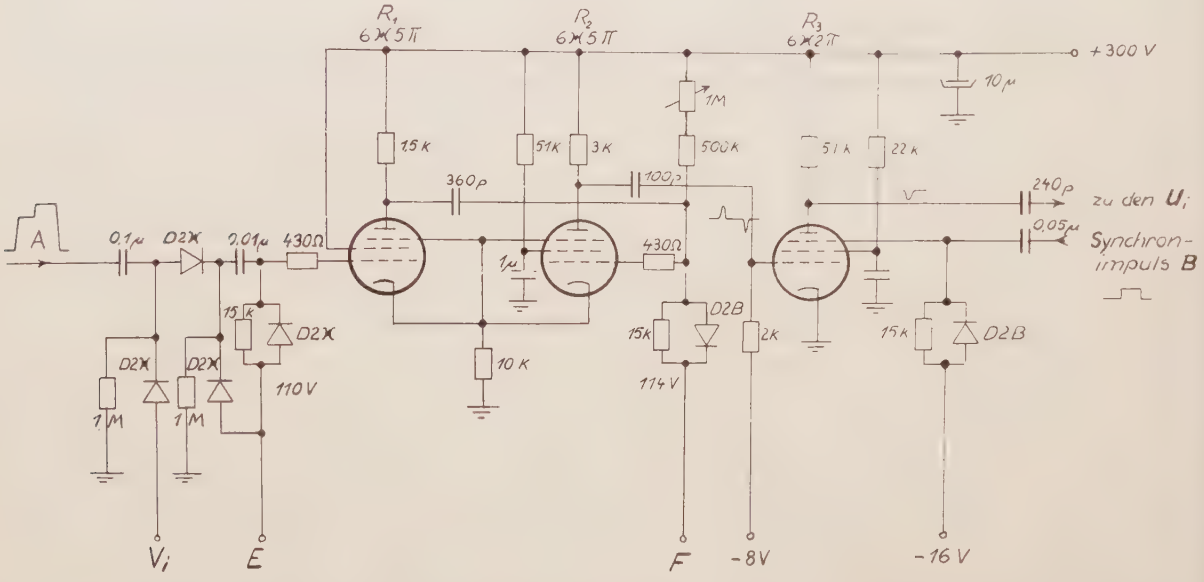

Fig. 5. Schaltbild des i-ten Kanals. Der Eingangsimpuls A, dessen Amplitude die Vorspannung $(E - V_i)$ der Germaniumdiode D2Ж übersteigt, triggert den aus R_1 und R_2 bestehenden Kreis, dessen differenzierter Ausgangsimpuls von der Koinzidenzröhre R_3 durchgelassen wird oder nicht, je nachdem ob er zur gleichen Zeit mit dem Synchronimpuls B an R_3 auftritt oder nicht.

4. Zusammenfassung

Die in 2.2 angegebene Methode der Erhöhung der praktischen Kanalzahl kann mit Vorteil in schnellen Analysatoren vom Gatti-Typ Verwendung finden, wenn man eine Verbesserung der Messgenauigkeit wünscht. Dabei bleibt das Spektrum als Ganzes und das Vorspannungssystem unverändert—die Verschiebung des Spektrums erfolgt lediglich um einen Betrag, der kleiner als ein Kanalabstand ist. Die Kanalbreite ist variabel und damit anpassungsfähig an das Mass, in dem eine Vergrösserung der Messgenauigkeit sinnvoll ist. Des weiteren hat man in dieser Variabilität eine bequeme Regelmöglichkeit der Zählgeschwindigkeit, wenn

die Intensität der Quelle nicht ohne weiteres verändert werden kann.

Baut man einen Analysator vom Gatti-Typ mit nur wenigen (z.B. 5) Kanälen auf, so lässt er sich ohne weiteres als Mehrpeakanalysator verwenden. Da die Kanäle in ihrer Position voneinander unabhängig sind, kann man sie einzeln beliebigen Bereichen eines Spektrums, in denen Peaks erwartet werden, zuordnen. Solch ein Mehrpeakanalysator hätte den Vorteil geringeren Aufwandes gegenüber Geräten, die aus mehreren Einkanalanalysatoren bestehen. Ein zusätzlicher Baustein ist lediglich der Impulsumformer.

NUCLEAR INSTRUMENTS AND METHODS 4 (1959) 140–150; NORTH-HOLLAND PUBLISHING CO.

NEUTRON TRANSMISSION PROBABILITY THROUGH A CURVED REVOLVING SLIT

M. MARSEGUERRA and G. PAULI

Comitato Nazionale per le Ricerche Nucleari, Roma

Received 11 January 1959

The formulas of a neutron burst transmitted by a revolving curved slit are analytically derived and are then applied to determine the distribution of the neutrons of the burst, after they have travelled a given distance.

1. Introduction

The shape of the neutron burst transmitted by a revolving "straight" slit has been extensively examined[1,2,3].

The purpose of this work is to determine the shape of the burst produced by a revolving "curved" slit. With this aim in mind, a detailed analysis has been carried out of the transmission of a collimated neutron-beam through a revolving curved slit. In sections 2, 3 and 4 the general expression of the burst shape is determined and is then specialized for the case of monochromatic neutrons transmitted by a parabolic slit. In sections 5, 6 the formulas for the burst shape are extended to the case of neutrons with a velocity spectrum $f(v)$, and the distribution shown by the neutrons after having travelled a distance d is determined and the velocity spread derived.

The formulas for the burst shape that are obtained can be specialized for the particular case of a straight slit.

2. The Mechanism of Burst Formation

A parallel beam of neutrons is incident upon a cylindrical shield, made of perfectly neutron-absorbing material and with the axis perpendicular to the neutron motion direction. The cylinder, of radius R, contains a slit defined by two cylindrical surfaces, α and β, with the directrices parallel to the cylinder axis (see fig. 1). The cylinder rotates around its own axis with constant angular velocity ω.

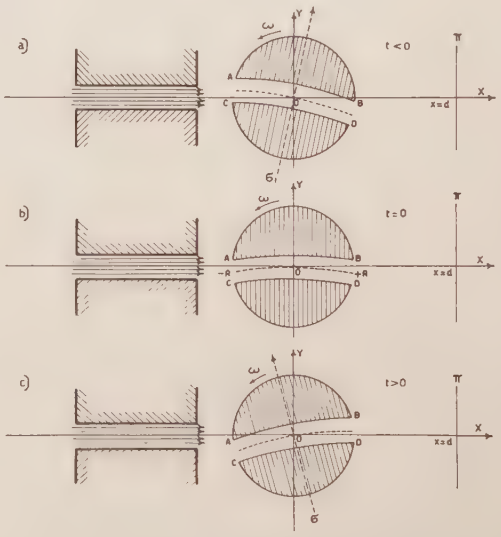

Fig. 1. A cross section of the cylindrical shield is shown, under the hypothesis that the surfaces α and β are both symmetric with respect to the center line of the cylinder and have the same symmetry plane σ, arbitrarily oriented. Curves AB and CD represent the cross-sections of the surfaces α and β with the (xy)-plane. The neutrons are supposed to have a uniform spatial distribution. The cylinder, the slit and the beam are supposed to be infinitely extended along the z direction.

In this way, the slit allows the passage of neutrons during short time intervals, Δt, following each other with constant frequency ν and consequently neutron bursts arise, which move towards the plane π placed across their path.

[1]) R. S. Stone and R. E. Slovacek, KAPL (1956) 1499.
[2]) V. I. Mostovoi *et al.*, P/640 Geneva Conf. (1955).
[3]) P. A. Egelstaff, AERE N/R 1131 (1953); Jour. Nucl. Energy 1 (1954) 57.

3. The General Expression of the Burst Shape

In this section an expression will be obtained of the function $P(v,t)$ giving the probability, per unit time, for a neutron to be transmitted through the revolving slit, v being the neutron velocity and t the time instant at which the neutron passes through the center of the slit.

Let us assume a rectangular coordinate system with the x-axis along the neutron motion direction and with the z-axis coincident with the rotation axis of the cylinder. The positive z-axis is chosen so that the cylinder rotates counterclockwise (see fig. 1). Further, let the time variable be equal to zero ($t = 0$) when the plane σ (see fig. 1) coincides with the plane $x = 0$. With reference to this coordinate system, let:

$$y_u = f_u(x) \tag{3.1}$$

and, respectively,

$$y_l = f_l(x) \tag{3.2}$$

be the equations for $t = 0$ of the curves AB and CD, cross-sections of the surfaces α and β with the plane $z = 0$ (see fig 1).

In order to define the position of the slit at $t \neq 0$, the angle ωt between the plane σ and the plane $x = 0$ may be used; as a consequence, negative angles will correspond to negative instants and positive angles to positive instants (see fig. 1). We assume the ratio between the size of the slit along the y axis and that along the x axis to be very small, i.e., of the order of 10^{-2}. This assumption implies that the time interval Δt, measuring the burst duration, may be considered as very small in comparison with the revolution time $2\pi/\omega$. For all angles ωt, where t is an instant of Δt, the following approximations are then allowed:

$$\sin \omega t = \operatorname{tg} \omega t = \omega t\,, \qquad \cos \omega t = 1\,. \tag{3.3}$$

During Δt, the x coordinates of the points on the surfaces α and β can therefore be considered unchanged and for any t of Δt the equations of the curves AB and CD read as follows:

$$y_u = f_u(x) + \omega t x \tag{3.4}$$

and respectively,

$$y_l = f_l(x) + \omega t x\,. \tag{3.5}$$

In particular, the two straight lines m and n defined by the preceeding equations for $x = t = 0$, that is,

$$y_u = f_u(0) \tag{3.6}$$

and, respectively,

$$y_l = f_l(0) \tag{3.7}$$

are fixed. This means that the neutron transmission probability vanishes outside of the interval $f_l(0) \leqslant y \leqslant f_u(0)$, and, therefore, the width of the collimator opening can be assumed to be equal to

$$h = f_u(0) - f_l(0)\,. \tag{3.8}$$

Let us now consider the neutrons of velocity v, transmitted by the revolving slit and passing through the center of the slit ($x = 0$) at an instant t of Δt. These neutrons have entered the slit, passing through the position $x = -R$, at the instant $t - R/v$, and will leave the slit, passing through the position $x = +R$, at the instant $t + R/v$. At the instant $t - R/v$, a number of neutrons are uniformly distributed inside a stripe of the plane $x = -R$, whose amplitude Δy is given by eq. (3.8). For clarity sake, we shall write $\Delta y_t(x)$, where the subscript t denotes the instant at which the neutrons will reach the position $x = 0$, while the variable x fixes the position at which Δy is calculated. Hence, the above considered amplitude will read as follows

$$\Delta y_t\,(-R) = h\,, \tag{3.9}$$

(see fig. 2). The fraction of neutrons that effectively enter the slit depend on the positions occupied at the time $t - R/v$ by the surfaces α and β defining the slit itself. These positions are indicated by eqs. (3.4) and (3.5), calculated for $t - R/v$, that is,

$$y_u = f_u(x) + \omega\,(t - R/v)\,x \tag{3.10}$$

and, respectively

$$y_l = f_l(x) + \omega\,(t - R/v)\,x\,. \tag{3.11}$$

Not all the neutrons that have entered the slit at the instant $t - R/v$ will be able to leave it at the instant $t + R/v$, since, during the transit time

$$(t + R/v) - (t - R/v) = 2R/v \tag{3.12}$$

some neutrons will be hitting the rotating slit walls, being consequently absorbed. The neutrons

which escape the chopping action of the slit walls and emerge from the slit at the time $t + R/v$, will be uniformly distributed inside a stripe of the plane $x = +R$. In order to calculate the amplitude $\Delta y_t(+R)$ of this stripe, a detailed analysis has to be performed of: (i) the neutron motion from the instant $t - R/v$, when the neutrons leave the plane $x = -R$ to move with constant speed v along the x direction, and (ii) the simultaneous motion of the

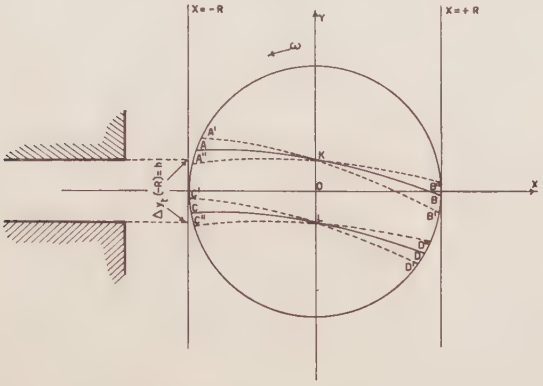

Fig. 2. Curves A′ B′, C′ D′; AB, CD; A″ B″, C″ D″ indicate the positions occupied by the surfaces α and β, defining the slit, at the time instants, $t - R/v$; t; $t + R/v$, respectively. In the situation represented in this figure, the neutrons that effectively penetrate into the slit at the time $t - R/v$ are the neutrons distributed inside the stripe whose amplitude is given by the difference between the ordinates of the points K and C′, that is, by the equation:

$$y_u(0, t - R/v) - y_1(-R, t - R/v) - f_u(0) - [f_1(-R) - \omega(t - R/v)R] .$$

slit walls which leave the positions (3.10) and (3.11) to rotate with constant angular velocity ω around the fixed straight lines m and n. These two motions are conveniently described by introducing a time parameter τ variable over the range of amplitude $2R/v$, given by eq. (3.12). Hence, the neutron motion between $x = -R$ and $x = +R$ is well described by the equation

$$x = -R + v\tau \tag{3.13}$$

and the simultaneous rotation of the slit walls is described by the equations

$$y_u = f_u(x) + \omega(t - R/v + \tau)x \tag{3.14}$$

and

$$y_1 = f_1(x) + \omega(t - R/v + \tau)x \tag{3.15}$$

for τ variable, as already stated, from zero to $2R/v$.

Eq. (3.13) represents a sheaf of planes parallel to the (y,z) plane. Each plane gives the position occupied by the neutron at the instant $t - R/v + \tau$. Equations (3.14) and (1.15) represent both a family of cylindrical surfaces with directrices parallel to the z-axis and generatrices expressed by eqs. (3.14) and (3.15), respectively. Each surface gives the position occupied by the slit walls at the instant $t - R/v + \tau$. The locus of the intersections between the planes of the sheaf of eq. (3.13) and the surfaces of eqs. (3.14) and (3.15) are two surfaces which visualize the chopping action performed by the slit walls upon the neutrons during the transit time given by eq. (3.12). The equations of the two surfaces are easily determined by elimination of the parameter τ between the eqs. (3.13) and (3.14) and between the eqs. (3.13) and (3.15). The following equations are obtained:

$$y_u^* = \frac{\omega x^2}{v} + \omega t x + f_u(x) \tag{3.16}$$

and

$$y_1^* = \frac{\omega x^2}{v} + \omega t x + f_1(x) , \tag{3.17}$$

which represent two cylindrical surfaces having the directrices still parallel to the z-axis and generatrices passing through the straight lines m and n.

The value $\Delta y_t(+R)$ of the amplitude $\Delta y_t(x)$ of the stripe belonging to the moving plane of eq. (3.13) and populated by the neutrons which have escaped the slit walls is clearly to be identified with the lowest value $[\Delta y_t(x)]_{min}$ assumed by $\Delta y_t(x)$ in the interval $|x| \leqslant |R|$.

In order to calculate $[\Delta y_t(x)]_{min}$, the lowest value, $[y_u^*]_{min}$, of eq. (3.16) and the highest value, $[y_1^*]_{max}$, of eq. (3.17) in the interval $|x| \leqslant |R|$ must be determined.

If

$$[y_u^*]_{min} \geqslant [y_1^*]_{max} \tag{3.18}$$

the amplitude $\Delta y_t(+R)$ has the expression given by the equation

$$\Delta y_t(+R) = [y_u^*]_{min} - [y_1^*]_{max} . \tag{3.19}$$

If, on the contrary,

$$[y_u^*]_{min} \leqslant [y_1^*]_{max} \tag{3.20}$$

the amplitude $\Delta y_t(+R)$ vanishes, that is,

$$\Delta y_t(+R) = 0 . \tag{3.21}$$

The number of neutrons incident on the rotating cylinder at $t - R/v$ is proportional to the amplitude $\Delta y_t(-R)$ and the number of neutrons emerging from it at the time $t + R/v$ is proportional to the amplitude $\Delta y_t(+R)$. As a consequence, the probability, per unit time, for a neutron of velocity v to be transmitted through the revolving system is given by the ratio

$$P(v,t) = \frac{\Delta y_t\,(+R)}{\Delta y_t\,(-R)} = \frac{\Delta y_t\,(+R)}{h}\,, \qquad (3.22)$$

t being the instant at which the neutron itself passes through $x = 0$.

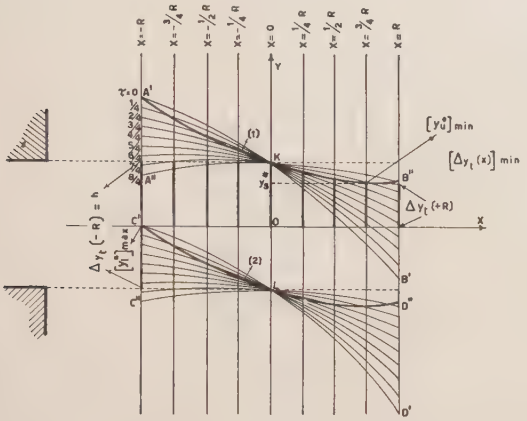

Fig. 3. Curves (1) and (2) are the cross sections of the chopping surfaces with the plane (x,y). The analytical expressions of these curves are given by eqs. (3.16) and (3.17). Nine positions of the moving plane eq. (3.13) and of the rotating slit walls eqs. (3.14) (3.15) are shown, being τ measured in terms of R/v. The two points K and L are intersections of the straight lines m and n with the plane $z = 0$.

4. The Shape of the Burst Transmitted by a Parabolic Slit

The equations (3.1) and (3.2) will now be specialized for the case of a parabolic slit.

With reference to a coordinate system rigidly connected with the rotating cylinder, let us calculate the path followed by a neutron having a given velocity v_0 and passing through the center of the slit at $t = 0$. There is no doubt that, if the slit has the curvature of this trajectory, a neutron of velocity v_0 will be transmitted through the slit itself. However, since the slit has a certain width h, a neutron with a velocity $v \neq v_0$ and passing through $x = 0$ at $t \neq 0$ will also be transmitted.

The above-considered neutron trajectory is easily found to have the following parametric equations:

$$X = v_0 t \cos \omega t\,, \qquad (4.1)$$

$$Y = -v_0 t \sin \omega t\,, \qquad (4.2)$$

where XY are the axes of the system referred to, rigidly connected with the rotating cylinder and so defined as to coincide with the xy system for $t = 0$. In virtue of the approximations expressed by eq. (3.3), the preceding equations can be written as follows:

$$X = v_0 t\,, \qquad (4.3)$$

$$Y = -v_0\,\omega t^2\,. \qquad (4.4)$$

By elimination of the variable t the cartesian equation of the trajectory is obtained:

$$Y = -\frac{\omega}{v_0} X^2\,. \qquad (4.5)$$

This equation can be written for $t = 0$ in terms of x and y, i.e.

$$y = -\frac{\omega}{v_0} x^2\,. \qquad (4.6)$$

Let us take the analytical expression given by eq. (4.6) to indicate the curves AB and CD. Hence, eqs. (3.1), (3.2) will have the following expressions:

$$y_u = f_u(x) = -\frac{\omega}{v_0} x^2 + \tfrac{1}{2}h \qquad (4.7)$$

$$y_l = f_l(x) = -\frac{\omega}{v_0} x^2 - \tfrac{1}{2}h\,, \qquad (4.8)$$

if the central width of the slit is assumed to be equal to h. Of course, the position of the slit defined by eqs. (4.7), (4.8) is not the only one which allows the passage of neutrons.

The neutrons indeed are also transmitted when the slit is upward, i.e., when the slit is rotated by 180 degrees from the downward position as described by the preceding equations. The transmission probability relative to the downward position will be discussed first.

The expression of the equations (3.16) and (3.17) are immediately obtained,

$$y_u{}^* = \frac{\omega x^2}{k} + \omega t x + \tfrac{1}{2}h \qquad (4.9)$$

and, respectively,

$$y_l{}^* = \frac{\omega x^2}{k} + \omega t x - \tfrac{1}{2}h\,, \qquad (4.10)$$

where

$$\frac{1}{k} = \frac{1}{v} - \frac{1}{v_0}\,. \qquad (4.11)$$

In eq. (4.11), v_0 is the velocity fixing, as already shown, the slit shape, while v is the velocity of the neutron whose transmission probability has to be calculated.

The velocity v may range from zero to infinity. We shall consider separately the two intervals

$$0 \leqslant v \leqslant v_0 \quad \text{and} \quad v_0 \leqslant v < +\infty\,, \tag{4.12}$$

that is, by means of eq. (4.11),

$$\text{(A)}: 0 \leqslant k < +\infty \quad \text{and} \quad \text{(B)}: -\infty < k \leqslant -v_0\,. \tag{4.13}$$

When the value of k belongs to the range (A), the two curves of eqs. (4.9) and (4.10) have both a minimum at the point of abscissa:

$$\xi = -\tfrac{1}{2}kt\,. \tag{4.14}$$

In order to determine the lowest value of the eq. (4.9) and highest value of eq. (4.10) for x varying between $-R$ and $+R$, the following cases have to be distinguished:

Case 1:

$$+R \leqslant \xi < +\infty\,. \tag{4.15}$$

In this case

$$[y_u^*]_{\min} = y_u^*(x = +R) \tag{4.16}$$

and

$$[y_l^*]_{\max} = y_l^*(x = -R)\,. \tag{4.17}$$

The hypothesis expressed by the eq. (4.15) is verified for

$$-\infty < t \leqslant \frac{2R}{k}\,. \tag{4.18}$$

Besides, the condition expressed by the eq. (3.18) is verified for

$$-\frac{R}{2\gamma} \leqslant t < +\infty \tag{4.19}$$

where

$$\gamma = \frac{\omega R^2}{h}\,. \tag{4.20}$$

Consequently

$$\Delta y_t\,(+R) = [y_u^*]_{\min} - [y_l^*]_{\max} = h + 2\omega t R\,, \tag{4.21}$$

and hence, for eq. (3.23),

$$P(k,t) = 1 + \frac{2\gamma}{R}t\,, \tag{4.22}$$

when t varies in the common part of the intervals defined by eqs. (4.18) and (4.19), that is:

$$\text{(I)}: \quad -\frac{R}{2\gamma} \leqslant t \leqslant -\frac{2R}{k}\,. \tag{4.23}$$

Note that the range (4.23) exists for

$$k \geqslant 4\gamma\,. \tag{4.24}$$

On the other hand, the condition (3.20) is verified for

$$-\infty < t \leqslant -\frac{R}{2\gamma}\,. \tag{4.25}$$

Thus,

$$\Delta y_t\,(+R) = 0 \tag{4.26}$$

and hence, for eq. (3.23),

$$P(k,t) = 0 \tag{4.27}$$

for t varying in the common part of the intervals expressed by eqs. (4.18) and (4.25), that is,

$$\begin{aligned} &\text{(II)}: \quad -\infty < t \leqslant -\frac{2R}{k} \quad \text{for} \quad k \leqslant 4\gamma\,, \\ &\text{(II')}: \quad -\infty < t \leqslant -\frac{R}{2\gamma} \quad \text{for} \quad k \geqslant 4\gamma \end{aligned} \tag{4.28}$$

(see fig. 4).

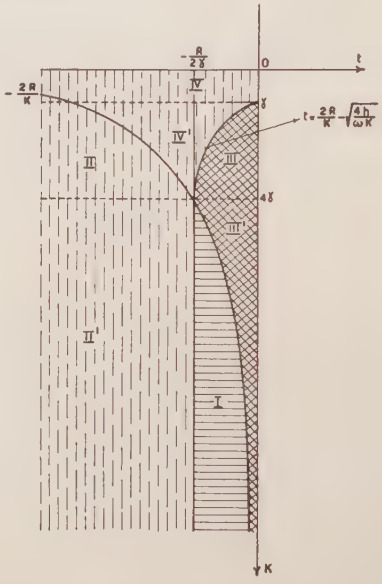

Fig. 4. Plot of the regions of the plane (t,k) where the transmission probability has the following expressions:

$P(k,t) = 1 + \frac{2\gamma}{R}t$

$P(k,t) = 1 - \frac{\omega k}{4h}\left(\frac{2R}{k} - t\right)^2$ $P(k,t) = 0$.

Case 2:

$$0 \leqslant \xi \leqslant +R\,. \tag{4.29}$$

In this case

$$[y_u^*]_{\min} = y_u^*\,(x = \xi) \tag{4.30}$$

and

$$[y_l^*]_{\max} = y_l^*\,(x = -R)\,. \tag{4.31}$$

The hypothesis expressed by the eq. (4.29) is verified for

$$-\frac{2R}{k} \leqslant t \leqslant 0\,. \tag{4.32}$$

In order to determine the intervals for t and k, where the conditions expressed by the equations (3.18) and (3.20) are complied with, a detailed analysis has to be performed of the function

$$\varphi(k,t) = h - \tfrac{1}{4}\omega k\left(\frac{2R}{k} - t\right)^2, \qquad (4.33)$$

which has been obtained by subtracting eq. (4.31) from eq. (4.30) and which expresses the difference $[y_u^*]_{min} - [y_l^*]_{max}$, i.e., as far as this difference is positive, the quantity $\Delta y_t(+R)$. for t varying in the common part of the intervals expressed by eqs. (4.32) and (4.34), that is,

$$\text{(III)}: \quad \frac{2R}{k} - \sqrt{\frac{4h}{\omega k}} \leqslant t \leqslant 0 \quad \text{for} \quad \gamma \leqslant k \leqslant 4\gamma\,, \qquad (4.36)$$

$$\text{(III')}: \quad -\frac{2R}{k} \leqslant t \leqslant 0 \quad \text{for} \quad 4\gamma \leqslant k < \infty$$

(see fig. 4). The amplitude $\Delta y_t(+R)$ vanishes by definition and, hence, for eq. (3.22), we have

$$(Pk,t) = 0 \qquad (4.37)$$

for t varying in the common part of the interval

TABLE 1

Expressions of the function $P(k,t)$ and of the corresponding ranges for k and t

(1)	(2)	(3)
k	$P(k,t)$	t
$0 \leqslant k \leqslant \gamma$	0	$-\infty < t < +\infty$
$\gamma \leqslant k \leqslant 4\gamma$	0	$-\infty < t \leqslant \frac{2R}{k} - \sqrt{\frac{4h}{\omega k}}$
	$1 - \frac{\omega k}{4h}\left(\frac{2R}{k} - t\right)^2$	$\frac{2R}{k} - \sqrt{\frac{4h}{\omega k}} \leqslant t \leqslant 0$
	$1 - \frac{\omega k}{4h}\left(\frac{2R}{k} + t\right)^2$	$0 \leqslant t \leqslant -\frac{2R}{k} + \sqrt{\frac{4h}{\omega k}}$
	0	$-\frac{2R}{k} + \sqrt{\frac{4h}{\omega k}} \leqslant t < +\infty$
$4\gamma \leqslant k < +\infty$	0	$-\infty < t \leqslant -\frac{R}{2\gamma}$
	$1 + \frac{2\gamma}{R}t$	$-\frac{R}{2\gamma} \leqslant t \leqslant -\frac{2R}{k}$
	$1 - \frac{\omega k}{4h}\left(\frac{2R}{k} - t\right)^2$	$-\frac{2R}{k} \leqslant t \leqslant 0$
	$1 - \frac{\omega k}{4h}\left(\frac{2R}{k} + t\right)^2$	$0 \leqslant t \leqslant \frac{2R}{k}$
	$1 - \frac{2\gamma}{R}t$	$\frac{2R}{k} \leqslant t \leqslant \frac{R}{2\gamma}$
	0	$\frac{R}{2\gamma} \leqslant t < +\infty$

The function $\varphi(k,t)$ has positive values for

$$\frac{2R}{k} - \sqrt{\frac{4h}{\omega k}} \leqslant t \leqslant \frac{2R}{k} + \sqrt{\frac{4h}{\omega k}}, \qquad (4.34)$$

and negative values outside of this interval.

It follows, from eq. (3.22), that

$$P(k,t) = 1 - \frac{\omega k}{4h}\left(\frac{2R}{k} - t\right)^2 \qquad (4.35)$$

defined by the eq. (4.32) and of the complementary interval so that defined by eq. (4.34), i.e.

$$\text{(IV)}: \quad -\frac{2R}{k} \leqslant t \leqslant 0 \quad \text{for} \quad 0 \leqslant k \leqslant \gamma \qquad (4.38)$$

$$\text{(IV')}: \quad -\frac{2R}{k} \leqslant t \leqslant \frac{2R}{k} - \sqrt{\frac{4h}{\omega k}} \quad \text{for} \quad \gamma \leqslant k \leqslant 4\gamma$$

(see fig. 4).

Cases 3 and 4:

$$-R \leqslant \xi \leqslant 0 \quad \text{and} \quad -\infty < \xi \leqslant -R\,.$$

In both cases 3 and 4, the expressions of the function $P(k,t)$ are those derived for cases 1 and 2, provided t is substituted by $-t$.

Let us now consider the case (B) of eq. (4.13) where k has negative values. It can be easily proved that the expressions of the transmission probability valid for the case (A) and shown in table 1 are still valid for the case (B), provided k in substituted by $|k|$.

and with $1/v + 1/v_0$ in the case (ii) of the upward position of the slit. The only calculation that has to be made consists in the determination of the interyals of the velocity v which correspond to the intervals of the quantity k appearing in table 1, column 1. It is however convenient to substitute the variable v with the variable ϑ defined by means of the following equation

$$\frac{v}{\gamma} = \vartheta\,,$$

where

$$0 \leqslant \vartheta < +\infty\,,$$

TABLE 2

Case (i): downward position of the slit

k	$-\infty$	-4γ	$-\gamma$	0	γ	4γ	$+\infty$
ϑ	$\vartheta_0 (> \vartheta_0)$	$\frac{4\vartheta_0}{4-\vartheta_0}$	$\frac{\vartheta_0}{1-\vartheta_0}$	0	$\frac{\vartheta_0}{1+\vartheta_0}$	$\frac{4\vartheta_0}{4+\vartheta_0}$	$\vartheta_0 (< \vartheta_0)$

Case (ii): upward position of the slit

k				0	γ	4γ	$\vartheta_0\gamma$
ϑ				0	$\frac{\vartheta_0}{\vartheta_0-1}$	$\frac{4\vartheta_0}{\vartheta_0-4}$	∞

Let us now discuss the case of the upward position of the slit. Very easily, the eqs. (4.9), (4.10) are proved to be still valid, being now

$$\frac{1}{k} = \frac{1}{v} + \frac{1}{v_0}\,.$$

The ranges (4.12) and (4.13) are in this case $0 \leqslant v < +\infty$ and $0 \leqslant k \leqslant v_0$. All the considerations made for the range (A) eq. (4.13) are then applicable to the present case and the expressions of the function $P(k,t)$ are, therefore, the same as those shown in table 1.

We should write, now, the analytical expressions of the transmission probability in terms of the velocity v of the neutron whose transmission probability is wanted. This is easily accomplished by substituting the quantity k in the expressions of $P(k,t)$ shown in table 1 with $1/v - 1/v_0$ in the case (i) of the downward position of the slit,

and

$$\vartheta_0 = \frac{v_0}{\gamma}\,.$$

The values of ϑ corresponding to the limits of the intervals for k are written in table 2.

The two cases (i) and (ii) will be discussed separately.

Case (i): The transmission probability is different from zero for

$$\frac{\vartheta_0}{1+\vartheta_0} \leqslant \vartheta \leqslant \frac{\vartheta_0}{1-\vartheta_0} \quad \text{when} \quad \vartheta_0 < 1\,,$$

(see figs. 5 and 6)

and for

$$\frac{\vartheta_0}{1+\vartheta_0} \leqslant \vartheta < \infty \quad \text{when} \quad \vartheta_0 \geqslant 1\,,$$

(see fig. 6).

There is a lower cut-off velocity, given by the equation

$$v = \frac{\vartheta_0}{1 + \vartheta_0}\gamma , \qquad (4.39)$$

which becomes equal to

$$\gamma = \frac{\omega R^2}{h} \qquad (4.40)$$

ities lower than γ without reducing the revolution speed ω [4]). The transmission probability can be unity for neutrons of velocity $v_0 = \vartheta_0\gamma$ provided they cross $x = 0$ for $t = 0$. This is an obvious result, considering the way in which the

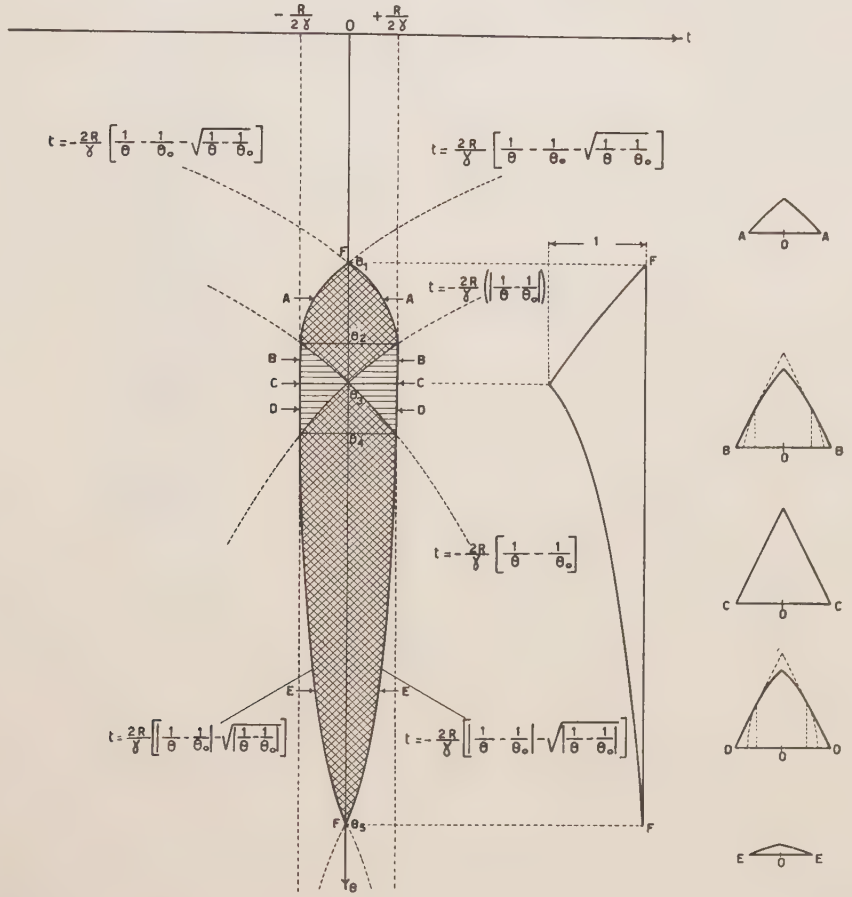

Fig. 5. Plot of the regions where, in case (i), the function $P(v,t)$ is defined and has the expressions:

$$P(v,t) = 1 - \frac{\omega|k|}{4h}\left(\frac{2R}{|k|} \mp t\right)^2 \qquad P(v,t) = 1 \pm \frac{2\gamma t}{R} .$$

All curves are calculated for $\vartheta_0 = \frac{1}{2}$. AA, BB, CC, DD, are cross sections of the function $P(v,t)$ with planes ϑ = const: FF is a section with plane $t = 0$. The numbers $\vartheta_1 \cdots \vartheta_5$ are equal to:

$$\vartheta_1 = \frac{\vartheta_0}{1 + \vartheta_0} , \quad \vartheta_2 = \frac{4\vartheta_0}{4 + \vartheta_0} , \quad \vartheta_3 = \vartheta_0 , \quad \vartheta_4 = \frac{4\vartheta_0}{4 - \vartheta_0} , \quad \vartheta_5 = \frac{\vartheta_0}{1 - \vartheta_0} .$$

for $\vartheta_0 = \infty$, that is, in the case of the straight slit. Since it is

$$\frac{\vartheta_0}{1 + \vartheta_0}\gamma < \gamma ,$$

it means that the use of a parabolic slit allows the performance of measurements with veloc-

[4]) V. V. Vladimirski *et al.*, P/641 Geneva Conf. (1955).

slit profile has been determined. For $v_0 = \infty$ the slit has a straight profile and the expressions of the function $P(v,t)$ reduce to those given by Mostovoi and Stone *et al.*[1,2]).

Case (ii): The highest value of k is $\vartheta_0\gamma$; it follows that if $0 \leqslant \vartheta_0 \leqslant 1$, the transmission

probability vanishes. For $\vartheta_0 > 1$ the transmission probability is different from zero when

$$\frac{\vartheta_0}{\vartheta_0 - 1} < \vartheta < \infty \,, \qquad \text{(see figs. 7 and 8).}$$

Hence, there is a lower cut-off velocity

$$v = \frac{\vartheta_0}{\vartheta_0 - 1}\gamma \tag{4.41}$$

which is larger than the cut-off velocity given by equation (4.39). It should be noted that the transmission probability never reaches unity, as may easily be seen analyzing the function $P(v,0)$.

In both cases (i) and (ii) the burst length is

$$\Delta t = \frac{R}{\gamma} \,. \tag{4.42}$$

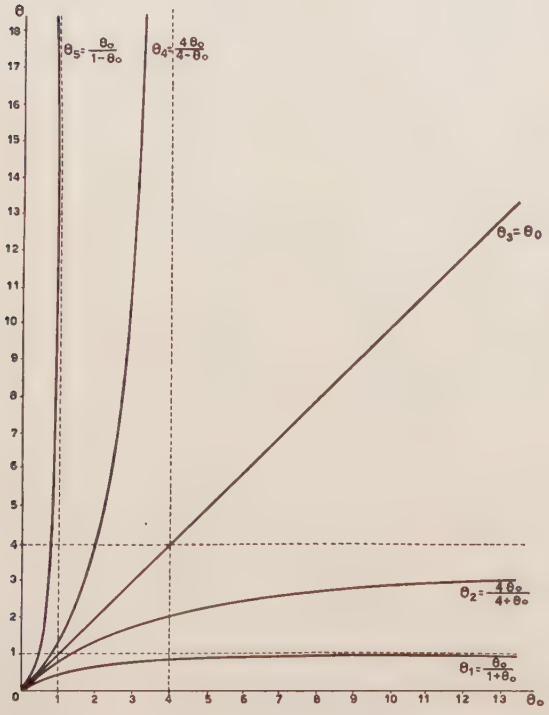

Fig. 6. Behaviour of the functions: $\vartheta_1(\vartheta_0) \cdots \vartheta_5(\vartheta_0)$.

5. The Burst Shape for an Incident Neutron Beam with a Velocity Spectrum $f(v)$

In the foregoing sections a general method has been described for determining the analytical expressions of the function $P(v,t)$ giving the probability, per unit time, for a neutron with velocity v to be transmitted by a revolving slit.

Let now the neutron velocity v be continuously varying over the range $0 \leqslant v < \infty$, according to a distribution function $f(v)$.

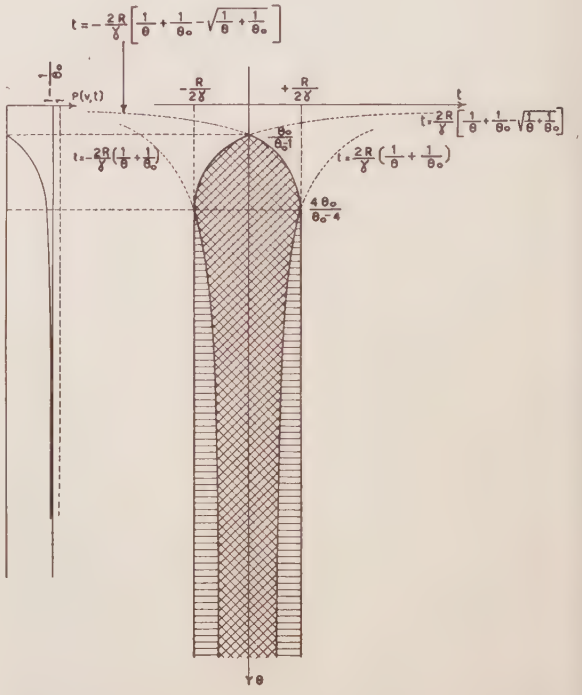

Fig. 7. Plot of the region where, in case (ii) the transmission probability is defined and has the following expressions:

$$P(v,t) = 1 - \frac{\omega}{4h}\,\frac{\gamma}{1/\vartheta + 1/\vartheta_0}\left\{\frac{2R}{\gamma}\,(1/\vartheta + 1/\vartheta_0) - t\right\}^{4}$$

$$P(v,t) = 1 - \frac{2\gamma t}{R} \,.$$

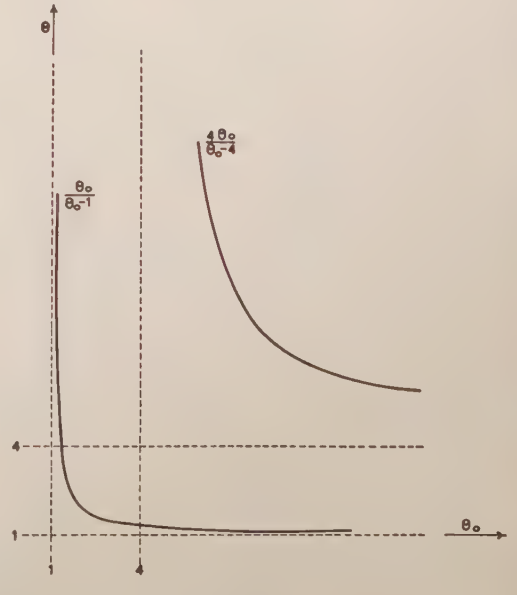

Fig. 8

The function $P(v,t)$ giving the burst shape in the case of monochromatic neutrons had a plot composed by a number of straight and curved lines in the plane $t,(Pv,t)$ (see, for example, fig. 5). In the case of neutrons with a velocity spectrum $f(v)$, the function $P(v,t)$ is represented by a continuous surface in the rectangular coordinate system v, t, $P(v,t)$. This surface is composed by a number of curved and plane surfaces, whose cross-sections with the planes $P(v,t) = 0$ and $v = \text{const}$ are shown in fig. 5. The dependence of the function $P(v,t)$ on the slit shape will be expressed by means of the quantity δ that summarizes the n quantities $\delta_1 \cdots \delta_n$ characterizing the slit shape (three, for example, in the case of a parabolic slit, i.e., $\delta_1 = w_0$, $\delta_2 = \omega$, $\delta_3 = h$). Therefore, the transmission probability will be represented by means of the expression $P(\delta,v,t)$.

It should be noted that the function $P(\delta,v,t)$ has a number of different analytical expressions in different intervals of the variable v, while the function $f(v)$ has only one analytical expression over the whole range $0 \leqslant v \leqslant \infty$.

According to the physical meaning of the functions $f(v)$ and $P(\delta,v,t)$, the product

$$\psi(\delta,v,t)\,\mathrm{d}v\,\mathrm{d}t = f(v)\,\mathrm{d}v\,P\,(\delta,v,t)\,\mathrm{d}t \qquad (5.1)$$

expresses the probability that a neutron having a velocity between v and $v + \mathrm{d}v$ and passing through the center of the revolving slit at an instant lying between t and $t + \mathrm{d}t$, is transmitted by the slit itself.

6. Distribution Shown by the Neutron with Velocity Spectrum $f(v)$, after a Flight Distance d

In order to describe the distribution shown by the neutrons with velocity spectrum $f(v)$ after a flight distance d, let us define the function $A(\delta,d,T)$, so as to give the number of neutrons reaching the plane $x = d$ at the time T.

First, we evaluate the probability eq. (5.1) for the time T. Since

$$T = t + d/v\,, \qquad (6.1)$$

where t is the instant at which the neutron with velocity v passes through $x = 0$ and T is the instant at which the same neutron reaches $x = d$, an easy calculation yields

$$\psi(\delta,v,T - d/v)\,\mathrm{d}v\,(T - d/v) = f(v)\,\mathrm{d}v\,P(\delta,v,T - d/v)\,\mathrm{d}T\,. \qquad (6.2)$$

The function $A(\delta,d,T)$ is then given by the equation

$$A(\delta,d,T)\,\mathrm{d}T = \mathrm{d}T \int_0^\infty \psi(\delta,v,T - d/v)\,\mathrm{d}v\,. \qquad (6.3)$$

Assuming that $t \ll T$ for any t of Δt, the equation (6.1) may be written as follows:

$$v = d/T\,; \qquad (6.4)$$

hence, the energy of the neutrons reaching $x = d$ at the time T can be evaluated.

The function $A(\delta,d,T)$ depends on δ, d and T. The quantity d can be a given distance or a function of δ, as will be seen later. Consequently, the function A is reduced to depend only on δ and T, i.e., $A(\delta,T)$. The value of the quantity δ must be chosen according to the experiment that has to be performed. For instance, if the distribution of the neutrons reaching the plane $x = d$ is wanted to exhibit a marked peak corresponding to a certain value v_{M} of the velocity, the function $A(\delta,T)$ must show a maximum for the value T_{M} derived from eq. (6.4) for $v = v_{\mathrm{M}}$. This is achieved by determining the quantity δ so as to satisfy the equation

$$\frac{\partial}{\partial \delta} A\,(\delta,T_{\mathrm{M}}) = 0\,.$$

Let us now determine the highest velocity $v_{\max}\,(\delta,d,T)$ and the lowest velocity $v_{\min}\,(\delta,d,T)$ of the neutrons reaching the plane $x = d$ at an instant T. These two velocities are easily determined by calculating the intersections of the curve of eq. (6.1) with the curves $t(v)$ which enclose the region where the transmission probability is not zero.

The larger the number

$$\frac{\mathrm{d}t}{\mathrm{d}v} = \frac{d}{v^2}\,, \qquad (6.5)$$

the smaller is the difference

$$v_{\max}\,(\delta,d,T) - v_{\min}\,(\delta,d,T) \qquad (6.6)$$

which gives the velocity spread.

From a physical point of view, this means

that the time interval Δt, giving the burst lenght, is very short as compared to the time T required by the neutron for travelling the distance d, so that all the neutrons of a burst may be considered to pass through $x = 0$ at the same time. Obviously, the number d/v^2 increases in proportion to the distance d. But this distance cannot have arbitrarily high values, since the superposition of the bursts must be avoided. This condition is fulfilled when d is not greater than an upper limit D which depends on the velocity $v_{\max}$ and $v_{\min}$ and is therefore a function of δ.

The best choice for d is then $d = D(\delta)$.

The number D is determined in the following manner. Let ν be the frequency of the bursts and $T_{\max}(\delta)$ ($T_{\min}(\delta)$) be the time required by the slowest (fastest) neutron to cover the distance d. The bursts do not superpose if

$$T_{\max}(\delta) \leqslant \frac{1}{\nu} + T_{\min}(\delta), \tag{6.7}$$

that is

$$\frac{d}{v_{\min}(\delta)} \leqslant \frac{1}{\nu} + \frac{d}{v_{\max}(\delta)}, \tag{6.8}$$

and

$$d \leqslant \frac{1}{\nu} \frac{1}{\dfrac{1}{v_{\min}(\delta)} - \dfrac{1}{v_{\max}(\delta)}}.$$

Consequently,

$$D(\delta) = \frac{1}{\nu}\left[\frac{1}{v_{\min}(\delta)} - \frac{1}{v_{\max}(\delta)}\right]^{-1}. \tag{6.9}$$

For example, in the case of the parabolic slit for $0 \leqslant \vartheta_0 \leqslant 1$, we have

$$\nu = \frac{\omega}{2\pi}; \qquad v_{\min}(\vartheta_0) = \frac{\gamma\vartheta_0}{2+\vartheta_0}, \qquad v_{\max}(\vartheta_0) = \frac{\gamma\vartheta_0}{1-\vartheta_0}$$

so that

$$D(R,h) = \frac{\pi}{\omega}\gamma = \frac{\pi R^2}{h}. \tag{6.10}$$

In the case of the straight slit we have

$$\nu = \frac{\omega}{\pi}, \qquad v_{\min} = \gamma, \qquad v_{\max} = \infty$$

so that

$$D(R,h) = \frac{\pi}{\omega}\gamma = \frac{\pi R^2}{h}. \tag{6.11}$$

The value (6.10) which coincides with the value (6.11) has been given also by Mostovoi *et al.*

The writers wish to thank Prof. Ezio Clementel for stimulating discussions on the subject of this work.

NUCLEAR INSTRUMENTS AND METHODS 4 (1959) 151–163; NORTH-HOLLAND PUBLISHING CO.

A SCINTILLATION COUNTER WITH NEUTRON AND GAMMA-RAY DISCRIMINATORS

F. D. BROOKS

U.K.A.E.A. *Research Group, Harwell, Didcot, Berks.*

Received 16 February 1959

Certain organic scintillators, notably anthracene, stilbene and quaterphenyl crystals and oxygen-free liquid scintillators, show an effectively longer scintillation decay time for heavily ionizing particles such as alpha-particles or protons than for electrons. A scintillation counter is described which distinguishes fast neutrons from gamma-rays by means of the different decay times of recoil proton and Compton electron scintillations respectively. Measurements of the proton-electron resolution for different scintillators are described. It is found, for example, that using a one inch thick stilbene crystal, 2 MeV neutrons may be detected with 9.5% efficiency while the detection efficiency for 2 MeV gamma-rays is reduced by decay time discrimination to less than 0.007%. An application of the counter for fission cross section measurements by fission neutron detection is described. The decay time properties of the scintillators are discussed and the longer decay time for protons (or alpha-particles) is interpreted in terms of slow (10^{-7} sec) ion recombination processes in the scintillators; these processes produce a slow component in the scintillation decay and in a proton scintillation the proportion of slow component is more than in an electron scintillation[4]).

1. Introduction

In a scintillation detector the mode of decay and the decay time of the light emission from the scintillator may sometimes be of particular interest; for example when the timing resolution of the instrument is estimated or when the physical processes in the scintillator are the subject of study. These characteristics have recently achieved new prominence following the report by Wright[1]) that scintillations produced by alpha-particles and electrons in anthracene crystals showed decay times of 53 mμsec and 31 mμsec respectively. It was subsequently reported[2]) that other organic scintillators, notably stilbene and quaterphenyl crystals and some liquid scintillators, showed decay time properties similar to those observed in anthracene; although the scintillation decay itself was not studied in detail it was found that the decay times of these scintillators were effectively longer for heavily ionizing particles, such as alpha-particles or protons than for electrons.

This effect has since become the basis of a new type of scintillation counter[2,3,4]) which discriminates promptly and efficiently between protons (or alpha-particles) and electrons and is thus particularly useful for detecting fast neutrons in the presence of gamma-rays. The present paper describes such a counter and its application to nuclear physics experiments. Studies of various scintillators with respect to their suitability for use in the counter are also described and the physical processes responsible for the decay time differences are discussed.

2. Description of the Counter

To achieve a simple practical instrument a photomultiplier circuit is used which delivers an output pulse whose amplitude, h, depends on the *decay time* of the scintillation. The circuit may be adjusted to give zero, or very small, h for one particular decay time, e.g. that for gamma-ray scintillations; in this condition neutron (i.e. recoil proton) scintillations, having a different decay time, each produce a pulse of large h and may be selected by an amplitude discriminator.

[1]) G. T. Wright, Proc. Phys. Soc. B **49** (1956) 358.

[2]) F. D. Brooks, Progress in Nuclear Physics, Ed. O. R. Frisch **5** (Pergamon, London, 1956) 284; Liquid Scintillation Counting, (Pergamon London, 1958), p. 268.

[3]) M. Forte, International Conference on the Peaceful Uses of Atomic Energy, A/CONF. 15/P/1514, Geneva (1958)

[4]) R. B. Owen, I. R. E. Transactions on Nuclear Science, NS-5, No. 3 (1958) 198.

Fig. 1 shows the photomultiplier circuit. When the photomultiplier detects a scintillation, positive pulses are generated at its dynodes due to the electrons they lose in the multiplication process. The output circuit in fig. 1 uses both the positive pulse from the last dynode and the

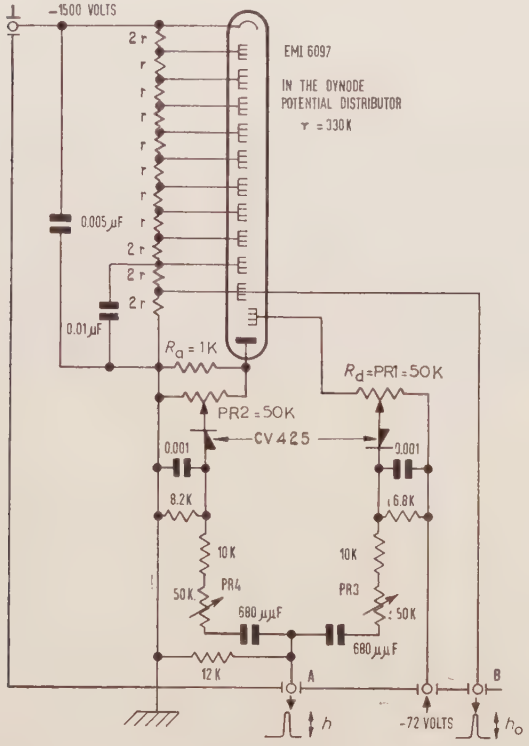

Fig. 1. Photomultiplier circuit.

negative pulse from the multiplier collector, or anode. To describe the circuit operation consider that the effective load at either electrode consists of a capacity, C, in parallel with a resistance, R. Then considering a scintillation which is a step rise followed by an exponential decay, of decay time, T, and assuming that the photomultiplier current pulse is of this same form, it can be shown that the charge, Q, on the electrode at a time, t, after charge begins to arrive at the electrode is given by:

$$Q = \frac{Q_0 \cdot RC}{T - RC} [\exp(-t/T) - \exp(-t/RC)] \quad (1)$$

where Q_0 is the net total charge which flows to the electrode during the whole scintillation. Differentiating (1) with respect to t we obtain that Q is maximum at a time, t_m, where:

$$t_m = \frac{T \cdot RC}{T - RC} \log_e \left(\frac{T}{RC} \right) \quad (2)$$

and hence that the amplitude, V, of the voltage pulse developed across R is:

$$V = \frac{V_0 \cdot RC}{T - RC} \left\{ \exp\left(\frac{RC \log_e (T/RC)}{RC - T} \right) - \exp\left(\frac{T \log_e (T/RC)}{RC - T} \right) \right\} \quad (3)$$

where $V_0 (= Q_0/C)$ is the amplitude obtained when $RC >> T$. Fig. 2 shows V/V_0 versus T/RC as given by eq. (3).

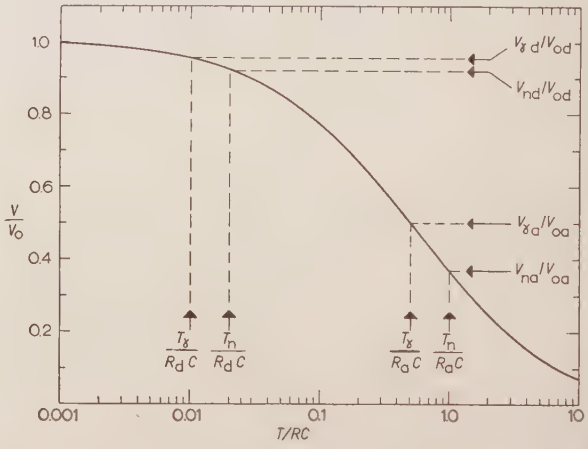

Fig. 2. V/V_0 as a function of T/RC from eq. (3). T = scintillation decay time; RC = dynode (or anode) time constant; V = amplitude of the pulse produced at the dynode (or anode); V_0 = pulse amplitude for $RC \gg T$.

In the photomultiplier circuit (fig. 1) different resistive loads, R, are used at the dynode and the anode respectively; at the dynode, $R_d = 50\ k\Omega$ and at the anode $R_a = 1\ k\Omega$. The stray capacity, C, is about the same at both electrodes hence the time constant R_dC at the dynode is about 50 times R_aC, that at the anode. Now suppose R_d is chosen so that $T_\gamma/R_dC = 0.01$, where T_γ is the decay time of a gamma-ray scintillation. Then $T_\gamma/R_aC = 0.50$ and from fig. 2 the amplitudes of the pulses which a gamma-ray scintillation produces at the dynode and anode respectively are, $V_{\gamma d} = 0.96\ V_{od}$ and $V_{\gamma a} = 0.50\, V_{oa}$; where V_{od} and V_{oa} are the

amplitudes which would be obtained at the dynode and anode respectively if R_dC and R_aC were much greater than T_γ. Assuming that the gain, k, between the last dynode and the anode is constant, we may write:

$$V_{oa} = kV_{od} . \quad (4)$$

The shapes and times of maxima of the dynode and anode pulses are different according to eqs. (1) and (2) respectively. However each pulse is stretched by a circuit consisting of a crystal diode and condenser (0.001 μF) so that two pulses of similar shape but opposite polarity are fed to the output terminal, A, of the counter (fig. 1). Ideally the amplitudes of these components are respectively $\phi_dV_{\gamma d}$ and $\phi_aV_{\gamma a}$, where ϕ_d is the constant fraction by which the positive pulse amplitude is reduced between the dynode and A and ϕ_a is that by which the negative pulse amplitude is reduced between the anode and A. The amplitude, h, of the resultant pulse at A is:

$$h = \phi_dV_d - \phi_aV_a . \quad (5)$$

Thus for a gamma-ray scintillation,

$$\begin{aligned} h_\gamma &= \phi_dV_{\gamma d} - \phi_aV_{\gamma a} \\ &= \phi_d\,[0.96 - 0.50\,(k\phi_a/\phi_d)]\,V_{od} . \end{aligned} \quad (6)$$

Now ϕ_d is controlled by the potentiometers PR1 and PR3 in fig. 1 and ϕ_a is controlled by PR2 and PR4. We may adjust these potentiometers to make $k\phi_a/\phi_d = 1.92$ thereby making h_γ always zero, irrespective of the value of V_{od}, or the total light in the scintillation. In other words the circuit may be "balanced" to give zero pulse height output at A for all gamma-ray scintillations.

Now consider the response of the balanced circuit to a neutron scintillation of decay time, T_n, where for example, $T_n = 2T_\gamma$. As before we obtain from fig. 2 that $V_{nd} = 0.92\ V_{od}$ and that $V_{na} = 0.37\ kV_{od}$. Thus for a neutron the resultant pulse amplitude, h_n, at A is:

$$\begin{aligned} h_n &= \phi_d\,(0.92 - 1.92 \times 0.37)\,V_{od} \\ &= 0.21\ \phi_dV_{od} . \end{aligned} \quad (7)$$

That is for a neutron a positive output pulse is obtained of amplitude proportional to V_{od} and hence to the total light in the scintillation. This is true in general provided T_n is greater than T_γ.

In practice the circuit behaviour is not exactly, but only qualitatively described by the above analysis, for a number of reasons. Firstly, it is an approximation to describe the scintillation decay as a single exponential (refs.[1,4–7]); this is not true in general for the organic scintillators. Secondly, the photomultiplier current pulse shape will generally vary from the scintillation pulse shape[1]) due to statistical effects, transit time spread and space charge saturation in the multiplier. Thirdly, because space charge saturation may occur between the last dynode and the anode, k is not as assumed in eq. (4), constant but depends on V_{od}. Fourthly, ϕ_d and ϕ_a also depend on V_{od} because the two diodes in the output circuit are characteristically non-linear impedances. However the non-linear effects from the two diodes may be made to cancel one-another out to some extent by selecting a pair with similar resistance-voltage characteristics and adjusting PR1 or PR2 to equalise the pulse amplitudes fed to them. Furthermore, remaining diode non-linearity may be part compensated for by the space charge saturation effect, for whereas ϕ_d and ϕ_a increase as V_{od} increases, k decreases. A dynode voltage distribution may be obtained for which the variation of k compensates that of ϕ_a/ϕ_d so that the product $k\phi_a/\phi_d$ remains constant. The circuit may thus be balanced in terms of eq. (6) over a wide range of V_{od}.

The counter is adjusted to balance with the aid of a cathode ray tube display, obtained as indicated in fig. 3. For this display, an additional output pulse of amplitude, h_0, is obtained from the second last dynode of the photomultiplier, via B in fig. 1. The load time constant at this dynode is long compared with T_γ or T_n hence h_0 is proportional to the total light in the scintillation or to V_{od} in eqs. (6) and (7). The two coincident output pulses from A and B in fig. 1

[5]) H. B. Phillips and R. K. Swank, Rev. Sci. Instr. **24** (1953) 611; R. K. Swank and W. L. Buck, Rev. Sci. Instr. **26** (1955) 15.

[6]) H. Kallmann and G. J. Brucker, Phys. Rev. **108** (1957) 1122.

[7]) F. B. Harrison, Nucleonics **12**, No. 3 (1954) 24; Phys. Rev. **89** (1953) 322.

are amplified and stretched[8]) to obtain two flat-topped and almost square pulses of amplitudes proportional to h and h_0 respectively. These pulses are applied to the Y and X plates of the C.R.T. respectively and the C.R.T. trace is brightened only while such a pair of pulses are

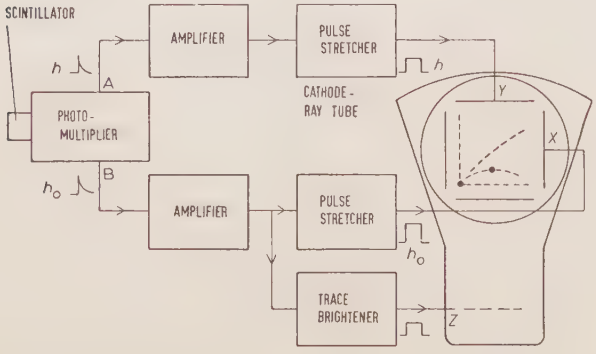

Fig. 3. Block diagram of the apparatus used to obtain a C.R.T. display of h, the pulse amplitude which depends on scintillation decay time, versus h_0, the pulse amplitude proportional to the total light in the scintillation.

applied to its plates. Thus a point (h_0,h) is plotted on the C.R.T. screen for each scintillation. Using a gamma-ray source which gives a continuous distribution of pulse heights, h_0, eq. (6) is thus plotted on the C.R.T. screen; the counter is then balanced by adjusting the potentiometers PR1–PR4 (fig. 1), the voltage applied to the dynode potential distributor and the potential applied to the last dynode until the h versus h_0 locus falls parallel to and as close to the X-axis of the display as possible (see fig. 4(a)).

3. Results for Different Scintillators and Photomultipliers

Fig. 4 shows distributions of h, the pulse height which depends on scintillation decay time, versus h_0 the pulse height proportional to the total light in the scintillation, recorded by photographing the C.R.T. Display. An EMI 6097 photomultiplier was used (as in fig. 1) together with a 1 in.^{3} stilbene crystal and; (a) a Co^{60} source (1.3 MeV gamma-rays); (b) a Po^{210}-Be source ($\lesssim$ 12 MeV neutrons and 4.5 MeV gamma-rays); (c) the Co^{60} source and an Am^{241} source (which emits 5.5 MeV alpha-particles); (d) the Po^{210}-Be source and the Am^{241} source. With the Co^{60} source Compton electrons ejected inside the crystal give a Compton distribution in h_0 and produce a single continuous locus in the h versus h_0 distribution (fig. 4(a)); h is small though not zero over the whole range of h_0. With the Po^{210}-Be source (fig. 4(b)) two diverging loci are obtained, one similar to that in (a) and due to gamma-rays and the other due to recoil protons from neutron-proton collisions inside the crystal. Along the neutron locus h increases with h_0, though not linearly as predicted for the ideal case represented by eq. (7). In fig. 4(b) the two loci are well resolved above the pulse height, $\bar{h}_0$, which corresponds to 0.5 MeV recoil proton energy and 0.13 MeV electron energy respectively. Clearly too, one may select protons above this energy and reject all electron scintillations by amplitude discriminating the h pulses at the level, δ, indicated in fig. 4(b). Fig. 4(c) shows the monenergetic alpha-particle group from Am^{241} well separated from the Co^{60} gamma-ray locus; here it is clear that alpha-particle scintillations can be efficiently and unambiguously distinguished from gamma-ray scintillations by amplitude discriminating the h pulses at a level δ. Fig. 4(d) on the other hand shows that the Am^{241} alpha-particles are not well separated from the Po^{210}-Be neutron locus.

In practical applications the equipment required for selecting neutrons or alpha-particles and rejecting gamma-rays is just the photomultiplier and scintillator, one amplifier, amplifying the h pulse, and an amplitude discriminator. The C.R.T. display and associated equipment shown in fig. 3 are not required after the counter has been balanced. The C.R.T. display system has also been used extensively to compare photomultipliers and scintillators since it offers a quick and convenient, though qualitative, means of observing and recording h versus h_0 loci. Several C.R.T. displays have been photographed to determine what loci are obtained using different photomultipliers and scintillators.

[8]) W. Bernstein, R. L. Chase and A. W. Schardt, Rev. Sci. Instr. **24** (1953) 437.

The photomultipliers tested include the types RCA 5819 and 6810, Du Mont 6292, and EMI 6260, 6097, 6099 and 9530. Using neutron and gamma-ray sources and a stilbene crystal all tubes gave loci similar to those in fig. 4; that is no particular type appeared to be superior for this application. The same was true when a liquid scintillator was used. This result is interesting because the transit time spreads claimed for the selection of multipliers range from 2 to 20 mμsec and are thus comparable with the decay times generally quoted[5,6]) for stilbene and liquid scintillators, which are both less than 10 mμsec. However, scintillations from these scintillators actually contain a proportion ($\lesssim$20%) of slow components[4,7]) of decay times $\gtrsim$100 mμsec in addition to the more familiar fast component of decay time < 10 mμsec. Owen[4]) has shown that it is these slow components which are responsible for the effective difference in decay time for protons and electrons; a proton scintillation contains more slow component emission and less fast component emission than an electron scintillation. Since the transit time spreads of all the multipliers are much less than the slow component decay times, all are equally capable of resolving the difference between proton and electron scintillations.

Loci were also photographed using anthracene, quaterphenyl and diphenylacetylene crystals respectively. Anthracene and quaterphenyl gave resolved proton and electron loci very similar to those shown for stilbene in fig. 4. Diphenylacetylene crystals did not resolve proton and electron loci however and thus do not appear to show different decay times for protons and electrons. Loci were also observed for 1 cm^3 anthracene and stilbene cyrstals at different temperatures, ranging from + 25° C to — 70° C and no change in the loci with crystal temperature was found for either crystal.

It was found that liquid scintillators do not in general resolve proton and electron loci unless dissolved oxygen has previously been removed from them; e.g. by flushing with dry nitrogen to displace the dissolved oxygen or by removing all

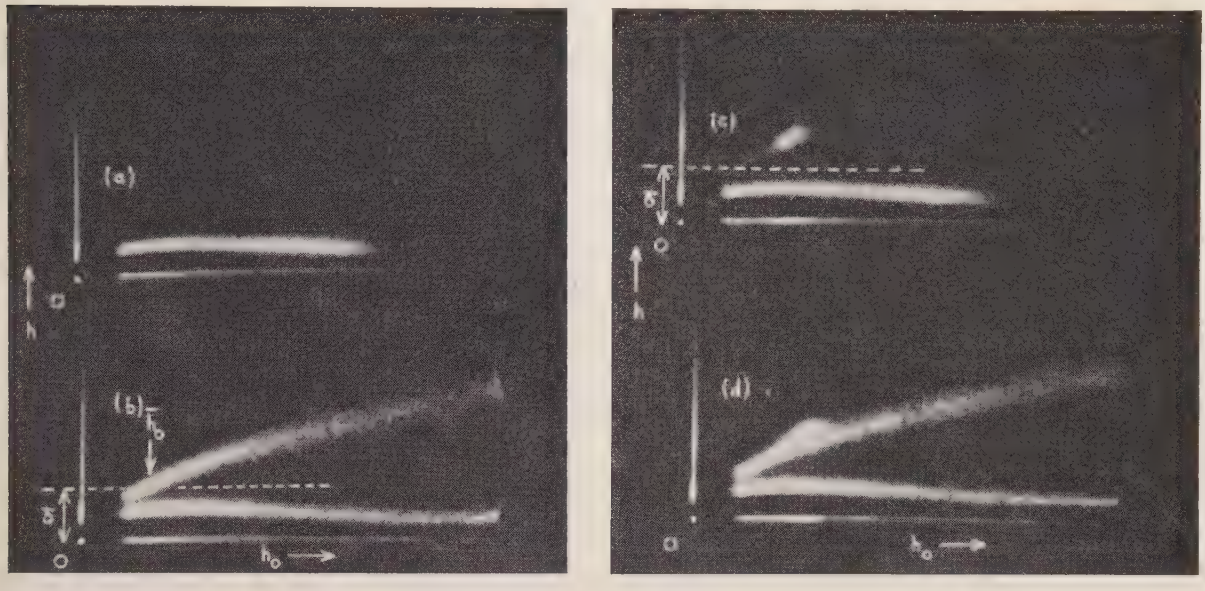

Fig. 4. Distributions of the pulse amplitude h, (which depends on scintillation decay time), versus the pulse amplitude h_0 (proportional to total light in the scintillation), for stilbene and; (a) Co^{60} source (1.3 MeV gamma-rays); (b) Po^{210}-Be source ($\lesssim$ 12 MeV neutrons + 4.5 MeV gamma rays); (c) Co^{60} source + Am^{241} source (5.5 MeV alpha-particles); (d) Po^{210}-Be source + Am^{241} source.

gases dissolved in the liquid by freezing followed by evacuation. Some oxygen-free solutions resolve proton and electron loci almost as well as stilbene, for example;

(i) [9])4 g/litre p-terphenyl (or PPO or PBD) in toluene (or xylene).

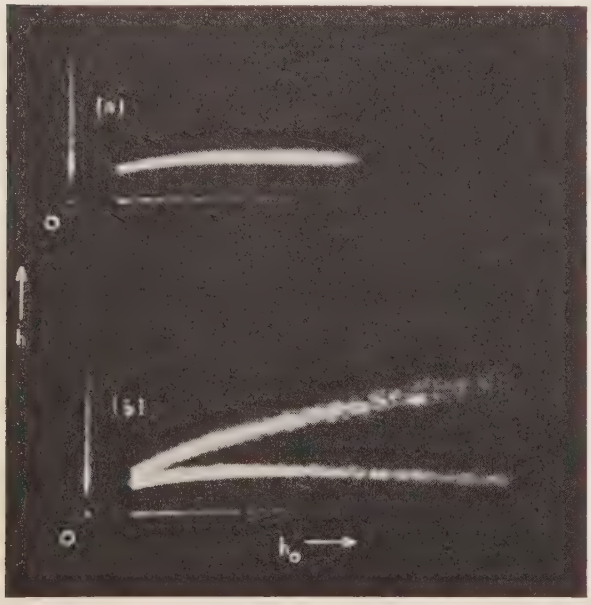

Fig. 5. Distributions of h versus h_0 for an oxygen-free liquid scintillator (4 g/litre PPO + 0.1 g/litre POPOP in toluene) and; (a) Co^{60} source; (b) Po^{210}-Be source.

(ii) [9])4 g/litre p-terphenyl (or PPO or PBD) + 0.1 g/litre POPOP in toluene or xylene.

(iii) [9])4 g/litre PPO (or PBD) + 0.1 g/litre POPOP in trimethyl-borate (47%) + xylene (31%) + naphthalene (22%).

Fig. 5 shows the loci obtained using the Po^{210}-Be source, solution (ii) from above and an EMI 6097 photomultiplier. The loci are well resolved and, as in fig. 4, protons of energy $\gtrsim 0.6$ MeV may be selected by amplitude discrimination at a suitable level of h. Loci were also photographed for solutions of different PPO concentration (from 0.05 to 8.0 g/litre) in toluene + 0.1 g/litre POPOP. Apart from the known variation[10]) of light output (and hence h_0) with PPO concentration, no variation of the loci was observed.

A number of plastic scintillators based on polystyrene or polyvinyl-toluene with p-terphenyl, PPO, TPB[9]) etc. as solutes were tested but none of these resolved proton and electron loci. Fig. 6 shows the loci obtained using Nuclear Enterprises' plastic scintillator, NE 102, and; (a) the Co^{60} source; (b) the Po^{210}-Be source. The proton locus is displaced from the electron

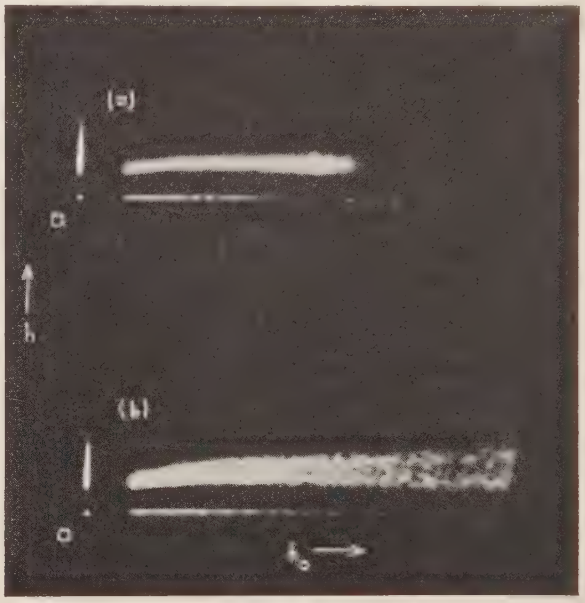

Fig. 6. Distributions of h versus h_0 for Nuclear Enterprises' plastic scintillator, NE 102, and; (a) Co^{60} source; (b) Po^{210}-Be source.

locus but the two loci are not resolved. This result is typical of the behaviour found in the plastic scintillators which thus appear to be a class which do not show marked decay time variations and are thus not ideal for neutron-gamma-ray discrimination by the present method.

4. Quantitative Measurements of Proton-Electron Resolution

The proton-electron resolution of the counter was quantitatively determined using a single-channel analyser and a 100-channel analyser as follows. The single-channel analyser selected events where h_0 lay within a small fixed range.

[9]) Scintillator Nomenclature "Shorthand"; PPO = 2,5 diphenyloxazole; PBD = 2-phenyl-5-(4 biphenylyl)-1,3,4-oxadiazole; POPOP = 1,4-bis2-(5-phenyloxazolyl)-benzene; TPB = 1,1,4,4,-tetraphenyl-1,3-butadiene.

[10]) F. N. Hayes, Ott, Kerr and Rogers, Nucleonics **13**, No. 12 (1955) 38.

The h pulses corresponding to these events were fed via a gate, opened by the single-channel analyser, to the 100-channel analyser which then gave their pulse height distribution. The pulse height distribution obtained is thus equivalent to the pulse density as a function of ordinate

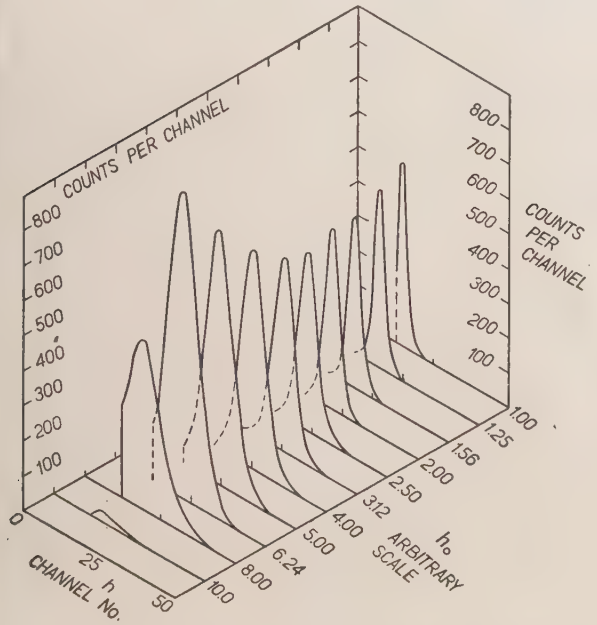

Fig. 7. A series of pulse height distributions obtained using stilbene and a Co^{60} source. Each component distribution shows the number of scintillations recorded per channel per ten minutes as a function of h for a particular value of h_0.

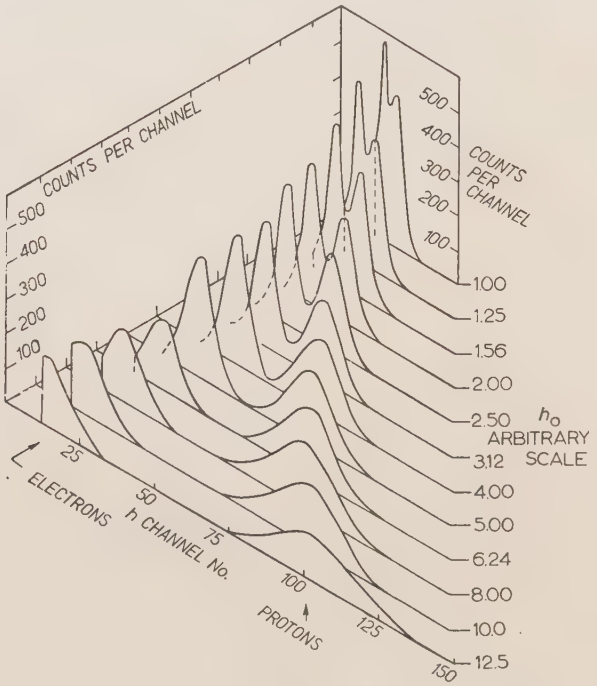

Fig. 8. A series of pulse height distributions obtained as for fig. 7 but using stilbene and a Po^{210}-Be source.

along a particular abcissa in figs. 4, 5 or 6. A series of such measurements gives a complete three-dimensional picture of the loci, of pulse density versus h versus h_0.

Figs. 7 and 8 show two series of pulse height distributions obtained using a stilbene crystal and an EMI 6097 photomultiplier; fig. 7 with the Co^{60} source and fig. 8 with the Po^{210}-Be source. A channel width 0.1 × the mean pulse height of the channel was used in the single-channel analyser.

For each component run (i.e. value of h_0) in fig. 8 the proton-electron resolution may be defined, arbitrarily, as the ratio, R, of the distance between the (mean pulse heights of the) proton and electron groups to the full width at half-maximum of the electron group. R has been evaluated as a function of h_0 from figs. 7 and 8 and is plotted in fig. 9. The scale of h_0 was calibrated in terms of electron energy from the Compton edge observed for Co^{60} 1.3 MeV gamma-rays (fig. 7). The scale of proton energy also shown in fig. 9 is based on the known relative response of stilbene to protons and electrons[11]).

Additional measurements of R were made for other scintillators, namely anthracene and quaterphenyl crystals and a solution of 4 g/litre PPO + 0.1 g/litre POPOP in toluene. The data obtained are included in fig. 9. If we adopt the criterion that R must exceed unity for effective resolution, then, from fig. 9 we see that the three crystals resolve above a proton energy of 0.5 MeV (and electron energy of 0.13 MeV) while the liquid scintillator resolves above proton and electron energies of 0.6 MeV and 0.16 MeV respectively.

[11]) Taylor, Jentschke, Remley, Eby and Kruger, Phys. Rev. 84 (1951) 1034.

The data shown in figs. 7 and 8 may also be used to determine how efficiently one selects proton scintillations and rejects electron scintillations in the practical system suggested in section 2; that is where the h pulses are fed to an amplitude discriminator biassed to a suitable level δ (see fig. 4). For a given δ we may determine, for each component run (h_0) in figs. 7 and 8, what fraction (of area) of the proton group and what fraction of the electron group lie in the region $h > \delta$; this gives the proton and electron counting efficiencies for a discriminator bias, δ, and the respective proton and electron energies corresponding to the h_0 of the component. Counting efficiencies have been determined for a series of values of δ and for each component run in figs. 7 and 8. Fig. 10 shows the proton counting efficiency versus proton energy for different δ; fig. 11 shows that for electrons.

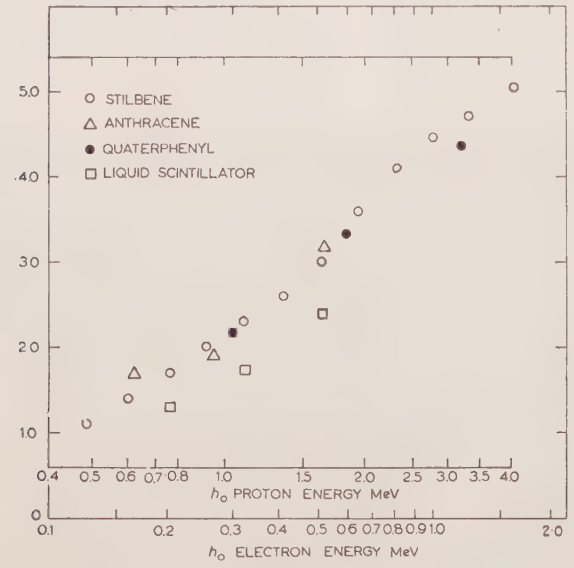

Fig. 9. Proton-electron resolution, R, as a function of proton and electron energy for stilbene (open circles), anthracene (triangles), quaterphenyl (solid circles) and an oxygen-free liquid scintillator of 4 g/litre PPO + 0.1 g/litre POPOP in toluene (squares).

With the aid of neutron-proton scattering cross section data[12]) and Compton cross section data[13]) it is now a simple step to calculate the absolute efficiency of the counter for neutrons and gamma-rays respectively. Suppose, for example, we have a 1 inch thick stilbene crystal and wish to count 2 MeV neutrons in a background of 2 MeV gamma-rays. 27% of the neutrons make n–p collisions in the crystal and the energies of the recoil protons produced are distributed evenly between 0 and 2 MeV.

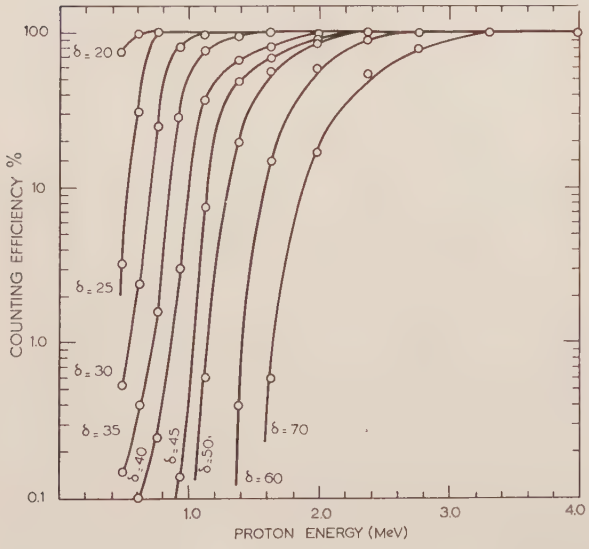

Fig. 10. Percentage of proton scintillations counted as a function of proton energy for different discriminator bias settings, δ.

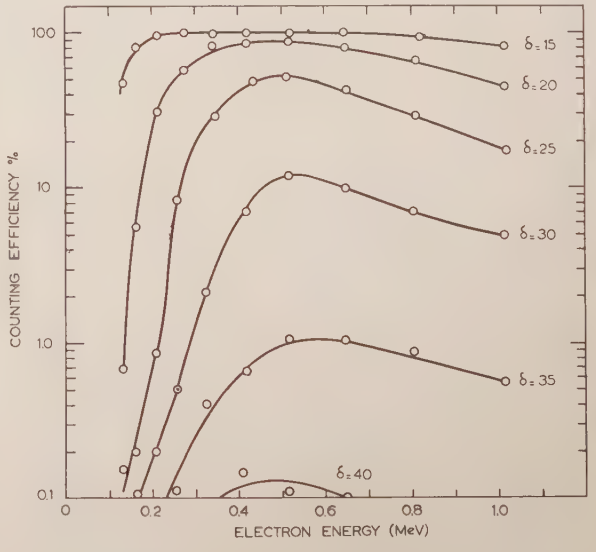

Fig. 11. Percentage of electron scintillations counted as a function of electron energy for different discriminator bias settings, δ.

[12]) D. J. Hughes and R. B. Schwartz, BNL 325 (1957).
[13]) W. Heitler, The Quantum Theory of Radiation (Oxford, 1949), Ch. 3.

Suppose we choose $\delta = 40$, then by integrating the appropriate curve in fig. 10 from 0 to 2 MeV we obtain that the fraction of the recoil proton distribution counted is 0.35; thus the absolute neutron counting efficiency is $0.35 \times 27 = 9.5\%$. Similarly, 14% of the gamma-rays are Compton scattered in the crystal producing recoil electrons with a Compton energy distribution from 0 to 1.8 MeV. From the curve for $\delta = 40$ in fig. 11 we obtain that a fraction, 0.0005, or less, of this Compton distribution is counted; thus the absolute gamma-ray counting efficiency is less than 0.0005×14 i.e. less than 0.007%.

5. Timing Resolution and Dead Time

The output pulse, h, from the counter is necessarily relatively "slow" (≈ 5 μsec wide) due to the long integrating times used in the output circuit (fig. 1). Thus the counter has an effective dead time of about 5 μsec, or at count rates exceeding about 10^4 (neutrons + gamma-rays) per second, neutron counts will be lost. The timing resolution of the counter is not limited by the slow rise time (≈ 0.5 μsec) of the h pulse however. For fast timing or coincidence applications an independent "fast" output pulse is derived from one of the photomultiplier dynodes, as the h_0 pulse is derived via B in fig. 1. This pulse is then delayed and gated by the discriminator triggered by the h pulse. In this system the timing resolution depends only on the photomultiplier transit time spread and the scintillator decay time and can be 5 mμsec or less for stilbene or liquid scintillators.

6. An Application of the Counter

This type of scintillation counter obviously has many possible applications for discrimination between alpha-particles, protons and electrons. A typical application for fission neutron detection will be described as an example.

To determine the fission cross section of uranium-235 for 6 eV to 60 eV neutrons two experiments were carried out as follows, using 3.1 inch diameter discs of U^{235} of 0.425 g/cm^2 and 90 g/cm^2 respectively. In each experiment the disc, or sample, was placed in a neutron beam produced by the Harwell 15 MeV linear electron accelerator, 10 metres from the accelerator target or pulsed neutron source. The stilbene crystal of the counter was placed close to the sample but outside the incident neutron beam. A fraction of the incident neutrons produced U^{235} fission in the sample and a fraction of the fission neutrons emitted were detected in the crystal. Using a neutron discriminator setting corresponding to $\delta = 40$ in fig. 10, the counter was adjusted to respond only to neutrons of energy greater than 1 MeV. Thus, as shown by the curve for $\delta = 40$ in fig. 11, at least 99.9% of any gamma-rays detected by the crystal (e.g. from radiative capture in the sample) were discarded by the discriminator. Counts from the discriminator were fed to a 100-channel time-sorter to be time analysed with respect to the accelerator neutron pulse. The duration of the neutron pulse at the accelerator target was less than 0.5 μsec and the width of each timing channel was 1.0 μsec. The fission neutron yield per timing channel, y, was thus determined as a function of incident neutron time-of-flight (from target to sample) that is as a function of incident neutron energy. This was done for the same total number of incident neutrons for the thick and thin samples respectively.

Now for U^{235} the number of neutrons emitted per fission and the fission neutron energy spectrum do not vary significantly with incident neutron energy from 6 eV to 60 eV[14]). We may thus assume that the measured fission neutron yield, y, is proportional to the number of fissions in the sample or, in other words, that the fission detection efficiency of the counter, ϵ, is constant over this incident neutron energy range. Now suppose we have N neutrons incident on the sample during the total time that a particular timing channel is open in the experiment and that only a small fraction ($< 2\%$) of these neutrons are scattered or stopped in the sample. Then the fission cross section, σ_f, averaged over the incident neutron energy range defined by

[14]) L. M. Bollinger, Conference on Neutron Physics by Time of Flight, Gatlinburg, ORNL 2309 (1956) p. 167.

the channel, is given, to better than 1%, by

$$\sigma_f = y/N\epsilon nx \qquad (8)$$

where n is the number of U^{235} nuclei per unit volume in the sample and x is the sample thickness.

In order to evaluate σ_f from eq. (8) values of $N\epsilon$ were determined as follows. From published cross section data[12]) it was known that the thick sample was black to (i.e. transmitted less than 1% of) 8.9 eV neutrons due to the U^{235} resonance at this energy and furthermore that the ratio of total width to fission width Γ/Γ_f for this U^{235} level was 1.60. Thus in the thick sample experiment, for the timing channel corresponding to 8.9 eV, $N\epsilon = 1.60\ y$. The (energy) spectrum of the incident neutrons was known and hence the variation of N with channel number. Values of $N\epsilon$ applying to the other timing channels in the thick sample experiment were thus calculated using the value for the 8.9 eV channel as a calibration.

Now for any particular timing channel N was the same in the thick and thin sample experiments since the samples were discs of equal area and were placed in identical positions and irradiated by the same total number of neutrons in the respective experiments. However ϵ is not necessarily the same in the two experiments, because a smaller fraction of the fission neutrons produced in the thick sample escape directly to the detector; some neutrons are elastically or inelastically scattered, or captured, in the sample, tending to decrease ϵ; others produce secondary fissions and hence more fission neutrons, tending effectively to increase ϵ. Calculation showed that these effects cancelled one another to within $\pm$ 1% or, in other words, that ϵ was the same, within this accuracy, in the two experiments. Values of $N\epsilon$ obtained for the thick sample were thus assumed to be true also for the thin sample experiment.

Fission cross section data were finally evaluated

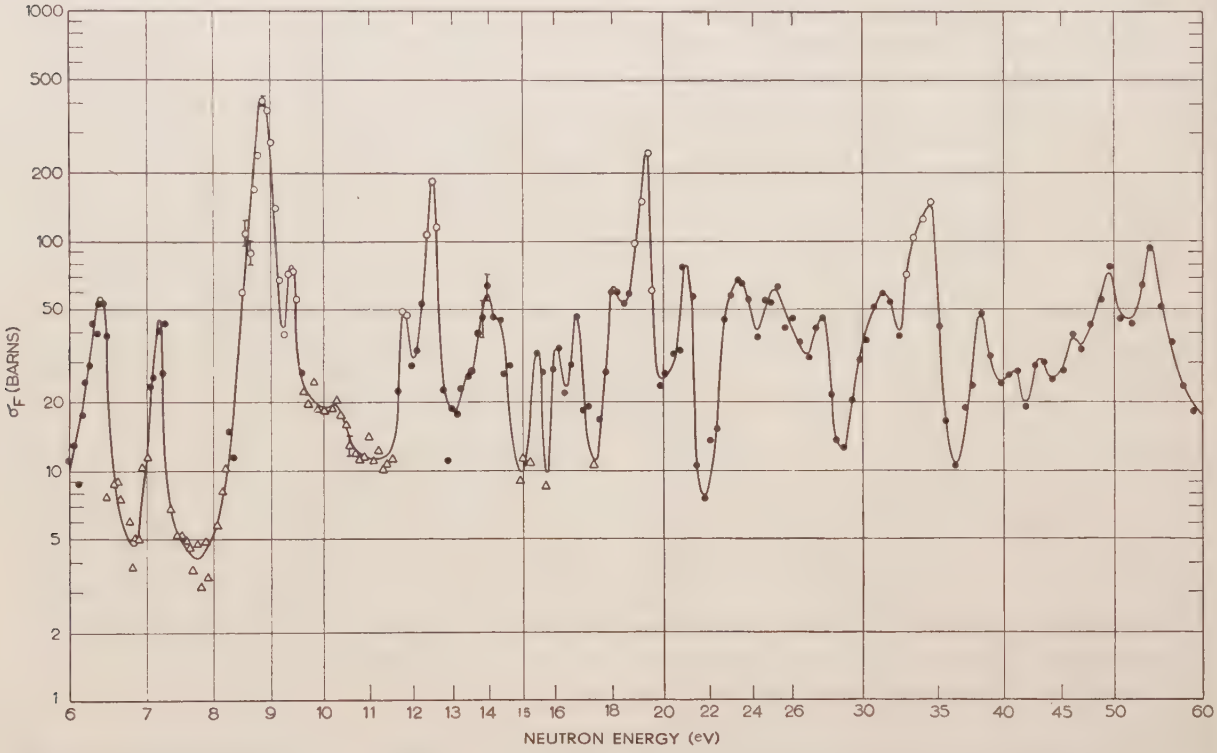

Fig. 12. Fission cross section, σ_F, of U^{235} for 6 eV to 60 eV neutrons; solid circles represent data from the thin sample experiment evaluated from eq. (8); triangles represent thick sample data evaluated from eq. (8); open circles represent thin sample data corrected for the thickness of the sample.

from equation (8) and are plotted in fig. 12; solid points and open circles indicate data derived from the thin sample experiment and triangles indicate data derived from the thick sample experiment. At the incident neutron energies corresponding to the solid points the thin sample satisfied the condition for equation (8) (i.e. transmitted more than 98% of the incident neutrons). The open circles correspond to neutron energies for which this condition was not satisfied and these data include a correction for the effective thickness of the thin sample. In some regions between resonances where the thick sample satisfied the condition for eq. (8), the thick sample data (triangles) were preferred, since this sample gave a higher fission yield and hence a more accurate result. The cross section data shown in fig. 12 are in good agreement with those listed by Hughes and Schwartz[12]).

For fission cross section measurements the fission neutron detection method has some advantages over fission fragment detection, where a thin sample, itself enclosed in a fission chamber or gas scintillation counter, is essential. In the neutron detection method thick samples may be used, alpha-activity in the sample is no problem and millimicrosecond time-of-flight resolution is possible assuming that an organic scintillator is the neutron detector. However, it is essential that only neutrons are counted and, in particular, that gamma-rays are not counted; the neutron discriminating scintillation counter fulfils this requirement ideally.

7. The Nature of the Decay Time Differences

The physical effects behind the decay time differences are a subject of interest in their own right. For our purposes they are of particular interest in so far as they explain the scintillator behaviour observed and reported in section 3; that is, that diphenylacetylene crystals, unlike anthracene, stilbene and quaterphenyl, do not show an effective decay time difference; that liquid scintillators show such a difference only provided they do not contain dissolved oxygen; that plastic scintillators show, if anything, only a very small difference.

Scintillation decay shapes have been studied by Harrison[7]), Swank[5]), Wright[1]), Kallmann and Brucker[6]) and Owen[4]). From their data one might conclude that in general for organic scintillators, the scintillation decay may be described as the sum of several exponential components, one millimicrosecond "fast" component, responsible for 80% or more of the total emission, and one or more "slow" components of periods between 0.1 μsec and 100 μsec. Harrison[7]) originally showed that these slow components were appreciable in scintillations produced by X-rays in anthracene and stilbene, though they were not observed in liquid scintillators (presumably containing dissolved oxygen). Kallmann and Brucker[6]) determined that the fast component periods were virtually identical for alpha-particle and electron scintillations respectively in a wide range of crystal, liquid and plastic scintillators, including anthracene and stilbene. Owen[4]) showed that the slow component periods were the same for proton and electron scintillations respectively in anthracene, stilbene and quaterphenyl crystals and also in oxygen-free liquid scintillators but that the proportion of slow component emission was higher (and that of fast component lower) in proton scintillations. In other words, the nett, or effective, decay time for protons is longer than that for electrons in these scintillators because proton scintillations contain a higher proportion of slow components.

After Owen's conclusions we might presume that those scintillators which do not show a decay time difference for protons and electrons must either: (1) emit little slow component or; (2) emit similar proportions of slow component for both protons and electrons. Liquid scintillators containing dissolved oxygen and plastic scintillators would seem to fall into category (1), from Harrison's observation[7]) that slow components are negligible in the former and responsible for only 10% or less of the light emitted by the latter. Diphenylacetylene crystals might fall into either category, for although it has been reported that these emit slow components[5]) it is not established whether the proportion of slow

emission is comparable with that emitted by anthracene or stilbene, for example.

Kallmann and Brucker[6]) have suggested that relatively slow ion recombination processes in the scintillator might be the indirect cause of the slow components. Extending their ideas we might interpret the different effective decay times of, for example, stilbene for protons and electrons as follows. A particle (proton or electron) in stopping in the scintillator produces electronically excited molecules, M*, and ionized molecules, M^+, along its track. Ignoring intermolecular energy transfer for the moment, excited molecules decay by either (i) emitting a photon or (ii) quenching, that is conversion of their electronic excitation energy into vibrational energy:

$$\begin{aligned} &M^* \rightarrow M + \text{photon (i)} \\ &M^* \rightarrow M + \text{heat (ii)} . \end{aligned} \qquad \text{(A)}$$

Ionized molecules undergo the additional step of recombination:

$$M^+ + e^- \rightarrow M^* \qquad \text{(B)}$$

and the excited molecules formed in (B) decay according to (A). For some of the ionized molecules the recombination (B) may be a relatively slow process ($\approx 10^{-7}$ sec or more) dictated by the slow diffusion of electrons back to them. In (A) the probability of decay by emission, (i), rather than by quenching, (ii), depends not only on the molecule, but also on its environment. For example it is well known[11]) that the light output (pulse height) from an organic scintillator is not proportional to particle energy for heavily ionizing particles and that the light output for a proton is less than that for an electron of equal energy. As formulated by Birks, Wright[15]) and Kallmann and Brucker[6]) the light output is a function of the initial ionization and excitation density (density of M^+ and M*) along the track of the particle in the scintillator. In the environment of the track additional modes of quenching are available to an excited molecule, e.g.[6,15,16]) through interaction with other excited molecules or ions or transfer of excitation energy to quenching centres produced by radiation damage etc. This quenching is accentuated and hence the light output is less for a more heavily ionizing particle. In terms of equations (A) the relative probability of decay by (ii) rather than by (i) is increased by a higher initial excitation density, as for example in a proton track compared to an electron track.

Now suppose we analyse the light in a scintillation into two components, (a) and (b), which originate respectively from the initial M* and from the M* from slow recombinations of the initial M^+. Component (a) is thus attributed entirely to branch (i) of equations (A) and its decay time is of the order of the natural lifetime (millimicroseconds) of the excited molecule, i.e. "fast". Moreover for a proton and an electron of the same energy we get fewer component (a), or "fast" photons from the proton. Suppose we get f_e and f_p ($< f_e$) "fast" photons from the electron and proton respectively.

In the production of component (b) the relatively slow initial recombination step, (B) has two important effects. Firstly this component is "slow" because its decay time is essentially the recombination time; the decay process is analagous to a radioactive series in which the half-life of a long-lived parent determines the rate of decay of a short-lived daughter. Secondly, because the recombination is slow, the M* formed in (B) are born into an environment where the excitation density is much less than it was initially; consequently they are more likely to emit (instead of being quenched) than the M* produced directly by the incident particle. Thus if we get s_e "slow" photons from an electron and s_p "slow" photons from a proton of the same energy, though s_p may also be less than s_e, we may expect s_p/s_e to exceed f_p/f_e. It follows that the proportion of slow component in the proton scintillation, $s_p/(f_p + s_p)$ is more than that, $s_e/(f_e + s_e)$, in the electron scintillation, as has been observed experimentally.

Since it is known that electronic excitation energy may be transferred from one scintillator

[15]) J. B. Birks, Proc. Phys. Soc. A **64** (1951) 874; G. T. Wright, Phys. Rev. **91** (1953) 1282.

[16]) G. T. Wright, Proc. Phys. Soc. B **68** (1955) 929.

molecule to another[17]) we should, to be exact, consider energy transfer as an alternative mode of decay in equations (A). In the case of stilbene however, this would not affect the qualitative result, since energy transfer generally leads to other stilbene molecules being excited and these must eventually decay by either (i) or (ii) in equations (A). Energy transfer is more important in liquid and solid solution scintillators for in these it is the solvent (e.g. toluene or polystyrene) which is initially excited and excitation energy is transferred to a relatively small proportion (1 to 10%) of solute (e.g. p-terphenyl, PPO or POPOP) which emits. However the above qualitative description may still be valid for solution scintillators provided it is read that the processes in (A) and (B) apply to the solvent and that branch (i) of (A) describes, not solvent emission, but the solvent to solute energy transfer which leads eventually to emission from the solute.

The basis of the above interpretation, namely that the slow components may be attributed, indirectly, to slow recombination processes, would perhaps require more justification than can at present be provided. An alternative explanation, suggested by Harrison[7]), is that some molecules are initially excited to long-lived ($\approx 10^{-7}$ sec) triplet states and that these decay by acquiring sufficient vibrational energy to reach the singlet first excited electronic state, from which they decay according to (A). However, the fact that the decay time difference in anthracene and stilbene does not depend on crystal temperature (section 3) does not favour this explanation; one would expect that the triplet-singlet transition and hence the proportion of slow component in the scintillation would depend on the crystal temperature.

The fact that dissolved oxygen removes, or reduces, the slow components from liquid scintillators also seems to favour recombination processes rather than long-lived triplet states. We might infer that the effects produced by the oxygen are associated with the unpaired electrons in the O_2 molecule which lead to its high electron affinity. The threshold energy for electron capture by O_2 is about 3 eV[18]) and is thus within the expected range of energy of the ionization electrons produced in the scintillators. It is thus feasible that O_2 molecules in the scintillator might compete with ionized scintillator molecules for the ionization electrons, thus reducing the number of recombinations and hence the proportion of slow component which these eventually produce. On the other hand radiation chemistry studies[19]) have suggested that for a given incident particle and energy more triplet states are excited in organic solutions containing dissolved oxygen than in those that are oxygen-free; so in scintillators we should expect to see any slow component from long-lived triplet states increase in proportion when oxygen is dissolved in the scintillator. In fact the opposite is observed; the addition of oxygen removes or reduces the proportion of slow component, thus favouring the recombination processes rather than the long-lived triplet states.

Acknowledgements

The author is indebted to Dr. E. Bretscher for his support and interest in this work. He also wishes to thank Mr. J. E. Jolly for valuable assistance, the A.E.R.E. Linear Accelerator Group for their co-operation and Drs. S. K. Hutchinson and R. A. Lapage (A.W.R.E.) and Nuclear Enterprises (G.B.) Ltd., for providing scintillators for the experiments. The results of this paper were discussed with Drs. E. B. Paul, W. M. Lomer, E. R. Rae, R. B. Schwartz and Mr. F. W. K. Firk and the author is indebted to them for many helpful suggestions and criticisms.

[17]) T. Förster, Fluoreszenz Organischer Verbindungen (Gottingen, 1951);
H. Kallmann and M. Furst, Phys. Rev. **81** (1951) 853; Phys. Rev. **94** (1954) 503; Phys. Rev. **96** (1954) 902;
J. B. Birks, Phys. Rev. **94** (1954) 1567.

[18]) F. H. Field and J. L. Franklin, Electron Impact Phenomena (Academic Press Inc., 1957) p. 313.

[19]) C. R. Reid, Excited States in Chemistry and Biology (Pergamon, London, 1957) p. 180.

NUCLEAR INSTRUMENTS AND METHODS 4 (1959) 164–166; NORTH-HOLLAND PUBLISHING CO.

A PULSE-HEIGHT STORAGE CIRCUIT OF HIGH STABILITY

K. W. OGILVIE and D. PAIX

The F.B.S. Falkiner Nuclear Research and Adolph Basser Computing Laboratories†
School of Physics, The University of Sydney, Sydney

Received 15 January 1959

A stable circuit suitable for long time storage of the height of negative microsecond pulses is described. The gain stability and linearity are better than one percent over periods of several weeks. Performance data are presented.

1. Introduction

Temporary storage of information presented in the form of the height of microsecond pulses is often required before recording. This can be carried out by lengthening them, or by setting up a direct voltage proportional to pulse height. These procedures are also often useful in the process of analogue to digital conversion, and several circuits to accomplish them have been published in recent years. They are described in a review by Meyer[1]).

Although other methods have been used[2-7]) the present circuit follows the scheme employed by Elmore and Sands[8]), Bernstein[9]) and Brennan *et al.*[10]), whereby a capacitor is charged to a potential proportional to the peak value of the pulse. It will accept negative input pulses over the range 0 to 120 volts which have an average rate of rise not exceeding 100 volts per μsec. The gain stability achieved is better than 1% over periods of several weeks when running under very unfavourable conditions of temperature and humidity, and the linearity is of the same order and very stable. The storage time is in practice limited solely by the circuits connected to the terminals of the output capacitor, which has a capacitance of 0.5 μF.

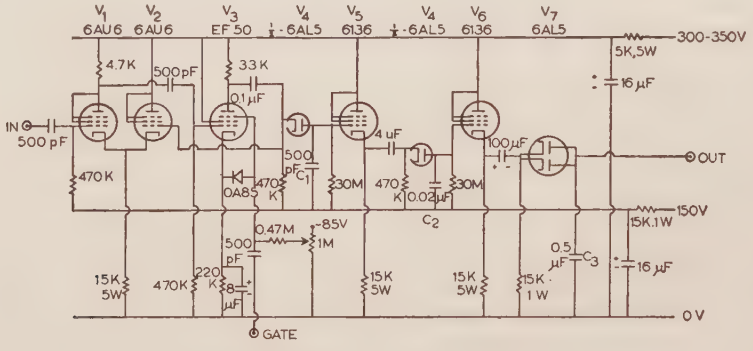

Fig. 1. Circuit diagram of pulse storage circuit.

† Also supported by the Nuclear Research Foundation within the University of Sydney.

[1]) M. A. Meyer, Nuclear Instruments **1** (1957) 62.
[2]) J. F. Craib, Electronics **24** (1951) 129.
[3]) L. Reiffel and G. M. Burgwald, Electronics **25** (1952) 186.
[4]) H. I. West and L. G. Mann, Rev. Scient. Instr. **25** (1954) 129.
[5]) R. S. Foote and H. W. Koch, Rev. Scient. Instr. **25** (1954) 746.
[6]) W. A. Hunt *et al.*, Rev. Scient. Instr. **25** (1954) 268.
[7]) A. Grabel, Elect. Engng. **75** (1956) 176.
[8]) Elmore and Sands, Electronics (McGraw Hill Book Co., 1949).
[9]) W. Bernstein *et al.*, Rev. Scient. Instr. **24** (1953) 437.
[10]) M. H. Brennan *et al.*, Nature **182** (1958) 905.

2. Description

A gated feedback amplifier with a gain of unity charges the first of three storage capacitors, C_1 in fig. 1. This is followed by two further pulse stretching cathode followers charging capacitors C_2 and C_3 through hot cathode diodes.

The size of C_3, the main store, was chosen to be 0.5 μF to ensure storage for several minutes with 1% loss and rather a large external leakage. The value of C_1, on the other hand, is limited by the charging current which the EF50 can deliver and by the desired rate of rise of the signal. With the value chosen, 500 pF, a pulse with mean rate of rise of 100 volts per microsecond is just followed. The obsolescent valve type EF50 is used in position V_3 because of its suppressor characteristic and its availability. A more modern type which would require a smaller gating pulse could be used.

The choice of C_2 is decided by the condition $C_3/C_2 \approx C_2/C_1$, which leads to a value of 0.02 μF. The time constants at the grids of V_5 and V_6 are chosen to permit a decay of charge of about 3% during the charging of the next capacitor, and the times taken to fully charge C_1, C_2 and C_3 in response to a 100 V signal are 1 μs, 0.3 ms and 5 ms respectively. The corresponding grid resistors are rather large by usual standards, but the use of the 6136 valve, a special quality version of the 6AU6, leads to a satisfactory operation. All the stages are condenser coupled so that small variations in the D.C. conditions do not effect the pulse response.

The gain of each cathode follower is 0.97, so that the total gain is 0.88, compared with the observed value of 0.8 $\pm$ 0.05. The storage time constants are such that the gain is only slightly dependent upon them. Approximately 30 mA is drawn from the + 300 V line, which need not be regulated, and less than 1 mA from the + 150 V and — 85 V supplies. If a valve with short suppressor grid base is substituted for the EF50 the negative supply voltage can be correspondingly reduced. The heater supply need not be regulated, but must be kept above 6.0 volts.

Although the diode charging C_3 should have a teflon socket to reduce leakage, C_3 itself is the only special component. With a polystyrene dielectric, its leakage resistance is greater than 2×10^4 megohms. When charged to about 150 V and left in the laboratory on open circuit the decay of charge in 24 hours was about 2%.

3. Circuit Performance

Standard flat topped pulses, rising at approximately 100 volts per microsecond to amplitudes between 8.2 V and 105 V were applied together with a gating pulse of + 50 V amplitude. This gating signal must rise to full amplitude in 0.2 μs, and it produces a pedestal of less than

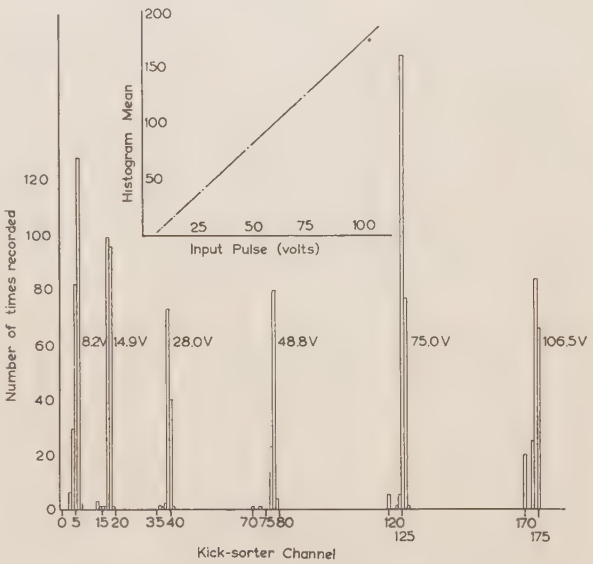

Fig. 2. Results of stability tests on storage circuit.

1.5 V on the output. Gated operation is very satisfactory when input pulses are not frequent, as it reduces the possibility of false readings due to pickup.

About 20 ms after the input pulse the stored voltage was measured by a 199 channel pulse height analyser of the design described by Wilkinson[11]). The recording was finally carried out on a standard punched card, appearing as a number between 0 and 199. Several pulses were recorded per hour over a long period as a test of stability. The pulse amplitude was derived from

[11]) D. H. Wilkinson, Proc. Camb. Phil. Soc. **46** (1950) 508.

the potential across two 85A2 voltage regulator tubes in series.

Histograms obtained for each of six pulse height settings are shown in fig. 2. Each represents results for a period of at least 24 hours. When examining them it should be borne in mind that the Wilkinson type analyser, which counts pulses from a free running oscillator for a period of time proportional to the pulse height, records a sequence of pulses of perfectly uniform height in two adjacent channels. An inset in fig. 2 shows how the mean recorded pulse height varies with the input pulse size.

No importance should be attached to the intercept, as it depends upon the recording system.

The data shown in fig. 2 were obtained over a period of several weeks, during which time the equipment was running continuously.

Acknowledgement

The authors would like to thank Professor Messel for the excellent laboratory facilities. We are also indebted to Dr. H. D. Rathgeber for helpful discussions. One of us (D. P.) would like to thank the University of Sydney for provision of a grant.

NUCLEAR INSTRUMENTS AND METHODS 4 (1959) 167–170; NORTH-HOLLAND PUBLISHING CO.

A METHOD FOR THE PREPARATION OF VERY THIN FOILS†

E. KASHY, R. R. PERRY and J. R. RISSER

The Rice Institute, Houston, Texas

Received 11 February 1959

A method for the preparation of self-supporting carbon foils of thicknesses ranging between 4 micrograms per cm² and 30 micrograms per cm², and of areas ranging between 0.25 cm² and 1 cm² is outlined. The essential features of the method are such that its application is not restricted to carbon.

1. Introduction

Thin self-supporting foils appear to have increasingly important applications in precision nuclear experiments involving reactions and scattering of low energy charged particles. In the case of reactions, thin evaporated films on heavy backings have long been used. In elastic scattering experiments, however, the energy difference between particles scattered from the backing and from the target is usually so small that a backing of appreciable thickness cannot be used.

Our first efforts to obtain thin self-supporting foils were made in the course of experiments on the elastic scattering of 2–5 MeV protons and alpha particles from C^{13}. The hope of avoiding the cost of filling our large scattering chamber with enriched hydrocarbon gas or of designing a new small gas scattering chamber furnished the motive. We subsequently applied the technique in experiments on the scattering of 0.5–2 MeV deuterons from C^{12}. These experiments involved a narrow resonance of well known width (5 keV at 1.44 MeV). With our thinnest foils, we were able to reproduce the elastic shape of this resonance.

The advantages of substituting self-supporting foils for gas target in elastic scattering experiments go far beyond cost savings in rare materials like C^{13}. Data-taking with a foil is considerably faster than with a gas target for several reasons. The stabilization of gas temperature and pressure in a gas scattering chamber is a time consuming process. Since cross section values depend critically on these parameters, checks and adjustments must constantly be made. Except in the immediate neighborhood of resonances, achievable gas target thicknesses are generally less than optimum for fast data-taking. Possibly more important than convenience and savings in time is the sometimes greater certainty in the energy of particles incident on the front face of the target. In the case of a foil, this energy is determined by the analyzing system of the accelerator, while in the case of a gas target, it is necessary to estimate the energy loss of the beam in traversing the differential pumping tube and that part of the scattering chamber between the exit slit of the differential tube and the target. The determination of target thickness constitutes a minor problem in the use of thin foils, since they cannot be weighed when made by our method. An indirect determination, however, in terms of the Rutherford cross section at forward angles and low energy can be made quite accurately.

In addition to direct use of thin carbon foils for scattering experiments in carbon, we have used them as backing for evaporated targets of other materials. With sufficiently few scattered particles from the backing and a sufficient difference in mass number between target and backing materials, elastic peaks can be resolved

† This work supported in part by the U. S. Atomic Energy Commission.

well forward of 90° in the center of mass system. An example of resolved scattered protons from Fe^{54} on a thin C^{12} foil is included at the end of this paper. It is hoped also that other target materials than carbon can be made self-supporting. The problem is mainly one of chemistry involving the relative solubility of the deposited target material and the backing upon which it has been deposited.

In general our thin carbon foils have not been ruptured by the passage of microampere beams of 1 MeV protons and deuterons. They, therefore, may prove useful as "beam strippers" in changing the ionization state of an accelerator beam and in other applications.

2. Experimental Technique

In the method we have used, the carbon was deposited on a nickel foil and the nickel was then removed over a limited area, leaving a self-supporting carbon foil over that area. The deposition of the carbon was made by heating the nickel foil in a chamber containing methyl iodide vapor. The nickel foil, which was cut rectangularly, one and one-half inches long by three-quarter inch wide, was mounted between two electrodes in the chamber (see fig. 1) and heated to a dull red by the passage of current. This, for a 0.00025 inch thick nickel foil, corresponded to a voltage of approximately 1.2 volts and a current of 15 amperes through the foil. The pressure of methyl iodide used in the chamber varied from 0.1 to 1 inch of mercury depending upon the thickness of the carbon foil desired. Since the carbon is deposited on both sides of the nickel, we used two foils, back to back, in the chamber, thereby obtaining two carbon depositions at a time. The nickel foils which we used† had a bright and a dull side, and the best results were obtained by depositing the carbon on the dull side. The foils were then placed on an aluminium mounting in which a half-inch hole had been cut. Amphenol Polyweld 912 coil dope was used to attach the nickel foil to the aluminium mounting with the side of the foil with the carbon away from the cement. The aluminium blank was a rectangle, $2'' \times \frac{3}{4}'' \times 0.010''$. The surface of the aluminium was filed slightly to make it somewhat coarse, so that the coil dope would adhere better to the surface of the aluminium. The aluminium blank was then painted with the coil dope and the nickel with the carbon foil mounted. The edges of the hole were then carefully masked with coil dope to keep the acid from flowing between the nickel and the aluminium. Fig. 2 is an exaggerated view of the assembly before etching. The nickel was then etched from the opening in the aluminium mounting using an acid solution of one part sulfuric acid, two parts water, and two parts nitric acid. The rate of etching could be increased by heating the solution. When the reaction was completed, i.e., the nickel had been removed from the opening in the aluminium and only the carbon foil was left, the foil

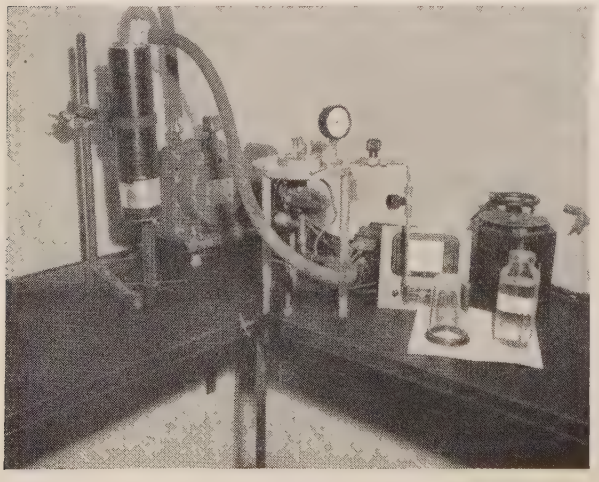

Fig. 1. Methyl iodide cracking chamber.

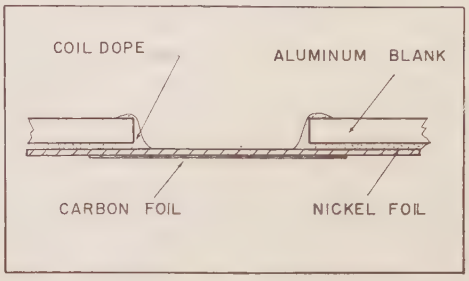

Fig. 2. Foil assembly before etching.

† The nickel was purchased from the Chromium Corporation of America.

was rinsed with a dilute nitric acid solution (one part nitric acid to three parts water). Finally, the foil was rinsed thoroughly with distilled water.

Of course, extreme caution must be used in each of the forgoing steps, since a foil of thickness we describe will survive very little strain, if any, during the etching process. However, the foil is quite strong after it has been allowed to dry. The etching and washing must be done using no more than a few drops of liquid on the foil at any one time. This can be done by constantly blotting away the various solutions. We have used medicine droppers for the liquids and highly absorbent paper for the blotting. The free carbon surface was always dry.

We have tried nickel foils of various thicknesses: 0.1, 0.25, 0.50, 0.75, 1.0, 1.5, and 2.0×10^{-3} inches. Of these, we found the 0.25×10^{-3} inch foil to be the most suitable for our purpose. Foils of thicknesses greater than 0.50×10^{-3} inch were found unsuitable. However, thinner nickel foils (as thin as 0.02×10^{-3} inch) would probably give satisfactory results, especially when the foil material is deposited on the nickel by evaporation. Of all the metals used, nickel was found most satisfactory with regard to freedom from pin holes in the carbon foil.

3. Results

In order to determine the thickness of our carbon foils we measured the yield of elastically scattered protons at a definite angle and energy through a measured solid angle, using the Rice Institute 5.5 MeV Van de Graaff accelerator. Since we can measure the number of protons incident upon the target by charge integration in the Faraday cup, we are able to calculate the thickness of our C^{12} target from the published values of the differential cross section[1]) for this reaction at a given angle and energy in the following way:

$$t = \frac{12}{0.602 \times 10^{24}} \times \frac{N}{\left(\frac{d\sigma}{d\Omega}\right)_L d\Omega I}$$

where

N = number of scattered particles counted.
$d\Omega$ = solid angle subtended by the counter.
I = number of incident particles
$= \frac{\text{integrated charge}}{\text{charge per particle}}$.
t = thickness in g/cm².

$(d\sigma/d\Omega)_L$ must be calculated from published values of the center of mass differential cross section

$$\left(\frac{d\sigma}{d\Omega}\right)_{c.m.} = C(\theta)\left(\frac{d\sigma}{d\Omega}\right)_L$$

[1]) Reich, Phillips and Russell, Phys. Rev. **104** (1956) 143.

Table 1

Experimental values of foil thicknesses

Foil No.	Yield (25 μcoulomb)	Thickness (μg/cm²)	Thickness† (Å)	Diameter of foil (cm)	Relative Success (completions/attempts)
1	4165	26.2	873	1.0	
2	4696	29.5	983	1.0	
3	3859	24.3	810	1.0	4/5
4	3347	21.1	703	1.0	
5	2730	17.2	573	1.0	
6	2391	15.0	500	1.0	3/5
7	3108	19.5	650	1.0	
8	1919	12.1	403	1.0	
9	1672	10.5	350	1.0	2/5
10	1044	6.6	220	0.7	
11	741	4.7	157	0.7	1/5

† We have assumed a density of 3 g/cm³ for the carbon foils.

where

$$C(\theta) = \frac{1 + \frac{m_1}{m_2}\cos\theta}{\left\{1 + 2\frac{m_1}{m_2}\cos\theta + \left(\frac{m_1}{m_2}\right)^2\right\}^{\frac{3}{2}}}$$

and θ = angle of scattering in the center of mass.

We have measured a series of foils with our counter at 162° in the center of mass system of coordinates and at a proton energy of 3.0 MeV, where $(d\sigma/d\Omega)_{c.m.}$ is 0.087×10^{-24} cm^2. The solid angle of our counter was 2.75×10^{-4} steradian and $C(\theta)$ for $\theta_{c.m.} = 162°$ is 1.180. In table 1, we have listed the thicknesses of some of our clean foils. The uncertainties in the cross section, solid angle measurement, and current integration give an overall uncertainty of 6% in the thickness of the foils. The last column estimates our relative success in making foils after some skill had been acquired. Clearly, this will vary greatly from person to person. We have checked the homogeneity of some of the foils and the results show that the foils are homogeneous to within 4% over most of the self-supporting area. Figs. 3 and 4 are spectra of 3 MeV scattered protons from several foils. In fig. 3 is the spectrum from an imperfectly washed foil, showing that residual impurities can be detected. Fig. 4A shows the spectrum from what we consider a clean foil. We used the foil of fig. 4A to illustrate the use of the C^{12} foils as backing material. Fig. 4B shows the same foil after Fe^{54} was deposited. The protons from Fe^{54} and from C^{12} were still resolved at laboratory angles greater than 80°.

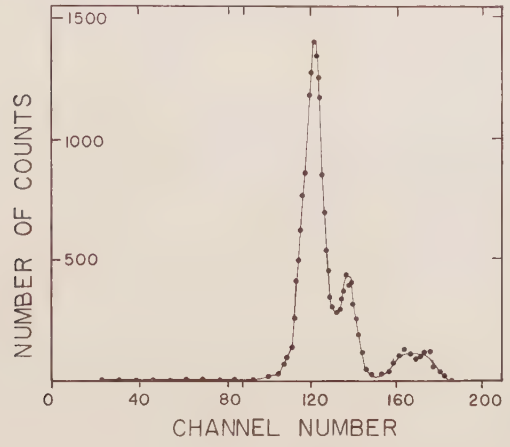

Fig. 3. Spectrum of protons scattered from an imperfectly washed foil, showing that impurities can be detected. The partially resolved low peak is from oxygen; the completely resolved low peak is from sulfur and nickel. The incident proton energy was 3 MeV and the C. M. angle was 162°.

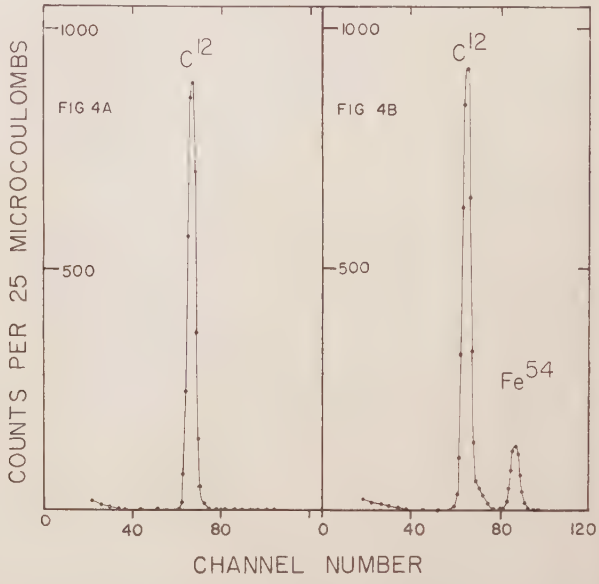

Fig. 4. Spectra of protons scattered from foil No. 3 of table 1, before and after Fe^{54} was deposited. The incident proton energy was 3 MeV and the C. M. angle was 162°.

NUCLEAR INSTRUMENTS AND METHODS 4 (1959) 171–180; NORTH-HOLLAND PUBLISHING CO.

THE RESPONSE TO HIGH-ENERGY GAMMA RAYS OF A NaI(Tl) SCINTILLATION SPECTROMETER

J. KOCKUM

Radiation Physics Department, University of Lund

and

N. STARFELT†

Institute of Physics, University of Lund

Received 4 February 1959

The pulse-height distributions produced by monoenergetic gamma rays in two NaI(Tl) spectrometers with diameters of 12,7 cm and lengths of 10.2 and 20.4 cm, respectively, have been studied.

The gamma rays were obtained from a Na^{22} and a Po-Be source (1.28 and 4.43 MeV respectively) and from the following proton induced reactions $F^{19}(p,\alpha\gamma)O^{16}$ (6.14 MeV); $B^{11}(p,\gamma)C^{12}$ (11.7 MeV); $Li^{7}(p,\gamma)Be^{8}$ (17.6 MeV); and $T(p,\gamma)He^{4}$ (20.3 MeV).

Measurements were performed with cylindric lead collimators of diameters ranging from 2.5 to 17 cm.

The variation of the shape of the response function with photon energy is shown to be rather small, thus permitting interpolation and extrapolation towards higher energy. A response function matrix covering the range from 4 to 34 MeV was constructed for the large spectrometer, using the pulse-height distributions obtained in this investigation and the 31 MeV distribution of Koch and Wyckoff. The inverse matrix was computed and used to compare an experimental bremsstrahlung spectrum from a 30 MeV synchrotron with a theoretical one. Good agreement was obtained.

1. Introduction

The total absorption scintillation spectrometer employing NaI(Tl) crystals, as described by Foote and Koch[1]), makes it possible to investigate gamma-ray spectra containing high energy photons.

In the study of continuous gamma-ray spectra[2]) it is necessary to know the variation of the response function of the spectrometer with the gamma-ray energy. This is easily obtained at energies below a few MeV, where both theoretical and experimental results[3,4]) are available, but at higher energies, where the escape from the crystal of bremsstrahlung emitted by compton and pair electrons is important, the number of published investigations is not as great[1,5–9]). Berger and Doggett[5]) extended their Monte-Carlo calculations for NaI(Tl) crystals of various sizes to 4.45 MeV. Foote and Koch[1]) experimentally determined the response function of a 12.7 cm diameter by 20.3 cm long crystal at 4.43, 11.7, and 17.6 MeV. For a similar crystal Koch and Wyckoff[6]) synthesized pulse-height distributions for 11 and 19 MeV gamma rays, respectively, using experimental pulse-height distributions produced by monoenergetic electrons of energies from 1 MeV to 20 MeV.

Koch and Wyckoff[9]) also obtained a good estimate of the response function of the large spectrometer at 31 and 78 MeV by analysis of measured continuous bremsstrahlung pulse distributions.

† Now at Research Institute of National Defence, Stockholm 80.

[1]) R. S. Foote and H. W. Koch, Rev. Sci. Instr. **25** (1954) 746.

[2]) N. Starfelt and H.W. Koch, Phys. Rev. **102** (1956) 1598.

[3]) D. Maeder, R. Müller and V. Wintersteiger, Helv. Phys. Acta **27** (1954) 3.

[4]) K. Lidén and N. Starfelt, Arkiv Fysik **7** (1954) 427.

[5]) M. J. Berger and J. Doggett, J. Res. N.B.S. **56** (1956) 355.

[6]) H. W. Koch and J. M. Wyckoff, J. Res. N.B.S. **56** (1956) 319.

[7]) J. G. Campbell and A. J. F. Boyle, Australian J. Phys. 6 (1953) 171.

[8]) A. E. Litherland, E. B. Paul, G. A. Bartholomew and H. E. Gove, Phys. Rev. **102** (1956) 208.

[9]) H. W. Koch and J. M. Wyckoff, IRE Transactions NS-5 (1958) 127.

Determination of photonuclear cross sections[10]) by the absorption method described by Foote and Koch[1,11]), requires knowledge of the response function up to about 30 MeV.

The present investigation was concerned with the pulse-height distributions produced by the gamma rays from the following proton induced reactions: $F^{19}(p,\alpha\gamma)O^{16}$, $B^{11}(p,\gamma)C^{12}$, $Li^{7}(p,\gamma)Be^{8}$, and $T(p,\gamma)He^{4}$, which give monoenergetic gamma-ray lines of 6.14, 11.7, 17.6, and 20.3 MeV, respectively. The 1.28 MeV line from a Na^{22} source, and the 4.43 MeV line from the reaction $Be^{9}(\alpha,n\gamma)C^{12}$ in a Po-Be-source were also studied. These latter gamma-ray sources have the advantage of being small and easily available, and can thus be used for calibration purposes in experiments in which no proton beam is available.

The most energetic gamma-ray line was thus at 20.3 MeV. It was therefore decided to investigate the possibility of determining the response function at higher energies by extrapolation.

The response function depends on the degree of collimation of the beam because of the escape of secondary photons through the sides of the crystal. Therefore the pulse-height distributions were measured with collimators ranging from 2.5 to 17 cm in diameter. Special interest was focused on the variation in relative height of the full energy peak and the peak produced by escape of one annihilation photon and the variation in half-width of the composite peak.

2. Experiment

The total absorption scintillation spectrometer (used in this experiment) employed two Harshaw NaI(Tl) crystals 12.7 cm in diameter by 10.2 cm in length, canned in copper containers in conjunction with DuMont 6364 photomultipliers. Response functions were recorded both with a single crystal and with the two crystals mounted so as to form a cylindrical spectrometer of a total length of 20.4 cm (fig. 1). In the latter case the gamma-ray beam passed through one of the photomultipliers. In order to decrease the effect of non-uniformity of the photocathode, 4 cm of perspex was used as a light pipe between the first crystal and its photomultiplier. The whole assembly was shielded by 3 cm Fe and 10 cm Pb. In the experiments with the Po-Be and T + p sources a further neutron shield consisting of 32 cm of a mixture of boric acid and paraffin in front and 16 cm around the rest of the crystals was applied. When both crystals were used, each photomultiplier was fed from its own high voltage supply, and the pulses were added together after proper adjustment of peak pulse height from each crystal. The pulse distribution was then analyzed in a Hutchinson-Scarrott type 100-channel pulse-height analyzer.

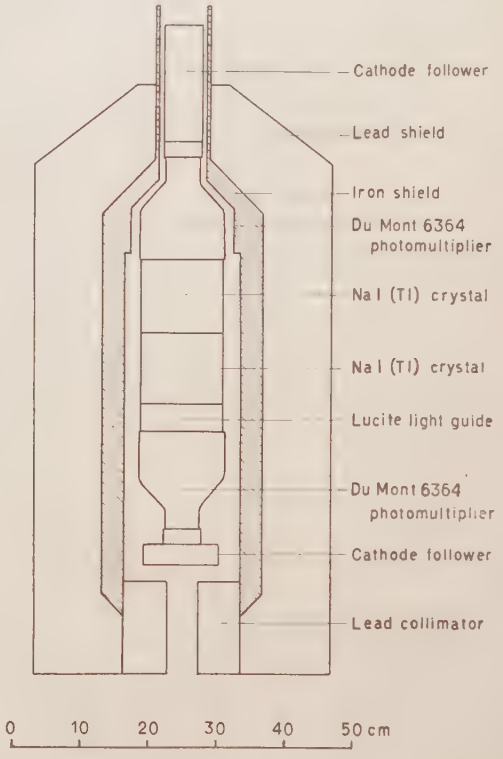

Fig. 1. Experimental arrangement.

Lead collimators of diameters 2.5, 4.5, 7, and 17 cm, respectively, were used. The largest collimator simply means a 17 cm hole in the lead shield which exposes the entire front surface of the crystal. Only the 4.5 cm collimator of the two-crystal spectrometer was used.

[10]) J. Kockum and N. Starfelt, (to be published).

[11]) H. W. Koch and R. S. Foote, Nucleonics **12**, No. 3 (1954) 51.

$Be^9(\alpha,n\gamma)C^{12}$

The source of the 4.43 MeV gamma rays was a 100 mC Po-Be source. The neutron background was troublesome, but this disadvantage was more than outweighed by the fact that the source is portable.

The protons used in the (p,γ)-reactions were accelerated in a van de Graaff generator. The pulse-height distributions were measured at an angle of 90° to the proton beam and, when permitted by the intensity of the gamma-ray line in question, the distance target to crystal front was kept at 75 cm.

$F^{19}(p,\alpha\gamma)O^{16}$

Good intensity of the 6.14 MeV line is readily obtained with the use of a thick CaF_2 target. By maintaining the proton energy below the resonance at 870 keV the intensity of the 6.9 and 7.1 MeV gamma rays can be kept at such a low level that they can easily be corrected for.

$B^{11}(p,\gamma)C^{12}$

A deposit of boron on a copper plate was used as a target. The proton energy was kept at 300 keV to avoid gamma rays other than 4.43, 11.7 and 16.1 MeV. The intensity obtained was rather low and therefore the only collimators used were 4.5 and 17 cm.

$Li^7(p,\gamma)Be^8$

A good intensity of the 17.6 MeV gamma-ray line was obtained when a 0.8 MeV proton beam struck a Li-metal target. The large contamination from the broad line at 14.8 MeV somewhat masked the pulse height distribution but it could be corrected for.

$T(p,\gamma)He^4$

The target consisted of a zirconium disk on which tritium had been adsorbed. The proton energy was kept at 0.9 MeV, well below the (p,n) threshold at 1.02 MeV in order to avoid neutron background. But neutron background occurred, probably due to (γ,n) reactions. The crystal was therefore shielded by extra borated paraffin. The gamma-ray intensity from this source was rather low, but counting times of several hours resulted in pulse-height distributions of sufficient statistical accuracy.

3. Treatment of the Data

Some of the observed uncorrected pulse-height distributions are given in fig. 2.

To correct for the background due to neutrons from the Po-Be source runs were performed with different lead absorbers. The logarithm of the total number of counts in every group of five channels (to improve the statistical accuracy) was plotted as a function of lead absorber thickness. The attenuation coefficient of gamma rays in lead is known but not that of the neutrons. A straight line representing the gamma ray attenuation and a constant number representing the counting rate due to neutrons penetrating the bulk of the lead shield were found by trial and error. Subtraction from the original absorption curve gave a straight line. The slope of this line gave the attenuation coefficient in lead for neutrons from the Po-Be source and extrapolation to zero absorber gave the number of pulses due to neutrons passing through the collimator. This permitted good estimation of the 4.43 MeV response function.

The 6.14 MeV pulse-height distribution was good (fig. 2). Pulse-height distributions corresponding to 6.9 and 7.1 MeV were derived from an assumed 6.14 MeV distribution and subtracted from the experimental composite curve to give the correct 6.14 MeV response function. Only that part of the curve below 1.5 MeV is uncertain because of the large background.

In the 11.7 MeV distribution the pulses from the accompanying 4.43 and 16.05 MeV lines are subtracted to give the 11.7 MeV response function.

The 17.6 MeV response function is more difficult to derive because of the width of the 14.8 MeV gamma-ray line, and slight contamination from lines at 13.5, 12.3, and 10.1 MeV. Inall and Boyle[12]) reported intensities for these last lines of 2%, 2%, and 0.5%, respectively, of

[12]) E. K. Inall and A. J. F. Boyle, Phil. Mag. **44** (1953) 1081.

the total gamma-ray intensity. According to Stearns and McDaniel[13]), the ratio of the intensity of the 17.6 MeV line to that of the 14.8 MeV line is 1.70 ± 0.20. Walker and McDaniel[14]) gave a width of the 14.8 MeV line equal to 2.1 MeV. In their paper both lines were described as being of the same shape. The width of the 14.8 MeV pulse height distribution was set equal to the square root of the sum of the squares of the spectrometer line width and the

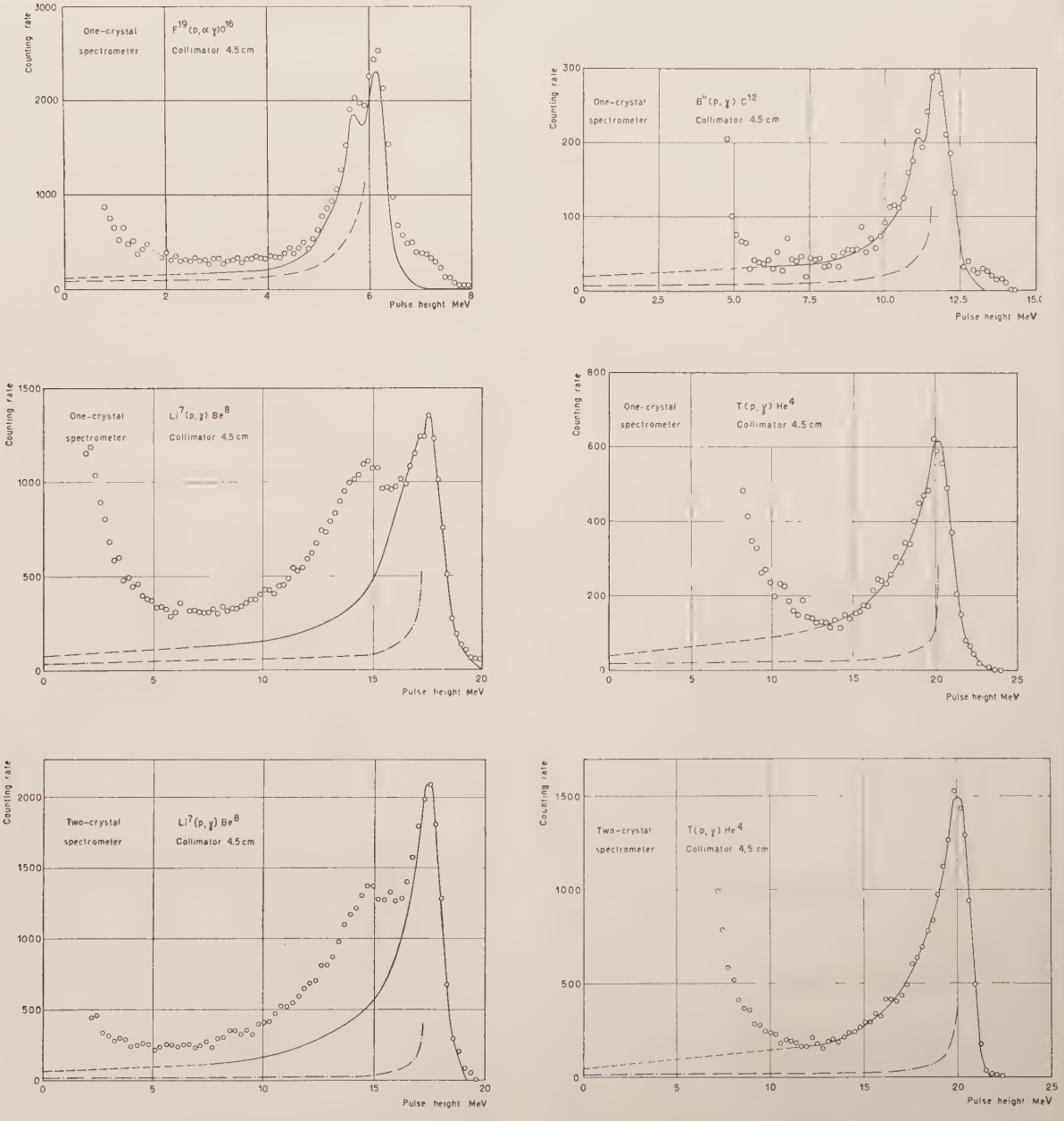

Fig. 2. Experimental pulse-height distributions produced by gamma rays of different energies in NaI(Tl) spectrometers of a diameter of 12.7 cm and of lengths of 10.2 cm and 20.4 cm, respectively. The uninterrupted curves are corrected for disturbing gamma-ray distributions and photons scattered from target holder and collimator. Experimentally uncertain parts of the curves are interrupted. Calculations of the tails of the pulse-height distributions taking into account the escape from the crystal of Compton photons and pair electrons are given as dot-dashed curves.

intrinsic line width. The 17.6 MeV response function was guessed, moved to 14.8 MeV and given the proper area and width. When the sum of the 17.6 and 14.8 MeV distributions determined in this way equalled the experimental curve minus correction for the three lines at 13.5, 12.3, and 10.1 MeV the 17.6 MeV distribution was said to be correct. Otherwise the procedure was repeated until agreement was obtained.

The 20.3 MeV distribution shows a large background at low energies, which makes the tail of the final curve rather uncertain. The 20.3 MeV gamma-ray line has a certain width due to the thick target used, but this is only 1.1% and therefore negligible compared with the resolving power of the spectrometer.

In the experiments with the two-crystal spectrometer, runs were made with T, Li and F in rapid succession with the same high-voltage settings. These gave a good linearity between peak pulse-height value and energy except for the experiment with 20.3 MeV in which the peak was shifted 0.2 MeV downwards. The same pulse height was ascribed to the peak of the tritium line obtained with the one-crystal spectrometer with a 4.5 cm collimator. The 17 cm collimator experiment was made immediately after the experiment with the 4.5 cm collimator and with the same energy scale.

3.1. COLLIMATOR EFFECTS AND SCATTERING IN THE TARGET HOLDER

The contribution to the observed pulse-height distributions by photons scattered from the brass tube around the target holder was estimated as well as that from the collimator walls and the build-up spectrum from photons penetrating the collimator material. Data were taken from White[15]) and, for the build-up spectrum, also from Goldstein and Wilkins[16]). All photon distributions were assumed to be uniform. According to this calculation the counting rate due to scattered photons was 8% of the total counting rate in the 6.14 MeV case, and then gradually dropping to 3% at 20 MeV.

In fig. 2 these contributions and the distributions due to accompanying weak gamma-ray lines are substracted from the experimental curves.

3.2. TAILS OF THE DISTRIBUTIONS

Though interest is concentrated on the peak of the response function in most applications, exact intensity determinations require knowledge of the shape of the whole curve. All distributions are rather uncertain at low energies owing to high background from accompanying gamma rays and neutrons. Therefore the contribution to the tail of the response function from Compton scattered photons and Compton and pair electrons escaping from the crystal was calculated. The Compton distribution was calculated in the way described by Koch and Wyckoff[6]) by extrapolating the data of Berger and Doggett[5]) to higher energies. The effect of escaping electrons was estimated assuming that the pair electrons formed in the last R cm of the crystal give a uniform pulse distribution. Here R is the average range in sodium iodide of an average pair electron. These calculated contributions to the response function are given in fig. 2. Especially with 6.14 MeV the experimental points indicate a horizontal tail with a higher number of pulses at zero energy than estimated. The final distributions are based on the average of these two curves. The estimated maximum error in the area under the curves at constant peak height thus obtained is 5% both at 6.1 and 20.3 MeV. The interrupted parts of the curves correspond to the region where the experimental points do not give any direct information about the distributions.

4. Results

The purpose of the investigation was to study the variation of the response function for a 10.2 cm long NaI(Tl) crystal with photon energy and collimator diameter and the possibil-

[13]) M. B. Stearns and B. D. McDaniel, Phys. Rev. **82** (1951) 450.

[14]) R. L. Walker and B. D. McDaniel, Phys. Rev. **74** (1948) 315.

[15]) Gladys White Grodstein, N.B.S. Circular 583 (1957).

[16]) H. Goldstein and J. E. Wilkins, U.S. Atomic Energy Commission NYO-3075 (1954).

TABLE 1

The relative half width, $\Delta\varepsilon/\varepsilon$, and the ratio, q, between the height of the full energy peak and that of the one-photon escape peak for the response function obtained with large NaI(Tl) crystals

a. NaI(Tl) 12.7 cm diameter by 10.2 cm long

Photon energy (MeV)	1.28	4.43		6.14		11.7		17.6		20.4
Collimator diameter (cm)	$\Delta\varepsilon/\varepsilon$%	$\Delta\varepsilon/\varepsilon$%	q%	$\Delta\varepsilon/\varepsilon$%	q%	$\Delta\varepsilon/\varepsilon$%	q%	$\Delta\varepsilon/\varepsilon$%	q%	$\Delta\varepsilon/\varepsilon$%
2.5				13.3	132					
4.5	9.2	16.1	172	14.9	123	12.8	143	14.5	109	15.3
7	10.0	17.7	139	16.0	112	13.3	—	17	—	
17	10.3	24.4	108	24.0	83	18.4	—	23.9	—	24.4

b. NaI(Tl) 12.7 cm diameter by 20. 4 cm long

4.5				13.6	148	10.3	—	10.5	—	11.7
4.5†						11.3		10.4		

† reference [1]).

ity of improving the resolution by using a 20.4 cm long spectrometer. Some of the results obtained are given in table 1. For one crystal the ratio between the full energy peak and the escape peak decreases and the width at half-height increases with increasing beam size (table 1a). Furthermore, if collimation is poor, escape of bremsstrahlung from the crystal shifts the peak towards lower pulse heights. The two-crystal spectrometer (table 1b) gives a much better resolution, the escape peak then not being detectable at energies above 6.14 MeV. This table also gives the results of Foote and Koch[1]) for 11.7 and 17.6 MeV. They used larger bin width for the 11.7 MeV experiment which

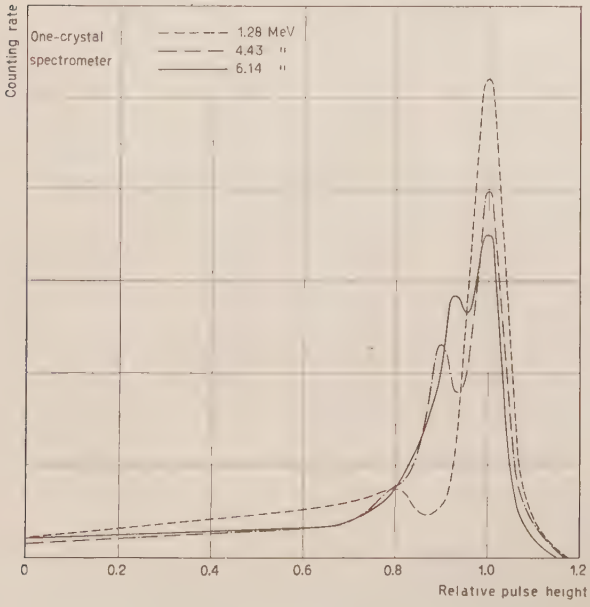

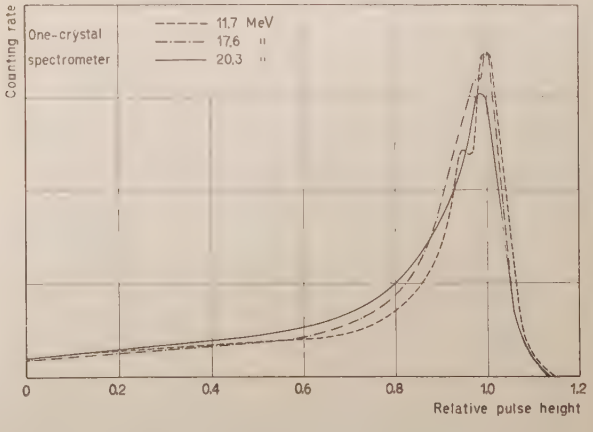

Fig. 3. Fully corrected experimental response function of a NaI(Tl) spectrometer, 12.7 cm in diameter and 10.2 cm long, obtained with a collimator 4.5 cm in diameter and a source to crystal distance of 75 cm.

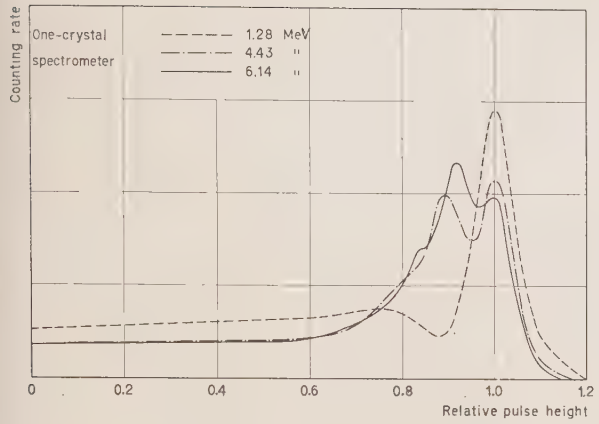

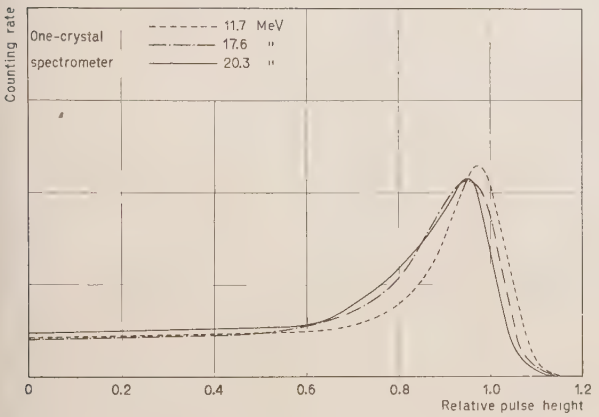

Fig. 4. Fully corrected experimental response function of a NaI(Tl) spectrometer, 12.7 cm in diameter and 10.2 cm long, obtained without collimator and a source to crystal distance of 75 cm.

explains the discrepancy between their and our results at this energy.

Figs. 3–5 show the variation of line shape with energy for collimators of 4.5 and 17 cm diameter, respectively. The pulse-height scale is relative, and the pulse height corresponding to the photon energy is set equal to unity. The areas under the curves are made equal to the crystal efficiency, $1 - e^{-\mu L}$ (fig. 6). The most striking feature at 4.5 cm is how little the shape of the response function varies with energy, especially at the higher energies where the one-photon escape peak is close to the main peak. This permits interpolation and even extrapolation towards higher energies.

When no collimator was used, the peak of the pulse-height distributions became broader and

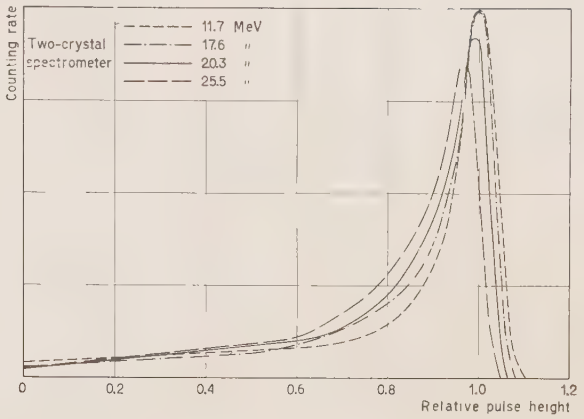

Fig. 5. Fully corrected experimental response function of a NaI(Tl) spectrometer, 12.7 cm in diameter and 20.4 cm long, obtained with a collimator 4.5 cm in diameter and a source to crystal distance of 75 cm. The 25.5 MeV curve is extrapolated from the other curves.

was shifted towards lower energy for 11.7, 17.6, and 20.3 MeV (fig. 4).

Fig. 5 shows the experimental curves for the two-crystal spectrometer at 11.7, 17.6, and 20.3 MeV as well as an extrapolated 25.5 MeV response function. Its shape was obtained by normalization of the experimental curves at the peak and extrapolation point by point. The peak pulse-height was obtained by interpolation

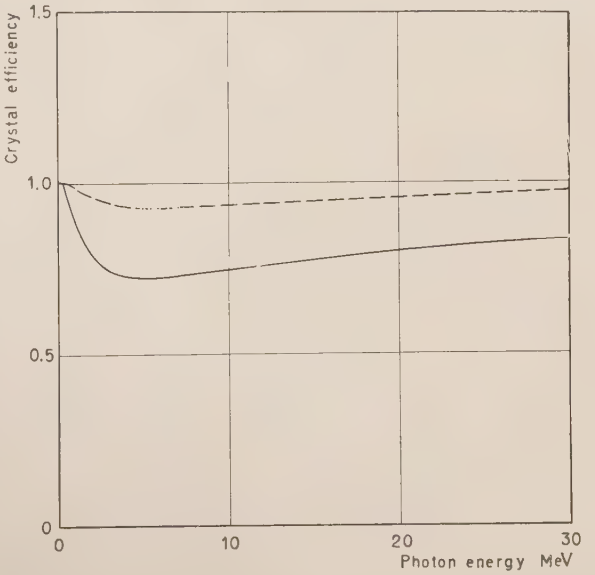

Fig. 6. Calculated efficiency ($1 - e^{-\mu L}$) of NaI(Tl) spectrometers, lengths 10.2 cm (solid curve) and 20.4 cm (dashed curve), respectively.

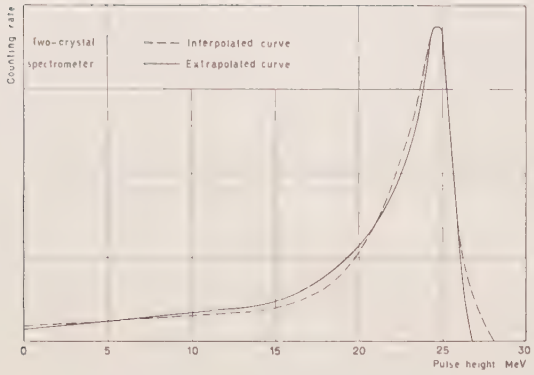

Fig. 7. Comparison between two 25.5 MeV pulse-height distributions, one (solid curve) extrapolated as shown in fig. 5 and the other one (dashed curve) interpolated between the 20.3 MeV distribution in fig. 5 and the 31 MeV distribution of Koch and Wyckoff[9]).

between the peak shifts at 20.3 MeV (0.2 MeV) in the present investigation and that at 31 MeV (1.8 MeV) in the investigation by Koch and Wyckoff[9]). Fig. 7 compares this extrapolated pulse distribution with a distribution interpolated between our 20.3 MeV function and the 31 MeV function of Koch and Wyckoff.

5. Analysis of Continuous Spectra

A continuous gamma-ray spectrum $N(k)$ gives rise to a pulse height distribution $P(\varepsilon)$ in the spectrometer, where k denotes photon energy and ε pulse height. The two distributions are related to each other through

$$P(\varepsilon)\mathrm{d}\varepsilon = \mathrm{d}\varepsilon \int_0^{k_{\max}} N(k)\, K(k,\varepsilon)\, (1 - \mathrm{e}^{-\mu L})\mathrm{d}k \qquad (1)$$

where $K(k,\varepsilon)$ is the response function of the spectrometer and $k_{\max}$ the maximum energy of the gamma-ray spectrum. This equation is easily transformed to a matrix equation which can be written[2])

$$< P(\varepsilon) > = M < N(k) > \qquad (2)$$

where $< P(\varepsilon) >$ and $< N(k) >$ are one-column matrices and M a square matrix whose elements are given by

$$M_{ji} = \frac{\int_{\Delta\varepsilon_j} \gamma \mathrm{d}\varepsilon \int_{\Delta k_i} K(k,\varepsilon)\, (1 - \mathrm{e}^{-\mu L})\, \mathrm{d}k}{\Delta\varepsilon_j} \qquad (3)$$

Δk_i and $\Delta\varepsilon_j$ are energy and pulse height intervals, respectively. N is obtained from eq. (2) through multiplication by the inverse matrix M^{-1}.

The error in N resulting from errors ΔP in P is given by

$$\Delta N(k_j) = [\sum (M_{ji}^{-1}\, \Delta P(\varepsilon_i))^2]^{\frac{1}{2}}. \qquad (4)$$

Thus $P(\varepsilon)$ and $K(k,\varepsilon)$ being experimentally determined it is not sufficient only to construct any matrix M and compute its inverse. To give the result a meaning the intervals must be chosen so that the enlargement of the experimental errors according to (4) is not excessive. If the intervals are made too narrow so as to require more information from the solution than is contained in the experiments the ΔN from eq. (4) may very well turn out to be much larger than N even if the accuracy in P is of the order of $\pm$ 1%.

A response function matrix was constructed for the two-crystal spectrometer in the energy region 4 to 34 MeV starting from the measured response function. At 31 MeV, $K(k,\varepsilon)$ was obtained from Koch and Wyckoff[8]) and, for energies between 20.3 and 31 MeV, by interpolation between the two experiments. The resulting matrix employing 2 MeV intervals is shown in table 2. The corresponding inverse matrix is given in table 3.

A 30 MeV bremsstrahlung spectrum from a synchrotron was recorded to check this response function matrix experimentally. The pulse distribution obtained with the NaI spectrometer as well as the photon spectrum obtained by multiplication by the matrix is shown in fig. 8, which also includes the theoretical bremsstrahlung spectrum as given by Penfold and Leiss[17]) which is known to represent the synchrotron spectrum with good accuracy. The experimental points in fig. 8 are seen to agree very well with the theoretical curve between 11 and 25 MeV. In this case the experimental inaccuracy, ΔP, in P gives a corresponding $\Delta N/N$ approximately 5 times larger than $\Delta P/P$ as marked in the figure. Narrower intervals in the matrix would lead to larger $\Delta N/N$ and wider intervals would

[17]) A. Penfold and J. Leiss, University of Illinois (May 1958).

result in a reduction in the information obtained about the details in N. The erratic behaviour of the experimental points above 25 MeV is due to insufficient knowledge about the shape of the high energy end of the response function at these energies. However, small errors in the matrix give rise to large errors in the photon spectrum only close to rapid changes in this spectrum, e.g. in a 40 MeV spectrum these errors would not show up at 27 MeV but rather

Table 2

Response function matrix

ε \ k	5	7	9	11	13	15	17	19	21	23	25	27	29	31	33
5	582	191	98	81	61	46	37	32	28	23	20	18	16	14	14
7	3	505	189	96	77	55	42	36	31	26	22	20	16	16	14
9		7	456	200	98	73	52	40	34	29	24	22	19	16	16
11			9	421	212	101	70	50	39	33	27	24	19	18	16
13				11	391	223	104	69	49	39	31	26	22	18	18
15					12	367	229	110	71	49	37	30	24	22	18
17						14	343	232	117	73	51	36	29	24	20
19							17	318	231	123	79	54	37	30	26
21								20	293	237	128	86	58	43	36
23									23	268	245	140	95	65	50
25										29	239	245	155	107	79
27											32	206	239	178	121
29												31	171	231	207
31													28	134	220
33													1	23	98

k represents the center of the photon interval (MeV), ε the energy corresponding to the center of the pulse-height interval (MeV). To yield the matrix elements the numbers in the table should be multiplied by 10^{-3}.

Table 3

Inverse response function matrix

k \ ε	5	7	9	11	13	15	17	19	21	23	25	27	29	31	33
5	1722	—650	— 98	— 135	— 42	— 35	— 26	— 24	— 21	— 7	— 17	— 2	— 34	51	— 106
7	—10	1996	—824	— 58	— 153	— 24	— 43	— 38	— 27	— 15	— 15	— 23	32	— 114	158
9		— 31	2227	—1051	23	— 162	— 16	— 47	— 35	— 24	— 15	— 23	— 35	69	— 162
11		1	— 48	2432	—1311	144	— 188	— 1	— 56	— 27	— 18	— 46	55	— 158	210
13			1	— 70	2644	—1599	291	— 223	21	— 79	— 2	— 31	— 43	108	— 259
15				2	— 89	2851	—1898	434	— 265	52	— 77	— 23	22	— 129	168
17					4	— 121	3107	—2264	598	— 330	138	— 124	14	— 38	33
19						7	— 175	3441	—2719	945	— 681	501	— 470	433	— 411
21						— 1	13	— 254	3884	—3518	1814	—1546	1 473	— 1 686	1 553
23							— 1	25	— 380	4595	—4975	3443	— 3 295	3 568	— 3 502
25								— 4	56	— 683	5865	—7541	6 694	— 7 009	6 506
27								1	— 12	143	—1226	8110	—12 555	14 306	—14 689
29									3	— 40	340	—2248	12 421	—23 766	29 637
31									— 1	12	— 106	703	— 3 884	19 572	—36 522
33										— 3	22	— 142	785	— 4 351	18 473

k denotes the center of the photon interval (MeV), ε the energy corresponding to the center of the pulse-height interval (MeV). To yield the matrix elements the numbers in the table should be multiplied by 10^{-3}.

at 35 MeV when using a matrix of the same accuracy as the one used here. The disagreement

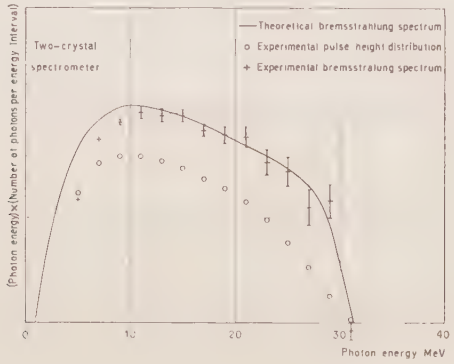

Fig. 8. Experimental check of the response function matrix (table 2 and 3). The circles represent a pulse-height distribution obtained in a NaI(Tl) spectrometer, 12.7 cm in diameter and 20.4 cm long with a synchrotron (maximum energy 30.5 MeV) and a 26 cm long aluminium absorber. The crosses show the experimental bremsstrahlung spectrum obtained by multiplying the pulse height distribution by the inverse matrix (table 3). The solid curve represents a theoretical bremsstrahlung spectrum[17]) with a maximum energy of 30.5 MeV attenuated in 26 cm of aluminium. This curve is normalized to the crosses between 13 and 25 MeV.

in fig. 8 below 11 MeV is not due to the matrix. The experiment was performed with a 26 cm aluminium absorber in the beam. The theoretical spectrum was corrected for the absorption to permit comparison with experiment. Small errors in the absorption coefficient of aluminium are important only below 15 MeV because the absorption is almost independent of energy above 15 MeV. An error in the determination of the pulse height corresponding to zero photon energy also influences the low energy points more than those at higher energies.

The matrix discussed here was used in an investigation of photonuclear absorption where the transmission of a continuous bremsstrahlung spectrum through long absorbers was studied[10]). The results of this investigation together with those demonstrated in fig. 8 show not only the possibilities in an analysis of a continuous pulse distribution as described here, but also its inevitable limitation due to the fairly large line width of the NaI scintillation spectrometer.

Acknowledgements

The authors wish to thank Dr. K. Lidén for never-tiring encouragement and interest, Dr. C-E. Fröberg for advice and help in performing the numerical computation, and Mr. E. Möller for invaluable aid in the experiments using the van de Graaff generator.

NUCLEAR INSTRUMENTS AND METHODS 4 (1959) 181–188; NORTH-HOLLAND PUBLISHING CO.

LE MOUVEMENT ANHARMONIQUE DES IONS DANS UN CYCLOTRON ET LE DIAGRAMME DE PHASE

R. KELLER

CERN, *Division du Synchro-Cyclotron, Genève*

Reçu le 18 Février 1959

It is shown that the equation of the orbits in a cyclotron and a synchro-cyclotron is identical with that of a pendulum. The equations of motion are then derived for the radius of the orbits and for the phase, for an adiabatic variation, such as occurs in practice. A numerical example is given of the calculation of the maximum energy and of phase bunching for a given cyclotron. To conclude, stockastic acceleration is illustrated by means of a phase diagram.

Il est possible de traiter le mouvement des ions dans un cyclotron de même que dans un synchro-cyclotron d'une façon extrêmement simple du moment que l'équation du mouvement des ions est identique à celle d'un pendule physique. Voici comment on peut déduire d'un seul coup d'oeil l'équation du mouvement pour un cyclotron.

1. Le rayon de l'orbite et la phase

Ce n'est pas le mouvement point par point qui intéresse, mais seulement la variation du rayon de l'orbite ainsi que de la phase par rapport au champ accélérateur. Soit l'induction magnétique $B(r)$ fonction du rayon r, de direction verticale dans le plan médian, et soit le champ électrique de haute fréquence $-E(r)\cos\omega t$ de direction horizontale, ω étant la fréquence angulaire du générateur de haute fréquence. Il est préférable de définir le champ négativement, de sorte que nous ayons des grandeurs positives par la suite. Ce champ est la somme de deux champs tournant en sens opposés, d'amplitude $\frac{1}{2}E(r)$, c'est-à-dire:

$$E(r)\cos\omega t = \tfrac{1}{2}E(r)\exp i\omega t + \tfrac{1}{2}E(r)\exp -i\omega t\,. \quad (1)$$

Si les ions tournent dans le sens $+\omega$, seul le terme en exp $i\omega t$ accélérera ces derniers, tandis que le terme en exp $-i\omega t$ ne se comportera que comme une petite perturbation négligeable. Soit maintenant le rayon vecteur $r\exp i(\omega t+\varphi)$ de la position de l'ion (voir fig. 1), φ étant la phase de l'ion par rapport au champ de haute fréquence. Or, une charge se déplaçant perpendiculairement aux lignes de force magnétique "voit" un champ électrique dont la direction est perpendiculaire à la fois aux lignes de force et à la direction du mouvement, et dont la valeur est égale à vB, v étant la vitesse. La particule est en équilibre si la force evB compense la force centrifuge $m\omega_s^2 r$ et la force due au champ de haute fréquence. On aura l'équation

$$\overrightarrow{evB} = \overrightarrow{m\omega_s^2 r} - \tfrac{1}{2}e\,\overrightarrow{E(r)}. \quad (2)$$

Disons maintenant que v est la somme vectorielle de la vitesse de rotation non perturbée $\omega_s r$ et d'une vitesse supplémentaire w due au champ $E(r)$

$$\vec{v} = \overrightarrow{\omega_s r} + \vec{w}\,. \quad (3)$$

En introduisant (3) dans (2) nous obtenons

$$\overrightarrow{e\omega_s r B} + \overrightarrow{ewB} = \overrightarrow{m\omega_s^2 r} - \tfrac{1}{2}e\,\overrightarrow{E(r)}\,. \quad (4)$$

Dans cette dernière équation les premiers vecteurs des deux membres sont parallèles entre eux, de même que les deux seconds vecteurs. Il vient donc $e\omega_s rB = m\omega_s^2 r$ et $ewB = -\frac{1}{2}E(r)$ ce qui conduit à deux résultats dont le premier aurait pu être déduit d'une façon plus directe:

$$\omega_s = \frac{eB}{m}\,. \quad (5)$$

Le second résultat est

$$w = -\frac{E(r)}{2B} \quad (6)$$

où w est tourné de $-90°$ par rapport au champ électrique (voir fig. 1).

Le champ tournant $-E(r)\exp i\omega t$ a donc comme effet de superposer vectoriellement à la

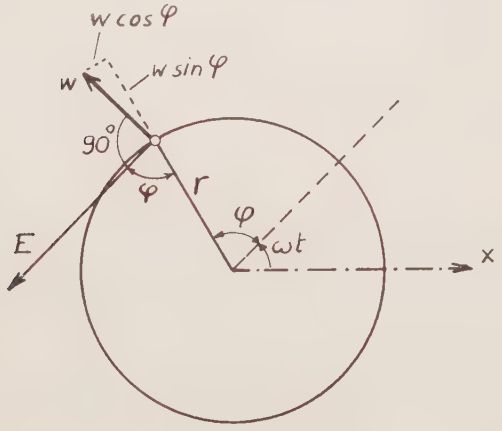

Fig. 1.

vitesse de rotation ωr une vitesse w qui désynchronise et accélère la particule. Comme le mouvement point par point est inintéressant, nous allons prendre un film dont les photos sont prises aux instants $\omega t = 0,\ 2\pi,\ 4\pi,\ 2n\pi$ c'est-à-dire une image stroboscopique du mouvement. Cette image s'appelle le "diagramme de phase". Les équations du mouvement peuvent être lues directement sur la fig. 1.

2. Le diagramme de phase

La variation du rayon est

$$\frac{\mathrm{d}r}{\mathrm{d}t} = w \sin \varphi \tag{7}$$

et la variation de phase

$$r\frac{\mathrm{d}\varphi}{\mathrm{d}t} = w \cos \varphi + r(\omega_s - \omega) \tag{8}$$

ou mieux

$$\frac{\mathrm{d}\varphi}{\mathrm{d}t} = \frac{w(r)\cos\varphi}{r} + \omega_s(r) - \omega(t)\,. \tag{8a}$$

Le terme $\omega_s - \omega$ exprime l'avance ou le retard de phase provoqué par le désaccord entre la fréquence synchrone ω_s (non pertubrée) et la fréquence d'excitation ω du générateur de haute fréquence. A chaque révolution la particule prend une avance de phase supplémentaire égale à $(\omega_s - \omega)\ T$. La fréquence ω_s est évidemment fonction de r. Si $\omega(t)$ varie dans le temps, ce sera le cas d'un synchro-cyclotron.

3. Le pendule de rotation

Le résultat ci-dessus, trouvé d'une manière simpliste, peut être démontré rigoureusement. Poursuivons la démonstration sur l'exemple du pendule de rotation non amorti. Nommons $-eE(r)\cos\omega t$ la force appliquée au pendule (cela pourrait être une force électrostatique agissant sur un pendule chargé). Les équations du mouvement sont

$$\ddot{x} = -\omega_s\dot{y} - \frac{eE(r)}{m}\cos\omega t \tag{9}$$

$$\ddot{y} = \omega_s\dot{x} \tag{10}$$

ω_s est la fréquence propre du pendule, qui vaut

$$\omega_s{}^2 = \frac{g}{\sqrt{R^2 - r^2}}\,. \tag{11}$$

Afin de mieux montrer l'analogie avec le cyclotron, nous posons arbitrairement $\omega_s = eB(r)/m$ où $B(r)$ n'est plus qu'une grandeur de calcul qui est déterminée par introduction de cette dernière formule dans (11).

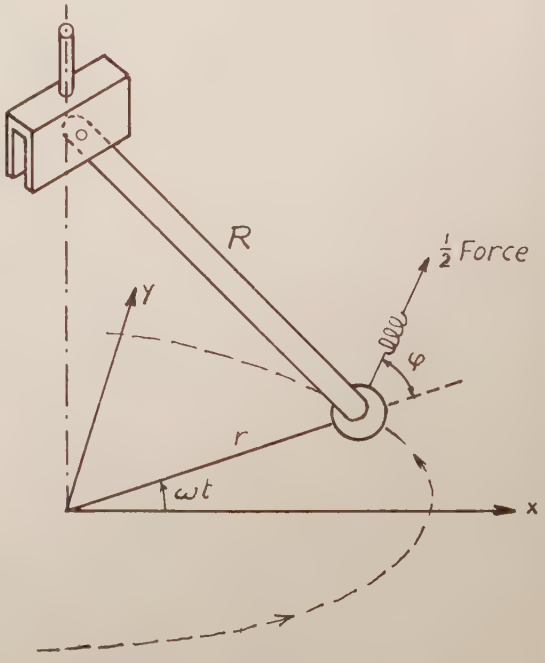

Fig. 2. Pendule de rotation.

Multiplions l'équation (10) par i et additionnons ceci à (9), il vient:

$$\ddot{r} - i\omega_s\dot{r} = -\omega_s w\,[\exp i\omega t + \exp -i\omega t] \quad (12)$$

avec

$$r = x + iy\,. \quad (13)$$

En vertu de la méthode conventionnelle pour résoudre l'équation différentielle (12) avec second membre, la solution est la somme d'une solution particulière $a \exp i\omega t + b \exp -i\omega t$ et de la solution générale $c \exp i\omega_s t$, où a, b et c sont des constantes. Mais cette façon de procéder ne mène pas à ce que nous cherchons. En fait, l'amplitude r varie et la phase φ aussi. Posons donc d'une façon non conventionnelle la solution suivante:

$$r = a(t) \exp i\,[\omega t + \varphi(t)] + b \exp -i\omega t + c \exp i\omega_s t \quad (14)$$

où a et φ sont fonctions du temps. Introduisons cette solution dans l'équation différentielle (12), mais en négligeant les termes en $\ddot{a}$, $\dot{a}\dot{\varphi}$ et $\ddot{\varphi}$. Cela revient à dire que $a(t)$ et $\varphi(t)$ doivent varier peu dans le laps de temps d'une période. La variation est alors, ce qu'on appelle, adiabatique. Ainsi nous obtenons

$$-a(\omega^2 + 2\omega\dot{\varphi} - \omega\omega_s - \omega_s\dot{\varphi}) + i\dot{a}\,(2\omega + 2\dot{\varphi} - \omega_s) = -\omega_s w \exp -i\varphi = -\omega_s w \cos\varphi + i\omega_s w \sin\varphi \quad (15)$$

et

$$b\omega\,(\omega + \omega_s) = \omega_s w\,. \quad (16)$$

Séparons encore la partie réelle de la partie imaginaire de (15), ce qui fait

$$a\,(\omega^2 + 2\omega\dot{\varphi} - \omega\omega_s - \omega_s\dot{\varphi}) = \omega_s w \cos\varphi \quad (17)$$

et

$$\dot{a}\,(2\omega + 2\dot{\varphi} - \omega_s) = \omega_s w \sin\varphi\,. \quad (18)$$

La variation adiabatique a lieu lorsque la fréquence d'excitation ω est voisine de la fréquence propre ω_s. Pour un cyclotron, on a toujours la relation $|\omega - \omega_s| \ll \omega_s$ ce qui simplifie les trois dernières équations comme suit:

$$b \overset{\rightarrow}{=} \frac{w}{2\omega_s} \quad (19)$$

$$\dot{\varphi} \overset{\rightarrow}{=} \frac{w\cos\varphi}{a} + \omega_s - \omega \quad (20)$$

$$\dot{a} \overset{\rightarrow}{=} w \sin\varphi\,. \quad (21)$$

La constante b est négligeable vis-à-vis de a. En effet, l'intégration de (21) donne $a = wt$ pour $\sin\varphi = 1$ ce qui fait au bout d'une période $a = 2\pi w/\omega_s$. Donc b ne représente qu'une petite fraction de l'augmentation d'amplitude en une période.

D'autre part, la constante c de l'expression (14) est arbitraire, elle sera choisie égale à zéro Ainsi il ne reste que

$$r = a(t) \exp i\,[\omega t + \varphi(t)] \quad (22)$$

$a(t)$ est de ce fait l'amplitude du pendule de rotation, c'est-à-dire le rayon de l'orbite d'un ion dans le cas précédent: $a(t) = r$. Nous constatons maintenant que le couple d'équations (21) et (20) est identique au couple (7) et (8a). Le pendule linéaire obéit aux mêmes équations parce que son mouvement est la projection d'un mouvement rotatoire. Nos déductions sont de portée plus générale, elles s'appliquent à n'importe quel système oscillant, harmonique ou non. La preuve en a été donnée par A. Schock *et coll.*[1]) et [2]).

3.1. REMARQUES

(a) Dans le cas stationnaire $\varphi = \text{const.}$ l'équation (20) devient $\omega = \omega_s + (w\cos\varphi)/r$. La fréquence du mouvement est différente de la fréquence propre si $\cos\varphi \neq 0$. Ce changement de fréquence est bien connu dans l'horlogerie: on sait que l'impulsion mécanique reçue par le balancier doit avoir lieu lors de son passage à zéro afin que la marche de la montre soit indépendante de la force du ressort. Dans ce cas, l'impulsion est déphasée de 90° ($\varphi = 90°$) par rapport à l'amplitude du balancier, $\cos\varphi$ est nul et de ce fait $\omega = \omega_s$.

(b) Lorsque r est très petit, le terme $(w\cos\varphi)/r$ dans l'équation (20) excède de beaucoup le terme $\omega_s - \omega$, d'autant plus que ω_s est très voisin de ω. Les équations se résument à

$$\dot{r} = w\sin\varphi$$
$$r\dot{\varphi} = w\cos\varphi\,.$$

[1]) R. Hagedorn, M. G. N. Hine and A. Schoch, Nonlinear orbit problems in synchrotrons. CERN Symposium 1956, Proceedings, vol. I, p. 237–53.

[2]) A. Schoch, Theory of linear and non-linear perturbations of betatron oscillations in alternating gradient synchrotrons. CERN 57–21.

Ceci est le mouvement d'un point se déplaçant à vitesse constante sur une droite verticale (parallèle à y) dans le diagramme de phase.

4. Solution partielle des équations du mouvement

Il s'agit en même temps de la solution du problème de la résonance anharmonique. Examinons l'équation (20) ou (8a). Dans le cas stationnaire $\dot{\varphi} = 0$ cette équation devient

$$\omega = \omega_s + \frac{w \cos \varphi}{r} \tag{23}$$

où ω_s est fonction de r. Pour le cyclotron, la fréquence propre vaut

$$\omega_s = \frac{eB}{m_0}\left[1 + \left(\frac{eBr}{m_0 c}\right)^2\right]^{-\frac{1}{2}} \tag{24}$$

où m_0 est la masse de l'ion au repos et c la vitesse de la lumière. Pour des rayons pas trop grands, on peut développer et garder le premier terme quadratique

$$\omega_s \overset{\rightarrow}{=} \omega_0\left[1 - \tfrac{1}{2} K\left(\frac{\omega_0}{c}\right)^2 r^2\right] \tag{25}$$

avec $\omega_0 = eB(r=0)/m_0$ la fréquence propre au centre et

$$K = 1 + n\left(\frac{c}{\omega_0 r}\right)^2 \cong 1 - \left(\frac{c}{\omega_0}\right)^2 \frac{B''}{B} \tag{26}$$

où B'' est la seconde dérivée de l'induction par rapport à r. B'' est négatif, K est plus grand que 1. L'indice du champ est $n = -rB'/B$.

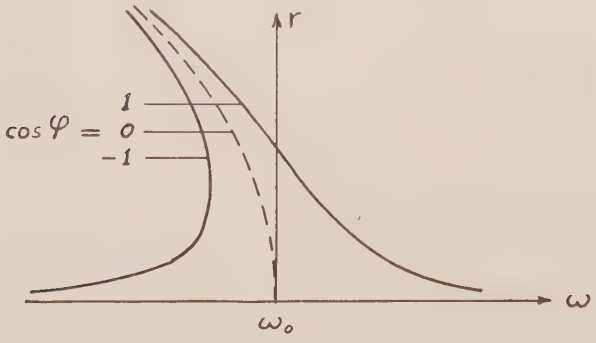

Fig. 3. Courbe de résonance.

Si nous reportons graphiquement la formule (23) avec ω en abscisse et r en ordonnée nous obtenons une série de courbes ayant $\cos\varphi$ comme paramètre. Les deux courbes extrêmes $\cos\varphi = \pm 1$ donnent la courbe de résonance anharmonique bien connue (voir fig. 3).

Pour résoudre les équations du mouvement il faut distinguer deux cas:

4.1. LA VITESSE D'EXPANSION w EST CONSTANTE

Pour de petites orbites, tant que r reste inférieur à l'espace interélectrode, la particule se meut dans une région où le champ de haute fréquence est constant, donc w l'est de même en

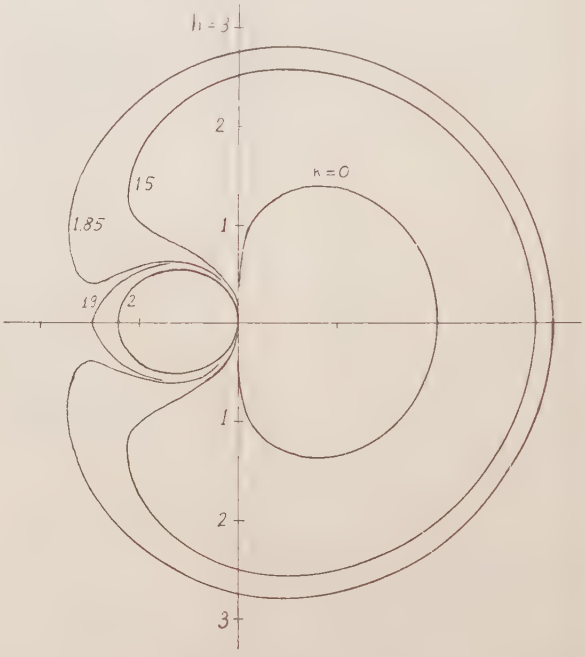

Fig. 4. Fréquence fixe.

vertu de (6). Ecrivons les équations (7) et (8a) sous forme normale:

$$\frac{dh}{d\vartheta} = \sin\varphi \tag{27}$$

$$\frac{d\varphi}{d\vartheta} = \frac{\cos\varphi}{h} - \tfrac{1}{2}h^2 + k \tag{28}$$

avec

$$h = r/r_n \quad \text{et} \quad \vartheta = t/t_n \tag{29}$$

r_n est un rayon unité qui vaut

$$r_n^3 = \frac{wc^2}{K\omega_0^3}$$

t_n est un temps unité qui vaut

$$t_n = r_n/w \tag{31}$$

et puis le désaccord s'exprime par k:

$$k = (\omega_0 - \omega)\, t_n\,. \tag{32}$$

La solution partielle de (27) et (28) est†

$$\cos\varphi = \tfrac{1}{8}h^3 - \tfrac{1}{2}kh + \mathscr{H}/h \ . \qquad (33)$$

C'est l'équation des courbes dans le diagramme de phase. Dans la fig. 4, nous avons dessiné

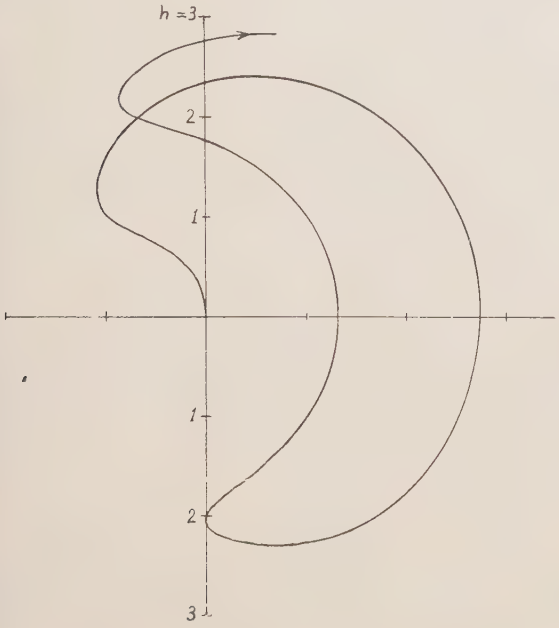

Fig. 5. Fréquence variable, $k = 1.1 + 0.33\,\vartheta$

quelques courbes pour différents paramètres k. La constante $\mathscr{H}$ de l'éq. (33) est choisie égale à zéro; c'est le cas où les ions partent de l'origine (cette figure est tirée de [3]) p. 29). De même, la

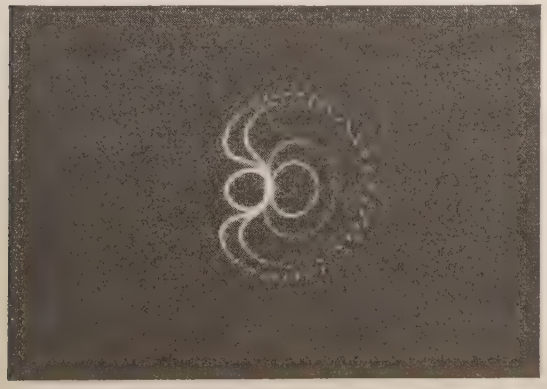

Fig. 6

† D'une façon plus générale, si les équations sont $\mathrm{d}z/\mathrm{d}t = a\sin\varphi$ et $\mathrm{d}\varphi/\mathrm{d}t = (\cos\varphi)/z + F(z)$, l'équation des courbes devient $az^{1/a}\cos\varphi + \int z^{1/a}F(z)\,\mathrm{d}z = \text{const.}$

fig. 6 représente ces courbes; elle a été obtenue au moyen de l'analogue électromécanique de Barbier (voir réf. [4]) et [5])).

Pour un synchro-cyclotron, k est variable, c'est-à-dire ω suit un programme de fréquence.

L'équation des courbes pour k variable est beaucoup plus difficile à trouver. Mais nous pouvons construire la courbe point par point, ce que nous avons fait dans la fig. 5 pour $k = 1.1 + 0.33\,\vartheta$ (variation linéaire de la fréquence d'excitation). La fig. 7 prise au moyen de l'analogue électromécanique de Barbier, représente le même cas.

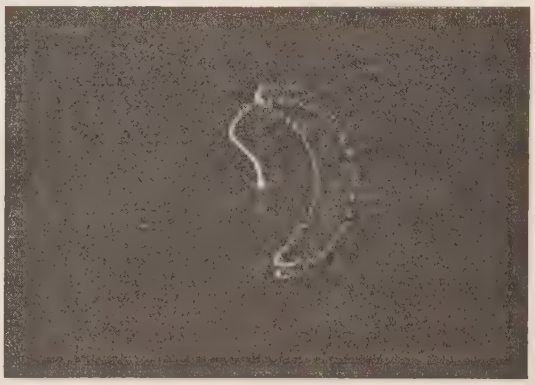

Fig. 7

4.2. LA VITESSE D'EXPANSION w EST PROPORTIONNELLE A $1/r$

Lorsque le rayon de l'orbite atteint une valeur supérieure à l'espace interélectrode, la particule se trouve à chaque demi-tour dans le champ électrique pendant un court instant, et le reste du temps elle ne subit pas d'accélération. C'est le gain maximum d'énergie par tour qui reste constant; il vaut $2V$ si V est la tension de crête entre électrodes. La vitesse d'expansion devient

$$w = \frac{V}{\pi B r} \qquad (34)$$

[3]) R. Keller, M. Fidecaro et M. Barbier, Calcul d'orbites dans un synchro-cyclotron. CERN 57-45.

[4]) M. Barbier, A mechanical analogue for the study of betatron oscillations. CERN Symposium 1956, Proceedings, vol. I, p. 262–264.

[5]) M. Barbier and A. Schoch, Study of two-dimensional non-linear oscillations by means of an electromechanical analogue model, applied to particle motion in circular accelerators. CERN 58-5.

au lieu de (6). Ecrivons de nouveau les équations (7) et (8a) sous forme normale:

$$\frac{\mathrm{d}h^2}{\mathrm{d}\vartheta} = 2 \sin \varphi \tag{35}$$

$$\frac{\mathrm{d}\varphi}{\mathrm{d}\vartheta} = \frac{\cos \varphi}{h^2} - h^2 + k \tag{36}$$

avec:

$$h = r/r_\mathrm{n} \; ; \qquad \vartheta = t/t_\mathrm{n} \; ;$$

$$r_\mathrm{n}^4 = \frac{2Vc^2e/m_0}{\pi K \omega_0^4} \tag{37}$$

$$t_\mathrm{n}^2 = \frac{2\pi c^2}{(e/m_0) V K \omega_0^2} \, .$$

L'équation des courbes sera

$$\cos \varphi = \tfrac{1}{5} h^4 - \tfrac{1}{3} k h^2 + \mathscr{H}/h \, . \tag{38}$$

De semblabes calculs ont été faits par M. Konrad[6]).

5. Energie maximum du cyclotron

L'expression (38) nous donne immédiatement le rayon maximum qu'un ion peut atteindre. Comme les ions partent du centre, $\mathscr{H}$ est nul et il reste

$$\cos \varphi = \tfrac{1}{5} h^4 - \tfrac{1}{3} k h^2 \, . \tag{39}$$

Regardons la fig. 8. Le point h_m est la position extrême qu'un ion peut atteindre. Ce point se trouve sur la séparatrice, pour laquelle le paramètre vaut k_m. En h_1 on a les conditions

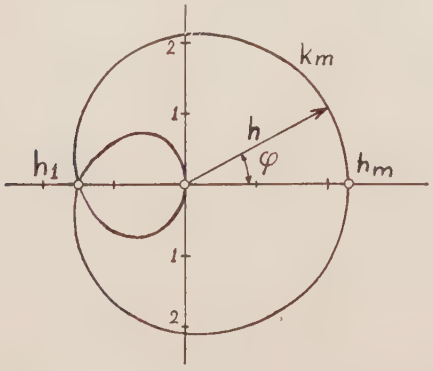

Fig. 8. Equation (39).

suivantes: $\cos \varphi = -1$ et $\mathrm{d} \cos \varphi / \mathrm{d}\vartheta = 0$ d'où les deux équations

$$\tfrac{1}{5} h^4 - \tfrac{1}{3} k h^2 + 1 = 0 \quad \text{et} \quad \tfrac{4}{5} h^3 - \tfrac{2}{3} k h = 0 \, . \tag{40}$$

Ceci nous donne

$$k_\mathrm{m} = \frac{6}{\sqrt{5}} \, . \tag{41}$$

Résolvons maintenant (39) au point h_m, donc pour $\cos \varphi = +1$ et $k = k_\mathrm{m}$:

$$h_\mathrm{m}^2 = (1 + \sqrt{2}) \sqrt{5} = 5.39 \, . \tag{42}$$

Le carré du rayon maximum est alors, d'après (37):

$$r_\mathrm{m}^2 = h_\mathrm{m}^2 r_\mathrm{n}^2 = 5.39 \sqrt{\frac{2Vc^2e/m_0}{\pi K \omega_0^4}} \, . \tag{43}$$

L'énergie d'une particule vaut, en électron-volts:

$$\varepsilon \cong \tfrac{1}{2} (e/m_0) B^2 r^2 \, . \tag{44}$$

Avec (43) nous trouvons enfin

$$\varepsilon \cong 2.15 \sqrt{\frac{m_0 c^2}{e} \frac{V}{K}} \, . \tag{45}$$

C'est, à un facteur numérique près, la moyenne géométrique entre l'énergie de repos et le gain d'énergie par tour. Notre résultat coincide avec celui de B. L. Cohen[7]).

6. Etalement de phase

En réalité, les ions ne partent pas exactement avec un rayon nul lorsqu'ils sortent de la source, même si leur vitesse est nulle. Dans un champ électrique et magnétique croisés, homogènes tous les deux, le centre des orbites se meut avec la vitesse $w = E/2B$ où $\frac{1}{2}E$ est le champ électrique homogène tournant dans le bon sens. w est donc aussi la vitesse orbitale de l'ion au repos. Le rayon au départ sera

$$r_0 = w/\omega_\mathrm{s} \, . \tag{46}$$

Le champ tournant dans le mauvais sens est cause d'une perturbation b donnée par la formule (19). Celle-ci est deux fois plus petite que r_0. Le calcul qui suit ne sera donc qu'une approximation.

Regardons les formules (33) et (38). Pour de très petits rayons ($h \to 0$) ces formules deviennent

$$\cos \varphi \overset{\rightarrow}{=} \mathscr{H}/h \, . \tag{47}$$

L'étalement de phase est alors

$$\Delta \cos \varphi = 2\mathscr{H}/h \, . \tag{48}$$

[6]) M. Konrad, Zagreb, Equations for the ion motion in a fixed frequency cyclotron, Glasnik Mat.-Fiz. I Astr., Tome 11, No. 3–4 (1956) p. 253.

[7]) B. L. Cohen, The theory of the fixed frequency cyclotron, Rev. sc. Instr. **24** (1953) 589.

Soit $h_0 = r_0/r_n$ la valeur de h au départ. L'étalement maximum est à ce moment

$$(A \cos \varphi)_0 = 2 = 2\mathscr{H}/h_0 . \qquad (49)$$

Ainsi $\mathscr{H}$ est déterminé, et l'étalement devient, avec (46) et (6):

$$A \cos \varphi = 2\frac{h_0}{h} = 2\frac{r_0}{r} \cong \frac{E}{B\omega_s r} . \qquad (50)$$

L'étalement de phase est inversement proportionnel au rayon de l'orbite, ceci dans le das (a) formule (33) comme dans le cas (b) formule (38). On peut démontrer qu'il en est de même dans le cas transitoire où le rayon de l'orbite est voisin de l'espace interélectrode. Il y a groupement de phase (phase grouping) lors de l'accélération.

Voici un exemple numérique.

Soit $V = 200\,000$ volts, $B = 1.4$ Wb/m^2, $e/m_0 = 0.48 \times 10^8$ (deutons) et $K = 5$.

Soit l'espace interélectrode $= 0.1$ m d'où $E \cong 2 \times 10^6$ volts/m.

Le rayon maximum devient, d'après (43)

$$r_m = 0.63 \text{ m} .$$

L'étalement de phase, d'après (50):

$$A \cos \varphi = 0.034$$

ce qui fait par exemple une phase de 0 à 15°. L'énergie maximum devient, d'après (45):

$$\varepsilon = 18.6 \text{ MeV} .$$

Si l'on admet que K est indépendant de r on aura d'après (26):

$$B''/B = -0.20 \qquad \text{d'où} \qquad B(r_m) = 0.96\, B(r = 0) .$$

Le champ magnétique décroit de 4% depuis le centre jusqu'à l'extraction du faisceau.

7. Accélération par un champ variant d'une façon aléatoire

Dans ce dernier paragraphe on esquisse la façon de calculer une accélération stochastique en faisant usage du diagramme de phase. Au moyen de cette accélération particulière il est possible d'accumuler un faisceau dans un synchro-cyclotron ainsi que d'augmenter considérablement l'intensité d'une telle machine. Ce problème a été étudié à fond sous référence[8]). L'idée première a été énoncée par E. L. Burshtein, V. I. Veksler et A. A. Kolomenskii[9]). Un autre travail traitant un sujet semblable va être publié sous peu[10]).

Il est facile de suivre le mouvement d'un point dans le diagramme de phase lorsque le champ accélérateur possède une amplitude et une fréquence $\omega(t)$ variant d'une façon quelconque. Au lieu de prendre les photographies de l'image stroboscopique à une cadence synchronisée avec $\omega(t)$, il est plus judicieux de se synchroniser avec ω_s. Ceci donne un diagramme de phase un peu modifié.

Soit un rayon vecteur dans ce nouveau diagramme de phase r, φ^*, avec

$$\varphi^* = \varphi - \int [\omega_s - \omega(t)]\, dt . \qquad (51)$$

Introduisons φ^* dans les équations (7) et (8a), cela fait

$$\frac{dr}{dt} = w \sin\left(\varphi^* + \int [\omega_s - \omega(t)]\, dt\right) \qquad (52)$$

$$r\frac{d\varphi^*}{dt} = w \cos\left(\varphi^* + \int [\omega_s - \omega(t)]\, dt\right) . \qquad (53)$$

Admettons d'abord que $\omega(t)$ est égal à ω_s. Le point se déplacera alors à une vitesse w dans la direction $\varphi^* + \text{const}$.

Faisons maintenant varier la phase du champ accélérateur d'une façon particulière, comme suit: Le générateur de haute fréquence émet des trains d'ondes de fréquence constante ω_s et de durée égale à Q périodes (voir fig. 9).

Après chaque train d'ondes il y a un saut de phase pris au hasard (ceci est réalisable au

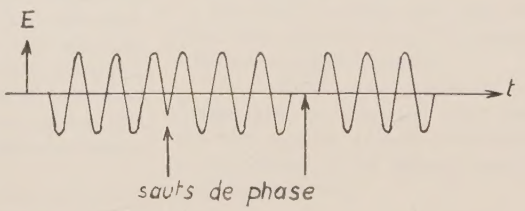

Fig. 9.

[8]) R. Keller and K. H. Schmitter, Beam storage with stochastic acceleration and improvement of a synchro-cyclotron beam. CERN 58-13.

[9]) E. L. Burshtein, V. I. Veksler et A. A. Kolomenskii, A stochastic method of accelerating particles, A.E.R.E. Lib/Trans. 623 (Harwell, 1955).

[10]) R. Gabillard et A. Chaber, Etude analogique de la stabilité de phase des particules accéléreés dont la tension accélératrice possède une modulation parasite de caractère aléatoire. Rapp. CERN (à paraître).

moyen d'un photomultiplicateur branché sur un circuit oscillant amorti. Chaque coup amorce un train d'onde amorti, composé de Q périodes en moyenne. La tension est amplifiée et filtrée avec des filtres passe-bande). Le point décrit sur le diagramme une succession de lignes droites de longueur $wQ2\pi/\omega$, avec changement de direction à chaque saut de phase. Le mouvement ressemble à un mouvement brownien dont le libre parcours moyen vaut

$$\lambda = wQ\ 2\ \pi/\omega\ . \tag{54}$$

Il s'agit donc d'une réelle diffusion à deux dimensions, avec une constante de diffusion égale à

$$D = \tfrac{1}{2}\ \lambda w = \pi Q w^2/\omega\ . \tag{55}$$

L'analyse Fourier de notre champ accélérateur donne un spectre de largeur ω/Q, dont les composantes n'ont pas de relation de phase, comme le spectre d'une tension de bruissement. On peut facilement se rendre compte que la fréquence propre ω_s peut changer, mais il faut qu'elle reste à l'intérieur de la bande.

Le mouvement des ions obéira dans l'ensemble à l'équation de diffusion

$$\text{div.}\ \tfrac{1}{2}\ \lambda\ \text{grad}\ (w\rho) - \rho/T = \partial\rho/\partial t \tag{56}$$

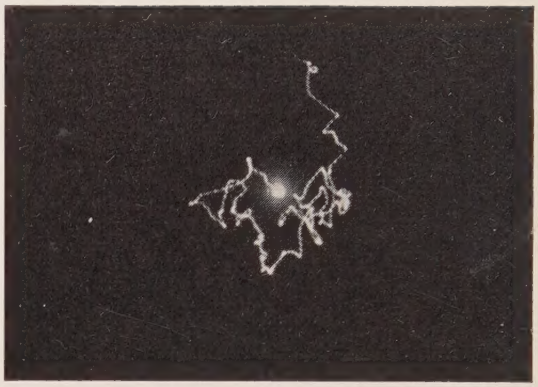

Fig. 10

où ρ est la charge d'espace et T la vie moyenne des ions. Ce mouvement s'appelle accéleration stochastique. Voici encore (fig. 10) une photo stroboscopique pour le cas d'une accélération de cette sorte, faite au moyen de l'analogue électromécanique.

Je tiens à remercier particulièrement Monsieur le Professeur W. Gentner pour l'impulsion qu'il a donnée à ce travail, ainsi que F. Louis pour l'aide mathématique qu'il a apportée. Les grandes possibilités du CERN, grâce au Professeur C. J. Bakker, Directeur général, m'ont été très chères.

Spotlight on Industry

This section appears each month and features various happenings of interest in the nuclear industrial world and objective information on products of the nuclear manufacturers. It is offered entirely as a service and all nuclear manufacturers are cordially invited to submit clearly objective and descriptive material on their endeavours and product developments for consideration for use in this section.

TRANSISTORIZED 128-CHANNEL SCALER-ANALYZER

Radiation Counter Laboratories, Inc., 5121 W. Grove, Skokie, Illinois, U.S.A.

The RCLiac-128 is a completely integrated system. It performs nuclear data processing operations from gross counting through scintillation spectroscopy.

Compact (21″ high × 19″ wide × 24″ deep) instrument weighs 115 pounds and requires 185 watts power.

Among the many features of the RCLiac-128 are: plug-in module construction; "Instant" Number or Curve CRT display; magnetic core memory capacity of 1 000 000 counts per channel; pre-set time, 0.19 seconds to 28 hours; pre-set count 2^1 to 2^{24}; 600 to 1 500 volts negative high voltage, stable to 50 parts per million with well regulated line; overall amplifier gain of 1 000; and integral linearity of ADC less than $\pm$ 1% for channels 5 through 128.

Instrument adds and subtracts through logical decimal arithmetic circuits.

HIGH-SENSITIVITY FAST NEUTRON SURVEY METER

Nucleonic Corporation of America, 196 Degraw Street, Brooklyn 31, New York

A high-sensitivity fast neutron survey meter, model FN2B for the detection and measurement of fast neutrons in the presence of intense gamma radiation fields is announced.

The detector consists of a uniform

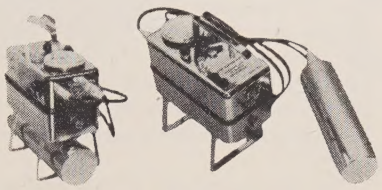

dispersion of ZnS grains molded directly into lucite. The lucite serves the dual purpose of supplying the proton recoils which produces the light scintillation in the phosphor and of transmitting this light to the photomultiplier tube. Operation is unaffected by gamma rays from Co^{60} up to 4R/h. It has no sensitivity to slow neutrons.

Neutron flux measured in neutrons/cm²·sec is read on a panel meter. A switch with 3 ranges of sensitivity; 0–5, 0–50, and 0–500 neutrons/cm²·sec permits easy range adjustment. The three ranges are linear and require no calibrating chart. On the most sensitive range, 5 neutrons/cm²·sec gives full scale deflection. Since tolerance dose for fast neutrons is 20 neutrons/cm²·sec the instrument gives full scale deflection for $\frac{1}{4}$ tolerance dosage.

AUTOMATIC NUCLEAR COUNTING SYSTEM

Società Elettronica Lombarda, Via Teodosio 70, Milan (Italy)

The system is composed of a fast 1000 scaler, an automatic sample changer of very simple and sturdy design and a time printing machine.

The scaler of full modular design comprises a HV supply unit (300–2020 V, stability $\pm$ 0.05%, resettability $\pm$ 0.1%); a non overloading input amplifier unit (G = 100, rise time better than 0.2 μsec); a fast discriminator, or a single channel analyser unit, (5–100 V threshold, 1–2–4–8 V channel width); three electronic decades with 1 μsec resolving time, and last the automatic counting unit (auto-time from 10 to 9999 sec in 1 sec steps; autocount from 1000 to 10^{-6} — 1 in 100 counts steps).

The automatic sample changer of patented design, is mechanically very simple and sturdy; it takes 30 samples on 1″ planchets or 12 samples on 2″ planchets.

It is possible to use three different detectors simply by replacing the detector head, namely an end window G.M. tube; an ultra thin window (0.9 mg/cm²) flow G.M. or proportional tube; a scintillation counter with alfa, beta, or gamma phosphors.

The G.M. counting gas used with G.M. flow tubes is a very inexpensive mixture of argon-buthane.

The modular construction not only makes the maintenance very easy, but also permits successive extentions or variations of the system avoiding any obsolescence.

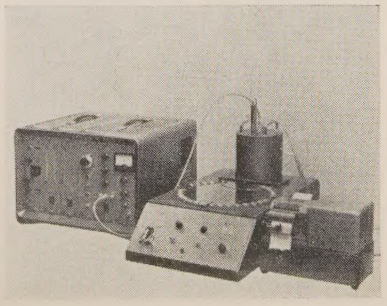

LOW COST NEUTRON SOURCE

High Voltage Engineering Corporation, Burlington, Mass.

A new 400 000 volt Van de Graaff positive-ion accelerator (PN-400) is announced.

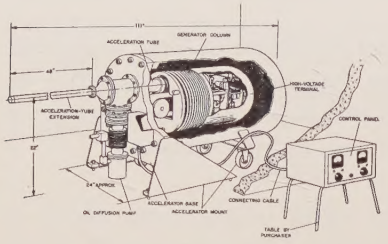

Performance ratings: *Voltage*: 0.40 million volts. *Continuous beam current*: controllable from 10 to 150 microamperes, nominal. *Monatomic ion yield*: at least 50% of beam current. *Pulsed current amplitude*: fixed at 100 μA nominal. *Beam diameter for 90% of current*: 1 cm maximum. *Pulse lengths*: available from 10 to 200 microseconds. *Pulse rise and decay times*: 3 microseconds, maximum. *Repetition rates*: available from 1 to 500 pps.

A.C. PLUG IN ELECTRONIC VOLTMETER

Metronix, Inc., Chesterland, Ohio

An AC electronic voltmeter module, designed for plug-in use with a remote meter, is announced.

Believed to be the first such AC plug-in circuitry, Model SPD-22 will measure from 10 millivolts to 300 volts r.m.s. full scale sensitivity, depending on the input voltage determined by the built-in attenuator. Offering the same freedom of meter location as the earlier DC Model SPD-21, Model SPD-22 contains all VTVM circuitry except the power supply. It measures only 5 by 2½ by 4¼ inches.

With this unit, meters being utilized for other readings may also be used for electronic AC voltage measurement. Such meters should have a minimum sensitivity of 250 microamperes and a maximum of 50 microamperes.

With an input impedance on 1 megohm, 10 micro-micro-farads, Model SPD-22 imposes almost no load on the circuit being measured. Its accuracy is plus or minus 3 per cent with a meter of 2 per cent accuracy. Frequency range is 20 cps to 50 kc/s at 2 per cent accuracy and 50 kc/s to 100 kc/s at 3 per cent accuracy.

The external power supply used with Model SPD-22 must provide 6.3 volts at 600 milliamperes AC or DC for the tube filaments and 120 to 170 volts DC at 5 milliamperes for the plates.

The two tubes used in this module may be replaced by both MIL and five-star equivalents if desired.

STANDARD NEUTRON DETECTION FOILS

Aerojet-General Nucleonics, P.O. Box 77, San Ramon, California

Accurate, reproducible spectral determinations are now possible by using a newly developed system of neutron detection foils. This system makes it possible to compare the results of various radiation-effects studies. Because such studies are only as complete as the neutron spectra data upon which they are based, these Standard Neutron Detection Foils provide an invaluable means of accurately correlating either single reactor system studies or similar studies using various reactors. Accurate cross-calibration and standardization of fast neutron data are obtained by measuring the spectrum in six energy increments:

1. Thermal fluxes are measured with gold or cobalt foils.

2. Neutron energies greater than 1 keV are measured by plutonium-239 foils.

3. Neutron energies greater than 1.5 MeV, by uranium-238 foils.

4. Neutron energies greater than 2.9 MeV, by sulfur-32 foils.

5. Neutron energies above 5.3 MeV are measured by analyzing the products of the (n,p) reaction on aluminium-27 foils.

6. Energies greater than 8.6 MeV by analyzing the products from the (n,α) reaction on aluminium-27 foils.

A boron-10 shield is used to protect the fission foils from thermal neutrons during irradiation. Cadmium covers are available for use with the gold and cobalt foils for determining the cadmium ratio. Sulfur foils are repackaged in "cold" aluminium after their irradiation, thus eliminating the possibility of mistaking certain reactions in aluminium for those in sulfur.

Foil Specifications

Gold Foils: *For Thermal Flux Measurements*

Dimensions of gold foils 0.500 inch in diameter by 0.002 inch thick.

Each foil weighs approximately 0.12 g. Pt and Ag impurities are less than 0.01% by weight.

The gold foils are packaged between 0.030 inch thick aluminium discs (99.999% pure), and are pressure-welded about the periphery.

Packaged foil is 0.750 inch diameter by 0.062 inch thick.

Cobalt Foils: *For Use in High Thermal Fluxes for Long Irradiation Times*

Dimensions of cobalt metal foils 0.500 inch in diameter by 0.004 inch thick.

Each foil weighs 0.11 g.

The physical nature of these foils makes packaging unnecessary.

Uranium Foils: *For Measurement of Neutrons with Energies Greater than 1.5 MeV*

Dimensions of uranium 0.250 inch in diameter by 0.020 inch thick.

U-238 (with 0.4039% U-235 by weight) encased in a pressure-welded aluminium package 0.500 inch in diameter by 0.060 inch thick.

Sulfur Foils: *For Measurement of Neutrons with Energies Greater than 2.9 MeV*

Dimensions of sulfur 0.750 inch in diameter by 0.250 inch thick tablets encased in an aluminium cup equipped with a ring cover.

92% sulfur (99.999% pure) mixed with graphite (8%) for elimination of static charge build-up.

Aluminium Foils: *For Measurement of Neutrons with Energies Greater than 5.3 and 8.6 MeV*

Dimensions of aluminium 0.750 inch by 0.030 inch thick.

Each foil contains 0.585 g of 99.999% pure aluminium.

The physical nature of these foils makes packaging unnecessary.